6-23-2022

New Connection Details for Concrete Filled Tubes to Precast Concrete Elements for Accelerated Bridge Construction Applications

FNU SHEHARYAR E REHMAT
Florida International University, ssheh005@fiu.edu

FLORIDA INTERNATIONAL UNIVERSITY

Miami, Florida

NEW CONNECTION DETAILS FOR CONCRETE FILLED TUBES TO PRECAST CONCRETE ELEMENTS FOR ACCELERATED BRIDGE CONSTRUCTION APPLICATIONS

A dissertation submitted in partial fulfillment of the

requirements for the degree of

DOCTOR OF PHILOSOPHY

in

CIVIL ENGINEERING

by

FNU Sheharyar e Rehmat

2022

To: Dean John L. Volakis
College of Engineering and Computing

This dissertation, written by FNU Sheharyar e Rehmat, and entitled New Connection Details for Concrete Filled Tubes to Precast Concrete Elements for Accelerated Bridge Construction Applications, having been approved in respect to style and intellectual content, is referred to you for judgment.

We have read this dissertation and recommend that it be approved.

Arindam Gan Chowdhury

Armin Mehrabi

Kingsley Lau

Wallied Orabi

Atorod Azizinamini, Major Professor

Date of Defense: June 23, 2022

The dissertation of FNU Sheharyar e Rehmat is approved.

Dean John L. Volakis
College of Engineering and Computing

Andrés G. Gil
Vice President for Research and Economic Development
and Dean of the University Graduate School

Florida International University, 2022

DEDICATION

I dedicate this dissertation to my father and mother for their love and support, to my brother and sisters for admiring my achievements.

ABSTRACT OF THE DISSERTATION

NEW CONNECTION DETAILS FOR CONCRETE FILLED TUBES TO PRECAST CONCRETE ELEMENTS FOR ACCELERATED BRIDGE CONSTRUCTION APPLICATIONS

by

FNU Sheharyar e Rehmat

Florida International University, 2022

Miami, Florida

Professor Atorod Azizinamini, Major Professor

The synergistic interaction of steel and concrete in concrete filled tube (CFT) composite members improves structural performance by delaying local buckling of steel tube. Compared to localized confinement provided by discreet ties in reinforced columns, the steel tube provides continuous confinement to infill concrete which results in improved energy dissipation and ductility performance. Concrete filled tubes (CFTs) provide improved structural strength and ductility while minimizing the cost of column formwork. The construction sequence of CFT allows its use for accelerated bridge construction applications.

The use of CFTs for bridges in the U.S. has been limited mainly due to lack of design provisions, particularly for seismic zones. This research proposes a new detail for column-to-footing connection using ultra-high performance concrete (UHPC). Several details were studied, and a detail comprises of CFT embedded in a layer of UHPC located near the plastic hinge zone of the column is selected to for experimental and numerical study. Using experiments from existing literature, pretest finite element analysis was carried out on the design parameters including effect of confinement, tension pull out and shear behavior of the connectors.

Three connection details were experimentally studied under a combination of constant axial and incremental lateral cyclic load. The proposed connection is desired to have a ductile behavior with the plastic hinge forming away from the footing which is typically designed as a capacity protected element. The results of the experiments and pretest analysis were used to carry out parametric finite element analysis. Further experimental and numerical study is proposed to recommend design and construction provisions.

TABLE OF CONTENTS

CHAPTER PAGE

LIST OF TABLES

LIST OF FIGURES

ABBREVIATIONS AND ACRONYMS

ABC	Accelerated Bridge Construction
ACI	American Concrete Institute
AASHTO	American Association of State Highway and Transportation Officials
ABC	Accelerated Bridge Construction
AREMA	American railway engineering and maintenace-of-way assoication
ASTM	American Society of Testing and Materials
CFT	Concrete Filled Tubes
CIP	Cast-in-place
CHSTP	California High-Speed Train Project
DOT	Department of Transportation
EXP	Experimental
FEA	Finite Element Analysis
FIU	Florida International University
FRA	Federal Railway Administration
HRWR	High Range Water Reducing Admixture
HSR	High-Speed Rail
NSC	Normal Strength Concrete
PBES	Prefabricated Bridge Elements and Systems
RC	Reinforced Concrete
SPMT	Self propelled modular transporters
UHPC	Ultra-High Performance Concrete

CHAPTER 1

INTRODUCTION

1.1 Background

The United States (U.S.) highway infrastructure consists of approximately 614,000 bridges. These existing bridges are periodically inspected, and their condition is characterized as good, fair, or poor. It is estimated that 7.9% bridges have been assigned a condition rating of poor in 2016. Also, it is estimated that 9% (56,000) of total bridge inventory is structurally deficient [1]. Federal Highway Administration (FHWA) also identifies bridges which are structurally deficient but as of 2016, no longer characterizes the bridge as functionally obsolete.

Bridges are an integral part of highway infrastructure and construction of these structures is time consuming and costly. Besides an increase in demand for repair of existing bridges, there has been substantial increase in construction of new bridges as part of expanding road networks, mitigation for traffic congestion and replacement of deficient bridges. Out of the 17.5$ billion dollars spent on bridges in 2012, 16.4$ billion were allocated to rehabilitate and replace existing bridges while the remainder were devoted to new bridges. It is estimated that nation's backlog of bridge rehabilitation needs 123$ billion dollars [2]. Although, repair may be feasible for some of the deteriorating infrastructure, but in most cases new construction may be more economical. However, one of the challenges of new construction in urban areas is the impact on existing traffic which may incur significant indirect costs.

Besides the backlog for construction of new bridges, there have been recent developments for construction of new rail corridors in the United States. This is mainly due to increase in demand for mass transit in urban areas. Conventional modes of transportation, such as road and air travel, have caused congestion and

traffic problems in many cities around the world. To achieve high mobility for mass transit, there have been innovations in rail transportation. One such example is the introduction of high-speed railway (HSR) which offers a robust alternative to conventional trains, vehicular and air traffic systems for mid-range distances. HSR services now operate in more than 16 countries and carry millions of passengers trip per year. It is estimated that a total of 22,990 miles of HSR lines are in operation [3]. HSR offers an efficient, fast and a safe transportation system. Countries with a wide network of high-speed trains have shown a reduction in volume of road and air traffic. A brief overview of the HSR systems in different parts of the world is provided in the following section.

1.1.1 Brief Overview of High Speed Rail Networks

The introduction of HSR in Europe and Asia in mid-sixties has been a cornerstone in the economic development of many countries. HSR now operates up to 16 countries and many new countries like Turkey, Saudia Arabia, etc., are developing HSR systems. Figure 1.1 shows the percentage of HSR in the world by mileage [4].

Japan was the first country to develop the HSR, commonly known as Shinkansen, which was operated between Tokyo and Osaka in the 1960s. Benefiting from a dedicated infrastructure and at-grade level crossing, there have been no reported crashes since the inception of the Shinkansen network. China started as late as 2007-2008 and since then it has developed the largest network of HSR in the world. As of 2016, China has 13,670 miles of HSR [5]. The Chinese high-speed train operates at a speed of 220-235 miles/hr. China has also developed Maglev technology which operates on a short route with a maximum speed of 268 miles/hr [6]. Europe has an estimated HSR line of almost 4,124 miles which are mainly located in France,

Germany, Spain, and Italy. Additional high-speed lines are either being constructed or planned [7]. The total network of HSR in France is about 1,120 miles. Spain launched the high-speed train also known as AVE (Alta Velocidad Espanola) in 1992 between the Madrid-Sevilla corridor and now has the largest HSR system in Europe only next to China. Germany developed Inter City Express in 1991 which is the long-distance rail transport system. Until 2018, Germany has an HSR network of almost 1,030 miles. Other European countries like Turkey, Poland, Switzerland and Belgium have also developed HSR networks.

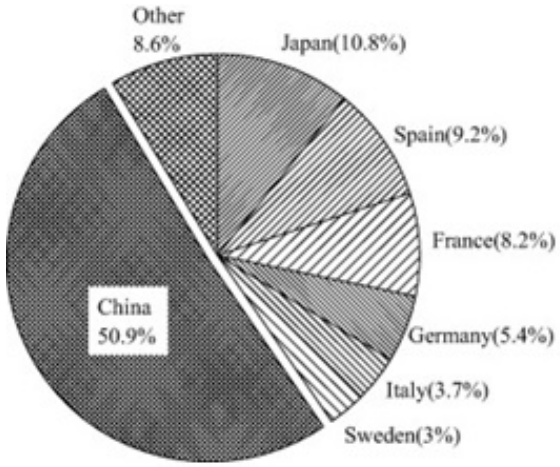

Figure 1.1: HSR mileage by countries[4].

The U.S. started its efforts in HSR in the 1960s which resulted in the introduction of Metroliner between the cities of New York and Washington D.C. The Federal Railway Administration has identified different corridors for connecting populated centers with HSR which are in the range of 100-600 miles. Figure 1.2 shows different planned corridors in the United States. Recently high-speed train projects are underway or in advanced stages of planning in California and Texas. Due to the geography and terrain of California, most of the structures on the rail network will use elevated tracks. The substructure height for railway structures may go up to a few hundred feet which poses considerable challenges from design and construction

standpoint. The construction of substructure for these bridges, using traditional construction methodologies, may not be efficient as these require the use of climbing formwork which is time-consuming and costly. Alternate solutions consist of the use of prefabricated columns, but the delivery and erection of these long columns is a challenging task. Owing to these constraints, the construction on some of the stretches on California high speed rail have been delayed, which has resulted in a substantial increase in cost of the project.

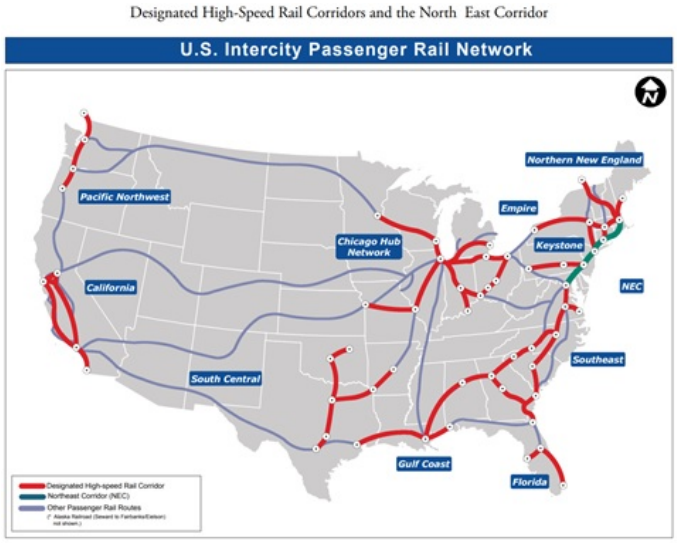

Figure 1.2: Planned HSR corridors in the U.S. [USDOT].

1.1.2 Design Considerations for High Speed Rail Structures

The design philosophy for HSR varies from conventional bridge structures as the former is expected to have continuity in operation at a relatively high-speed. Therefore, HSRs require higher performance metrics which are typically reflected in design and construction provisions. Besides operation controls, some of the HSR (such as California, USA) are located in high-seismic regions which can further increase the target seismic performance level for these structures.

Based on the speed, location and traveler's comfort, the rail structures have limitations on geometric controls such as alignment, slopes, and curvatures. The track's smoothness requires deflection checks which are different from conventional train bridges [4]. Also, the rail bridges are subjected to dynamic effects of high-speed trains, fatigue and rail-deck interaction which demand higher stiffness and dynamic stability. Other structural considerations for HSR bridges include seismic performance, creep, and thermal effects.

1.1.3 Typical Structures for High Speed Rail

In China, the HSR lines mainly consist of standardized simply supported beams for shorter spans and continuous beams for longer spans [4]. For medium spans, concrete filled tubes (CFT) arches, tied steel arch, and rigid frame prestressed structures have been used. A major portion of the Beijing-Shanghai HSR consists of simply supported prestressed box girders with a span of 105-ft. Due to diverse terrain, long span bridges on railway network have also been constructed. Most of the bridges on the German HSR network consist of simply supported and continuous box girder bridges. For substructure, the most common kind of pier columns consists of reinforced concrete (RC) single columns, wall piers and multi-column piers. Several different design codes have been developed for HSR. China has developed code for design of HSR and International Union of Railways code provides several design leaflets for HSR.

American railway engineering and maintenance-of-way association (AREMA) do not have any specific requirements for HSRs [8]. The existing federal and state regulations for passenger and freight trains in the U.S. do not address the design and operation for trains over 150 mph. Therefore, international regulations are

used for additional guidance. California high-speed train project (CHSTP) has published several guidelines for high-speed trains and are intended for design of high-speed train system elements. As mentioned earlier, the HSR system is planned for California which is located in an active seismic region. The development of HSR network in California needs to meet both seismic design and high-speed train serviceability requirements [9].

The cost of construction of an HSR network is an economic burden. The initial cost of HSR is usually higher due to stringent design and construction provisions. To reduce the cost, CHSTP recommends the use of standard superstructure cross-sections, prefabricated segments, and rolling forms. The use of these methods for superstructure would eliminate the need for erecting falsework, onsite curing time, and reduces temporary clearance requirements. Besides, HSR can benefit from accelerated bridge construction (ABC) techniques which can facilitate construction and provide structural elements which have a longer service life.

1.2 Accelerated Bridge Construction (ABC)

Considering the challenges associated with difficult terrain in a seismic zone, the use of traditional construction methodologies may not be feasible. Significant changes have been made over the last few decades on many frontiers including improved project management tools, material technology, and introduction of automation in construction. These methods have enabled improved scheduling, increased durability and construction of aesthetic structures but have failed to address the need for expedited replacement and new construction of bridge structures. The high cost is generally attributed to many factors including dedicated infrastructure and high maintenance, etc.

More recently, the introduction of ABC methods has brought paradigm shift for bridge industry by providing robust construction, improved durability and, in many cases, emulative performance to cast-in-place bridge elements. Although, these advancements have inherent benefits for the industry, but the widespread use of these methodologies have remained largely unimplemented. One of the challenges is the lack of experimental data on performance of these technologies and their comparison with traditional cast-in-place methods. The next section briefly presents some of the ABC methods and challenges associated with these methods.

1.2.1 Introduction to ABC Techniques

ABC techniques provide alternative to traditional construction of bridge structures. Although, project management and planning tools have been used for a long time to reduce time and cost for bridges; however, the term ABC has been coined more recently to include the range of innovations which allow faster and more cost-effective construction of bridges. These innovations include but are not limited to advanced materials, construction methods and smart project management tools. According to FHWA, ABC reduces traffic impacts, on-site construction time and weather related time delays [10]. Figure 1.3 shows the most commonly used ABC technologies.

Among the items listed in Figure 1.3, prefabricated bridge elements and systems (PBES) is the most used ABC method. In this system prefabricated elements, which are constructed off-site, are shipped, and assembled at the site. The construction of these elements in a controlled environment allows better quality control which results in an improved durability performance. Besides PBES, structure placement methods such as self-propelled modular transporters (SPMT), longitudinal launching and sliding are also gaining popularity due to their advantages [10].

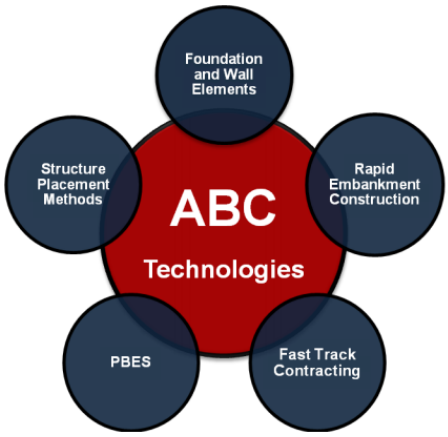

Figure 1.3: Commonly used Accelerated bridge construction technologies [10].

1.2.2 ABC Connections and Field Challenges

PBES have been used in construction industry owing to the benefits of robust construction and fewer on-site activities. PBES allows faster construction schedules and eliminates forming, scaffolding and other critical site activities. Some examples of PBES include precast panels, prefabricated bridge decks, orthotropic decks, etc. PBES is commonly used for construction of superstructure, substructures, and other ancillary structures. Prefabricated elements are generally constructed off site or inside precast plants and one of the considerations in design of these elements is the hauling and lifting capabilities. Due to limitations of transportation, most of PBES elements consist of a structural member which requires connection with other structural elements. Post-erection of these elements at the site, the connections between different elements are casted. In most cases, the joints are provided along the transverse and longitudinal direction such as closure joints between two precast deck panels or pier cap beam to column as shown in Figure 1.4.

The presence of joints and connections between structural elements has been a concern for bridge owners and state departments of transportation (DOT). This concern stems not only from durability issues but also structural performance of

(a) Erection of precast pier cap [11]

(b) Connection for precast deck panels [10]

Figure 1.4: Connections between prefabricated bridge elements and systems.

modular connected elements. From durability stand, problems such as cracking and leaking can facilitate other deterioration mechanisms and reduce service life of structure [12]. From structural point-of-view, connections present significant design challenges especially for high-seismic regions. Therefore, it is imperative that the connection between prefabricated elements should satisfy structural criteria as specified in different design codes. Since the connection is generally the weakest link in a structural element and should be designed to carry and transfer all anticipated forces safely. The selection of the connection detail should also take into account durability performance and service life considerations.

Besides the PBES and placement methods, some of structural members are intrinsically suited for ABC. One such example consists of concrete filled steel tubes (CFT) which have inherent benefits of robust construction especially for bridge piers and piles. The following section explains the structural and construction efficiency of CFT and current constraints to their use for ABC applications.

1.3 Concrete-Filled Steel Tubes

CFTs consist of an encasing tube of steel which is filled with conventional concrete. The tube is located at the periphery and provides protection to the in-fill concrete.

The tube also acts as a formwork element which reduces the cost of the structure. For most applications, CFTs do not require the use of any mild reinforcement inside the tube which reduces the labor cost of fabrication and assembly at the site. Besides protection, the steel tube offers confinement to the concrete which improves the structural capacity and ductility of the section.

Figure 1.5 shows typical cross-sections used for CFTs. The geometry of CFTs can be broadly classified into circular, square and rectangular cross-sections; however, other shapes such polygons and elliptical shapes are also gaining popularity. Other variation of the CFT include double skin tubes, concrete encased, and steel reinforced tubes.

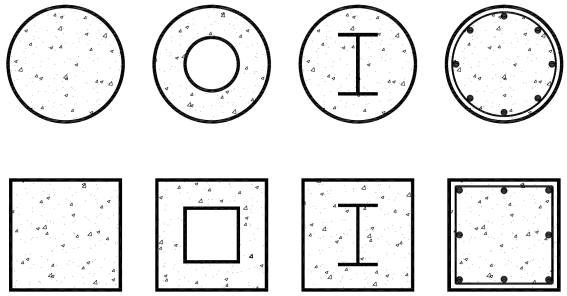

Figure 1.5: Typical cross-sections of concrete filled steel tubes.

Due to the large structural demands, CFTs have been commonly used in super-columns of high-rise buildings. Besides building construction, the inherent construction benefits of CFT and their structural performance can be beneficial for bridge piers especially in high seismic regions. Although, precast concrete bridge piers have been widely used for accelerated construction, but most of these bridges are located in flat terrain. For tough terrains, such as California, where the height of substructures may go up to few hundred feet, the delivery and erection of precast bridge piers is a challenging task. CFT provide a robust alternative since only a thin tube is delivered at site and erected using lighter cranes. Once secured to the substructure element, the tube is filled with concrete. Few examples of CFT ap-

plications are shown in Figure 1.6. The range of applications include bridge piers, trusses, and piles, etc. A brief overview of connection details for CFT are provided in following section.

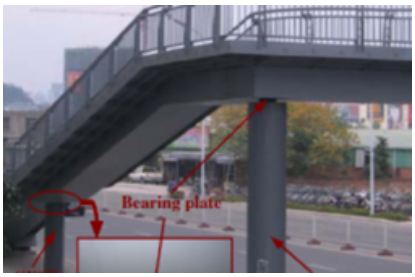

(a) CFT column for bridge pier [13]

(b) CFT for substructure [14]

(c) CFT for mega columns [15]

(d) Wangcang east river Bridge [16]

Figure 1.6: Examples of CFT for bridge and building applications.

1.4 Connections for Concrete Filled Tubes

A suitable connection detail is an important parameter for the economy of a connection in composite structures. The connections between CFT to concrete and steel beams for cast-in-place construction have been developed extensively [17]. These applications are typically for building construction where columns are framed at each floor and connected to reinforced concrete beams. Besides welded and bolted details, beam to column connections also consist of external, internal and through diaphragms. Welded connections are prone to wall distortions and weld fractures and may not be feasible for moment frames [18]. Diaphragm connections show

favorable inelastic response, but early deterioration is observed under imposed deformations. The through beam connections has an ideal rigid behavior and exhibited more ductility when compared to other connections [19].

The connections developed for high-rise and industrial buildings may be incompatible for ABC applications. For footing to cap beam connections, typical details consist of embedded, base plate and encased connections. However, the base plate connection is prone to localized failure for seismic applications and these details may not provide sufficient resistance which limit their use in bridge construction. Encased and embedded connections are a function of the depth of confining material (generally reinforced concrete and grout) and are prone to shear failure in the connection region. A number of connection details for bridge construction were proposed by [20] [21][22]. Most of these connections consisted of embedded connections with annular ring.

Recently, the use of ultra-high performance concrete (UHPC) for connection regions has provided an alternative solution to conventional materials [23] [24]. UHPC has also been used in connection of precast barrier [25], shell cap beam [26] and modular 3D construction [27]. The superior material and mechanical characteristics make it a feasible option for connection regions. The inherent deficiencies of traditional construction materials can be mitigated with the use of UHPC. Due to lower development length requirements and increased stiffness, compressive and tension strength, the material is ideally suited for structural performance. However, the use of UHPC has not been for connection regions of CFT has not been developed for ABC applications. In this study, a comprehensive experimental and numerical study is carried out on the use of UHPC for connection regions of CFT. A new connection is proposed for CFT to precast footing which strategically uses UHPC in the connection region.

1.5 Objectives and Methodology

Many ABC technologies have been developed for pier construction including prefabricated piers and precast segmental columns. These prefabricated columns require development of connection details which can safely transfer loads to the adjacent capacity protected element. In this respect, extensive research is available on different connection details of these elements with concrete footing and cap beams. However, similar connections for CFT may not be feasible. There is a need to develop ABC connections for CFT which conforms to the design philosophy of current specifications. The use of CFTs in ABC technologies can benefit the construction industry by providing alternate structural elements which have both structural strength and ductility especially for high seismic regions such as California.

Significant research efforts have been carried out on CFT column behavior under different loading conditions and various guidelines and codes provide design expression for the CFTs including AASHTO and AISC. Recently, there has been an increase in research efforts on CFT to precast concrete elements especially for ABC applications. However, the inelastic behavior of these connection details under seismic forces has not been investigated.

The focus of this research is development of a new connection details for CFT to precast concrete. Besides precast elements, the recent advent of UHPC shells has opened new ABC solutions for cap beams. These precast shells can be used with CFT to further accelerate on-site construction. The objectives of the research are tabulated below:

- Conduct a state-of-the-art literature review and comprehend the recent developments in the area of connections to CFT columns.

- Carry out a set of pretest finite element tests to complement the design of shear connectors based CFT connections and understand the behavior of connectors under different loading.
- Carry out experimental work on scaled down model to study on a set of new CFT connection details under axial and lateral cyclic loading.
- Develop non-linear finite element models for the connection details and calibrate the model with the results of the experimental study. Using the calibrated numerical model, carry out a parametric study on various connection details.
- Propose preliminary recommendations for field application of the connection.

The increased demand for development of new ABC connections for CFTs require an elaborate experimental and numerical research to comprehend the behavior and develop design guidelines. A detailed experimental and numerical work is carried out to comprehend the behavior of CFT connections with precast elements.

1.6 Organization of dissertation

This study presents results of large scale testing and numerical study on connection details and recommendations for field implementation. The dissertation is organized in following chapters:

Chapter 1 provides an introduction to accelerated bridge construction and briefly discusses high speed rail developments in the U.S. Also, the chapter highlights the inherent benefits of concrete filled steel tubes and research needs required for its ABC applications for high speed rails.

Chapter 2 - This chapter presents a comprehensive review of CFT connections. Past literature and objective findings of the failure modes were studied, and a new

set of connection detail is proposed. The design parameters for CFT connections are presented and complemented with pretest finite element analysis on connection details.

Chapter 3 - Utilizing the outcomes of pretest finite element analysis, a select detail of connection was studied in a large scale experimental program for CFT to precast concrete connections. The experimental program consisted of the three proposed connection details which were studied under axial and lateral cyclic loading. The chapter presents the failure modes, load-drift, strain response and a comparison of performance of the connection detail.

Chapter 4 - The results of experimental program are used to calibrate the numerical models and a parametric study is carried out on different details for each specimen. Using the calibrated models, the behavior of the connections is predicted. The investigated parameters include material properties, axial load level and boundary conditions.

Chapter 5 - Presents and summarizes the outcome of the research endeavor. Recommendations for future work and field implementation of the connection are made.

CHAPTER 2

LITERATURE REVIEW AND PRETEST NUMERICAL STUDY

2.1 Introduction

A number of details for CFT connection have been used in practice. Figure 2.1 shows the schematic of some of the commonly used connections which includes: a) encased connection, b) embedded connection, c) exposed base plate connection, d) semi-embedded connection, and e) embedded ring connection. The most common type of connection detail consists of exposed connection and embedded connection. Each of these connections have advantages and disadvantages associated with them.

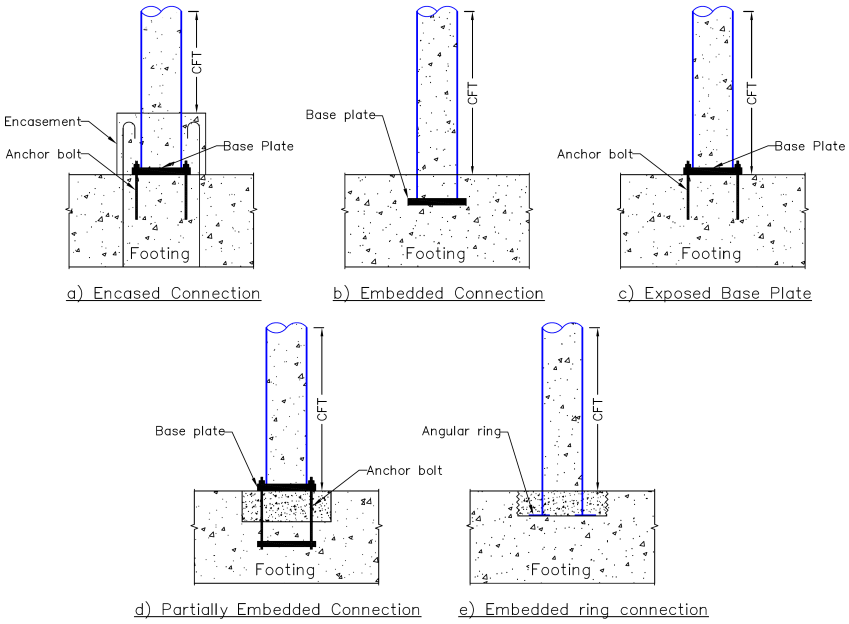

Figure 2.1: Schematic of commonly used CFT connections [28]

Table 2.1 presents a summary of tests carried out by previous researchers on different connection types along with their details and failure modes. A brief summary is provided for some of these connections to develop an understanding of construction issues, research outcomes and target parameters for design of a new connection.

Table 2.1: Previous experimental studies on CFT connections.

Type	**CFT**	**Connection Detail**	**Failure Mode**
Encased [29]	Hex	Concrete encased	Tube buckling
Embedded [30]	Round	Base plate-studs	Cracking - Tube buckling
Embedded [31]	Square	Anchors - stiffners	Buckling
Encased [32]	Circular	Anchors - Deformed bars	Anchor failure - Buckling
Embedded [22]	Circular	Annular ring	Buckling - Tearing of tube
Encased steel [33]	Circular	Channels - Plates	Local Buckling
Semi-embedded [34]	Square	Base plate - anchors	Cracking - bolt yield
Encased [35]	Circular	Steel wraps - Studs	Shear cracking - Buckling

The following chapter reviews some of the state-of-the-art literature for CFT connections and their limitations for ABC applications. Building upon the shortcomings of existing connections and availability of advanced materials such as ultra-high performance concrete(UHPC), a new connection is proposed for further investigation.

2.1.1 Baseplate Connections

A baseplate connection is the commonly used among all CFT to base connections. This type of connection consists of attaching a base plate on the bolts which are pre-installed in the concrete member. The main advantage of this type of connection is easy and fast construction but the positioning of bolts and anchors requires larger construction tolerances. The exposed connection relies entirely on anchor bolt and thick end plate, both of which are vulnerable to damage during earthquake loading. Different failure modes for baseplate connection include cracking of concrete, bolt failures, and buckling of the steel plate. An extensive research data is available on the behavior of baseplate connections in which researchers have investigated different anchor size and materials, baseplate arrangement and configurations, strength of concrete and grouting, etc.

Experimental study by Qiao et al. [36] used threaded anchors (shown in Figure 2.2) at the periphery of square columns and additional high strength embedded reinforcing bars. The placement of anchors externally increased the bending capacity and rotation stiffness of the connection. The failure mode include cracking in grout, yielding of bolts and buckling of the steel tube. Christoper et al. [37] carried

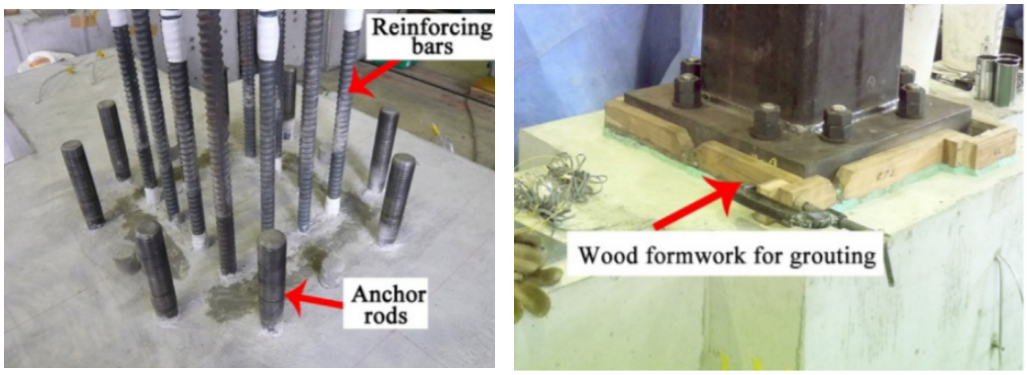

Figure 2.2: Baseplate connections with anchor bolts [36]

out testing on baseplate connections with W-section column and concluded that the failure modes under seismic loads are dependent on baseplate setting and stretch length of anchors. Similar test results were obtained by Lim et al. [38] who carried out testing on column base connections. Results showed that the behavior of the connection is mainly dependent on the thickness of base-plate. Authors, however, point out that the design of plain round anchor for $30d_b$ may still undergo slippage. For deformed rebars the provisions of ACI code can be used to design the embedment depth.

The baseplate connections are mainly used for joining column sections to the concrete bases, light pole columns and installation of industrial units to pedestals. The column erection in this connection is complex which requires selection for setting method of anchor rods, grouting procedures, etc [39]. The minuscule detailing makes this connection tedious for bridge substructure applications.

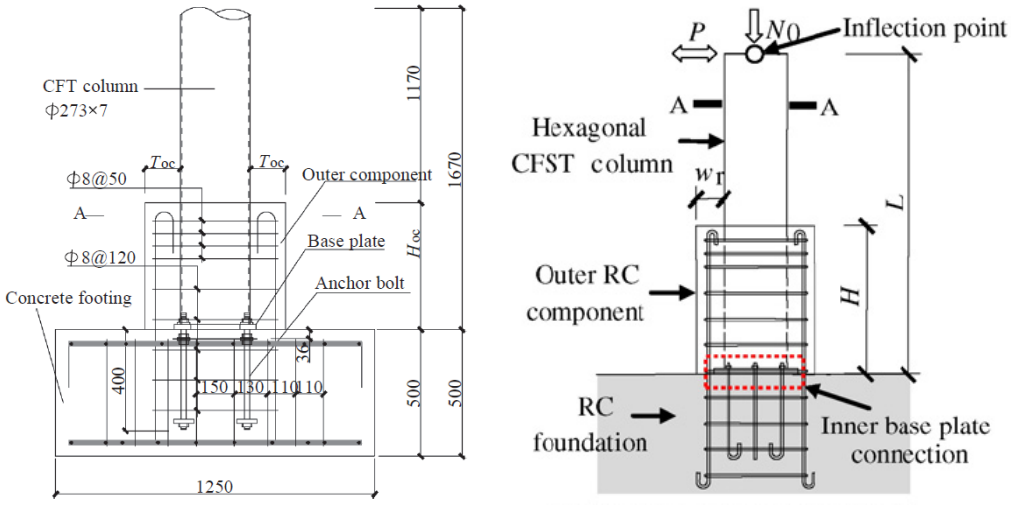

(a) Encased connection [40] (b) Encased connection [29]

Figure 2.3: Encased connections with outer component.

2.1.2 Encased Connections

Encased connections consist of steel tube which is partially enclosed in a layer of encasing material (typically reinforced concrete). Encased sections have been used in seismic regions due to their improved strength and stiffness. Most of the applications for encased connections are for high rise buildings and industrial structures. The construction complexity of encased connection is moderate when compared to embedded or base plate connections. The failure mode for these encased connections mainly depends on the geometric and material properties of the encasing layer.

Xian et al. [40] studied steel wrapped reinforced encased connections, shown in Figure 2.3a, under seismic loads. In this study shear studs were used which resulted in an improvement of bond behavior between CFT and encasement. The specimens failed either by buckling or shear cracking of encasement layer. The shear cracking of encasement was prevented by providing steel wraps.

Wu et al. [29] carried out experimental study on twelve hexagonal encased connection under constant axial and cyclic lateral load shown in Figure 2.3b. Six

Figure 2.4: Grouted shear stud connection [41].

groups of test specimen were tested with one of them using studs between CFT and outer component. The failure of concrete encasement and buckling failure of column were both observed in the specimens. The specimen with shear studs exhibited improved composite behavior resulting in an increase in elastic stiffness, maximum strength and ductility coefficient.

Grouted socket type connection, shown in Figure 2.4, was developed by Fulmer et al. [41] for ABC applications. The outer region between the outside stub and pipe column was grouted and studs facilitated the force transfer at the connection. The authors rationalize the use of shear studs due to lower encasement depth and which may be waived if deeper outside stub is used. The results showed desirable behavior with damage located away from the capacity protected element. Kim et al. [32] experimentally evaluated different types of CFT to foundation connections and compared the effectiveness of different details. Five connection details were considered with different combinations of high-tension bolts, deformed bars, and anchor frames, etc. Different types of connections were joined with an external base plate frame which encased the bottom of the CFT column. Results showed that all columns exhibited local buckling along with anchor failures. The high-tension bolts exhibited superior structural performance when compared with anchor bolts or anchor frames.

2.1.3 Embedded Connections

Embedded connection consists of partially placing the steel tube inside the concrete component. This connection requires recess opening in the precast element which is then filled with cementitious material. The embedment length of CFT inside the concrete has a significant effect on the behavior of the connection. All test results of embedded CFT connection to concrete element show that the longer embedment depth of the tube results into achieving higher drift capacities [22] and an improvement in rigidity of the connection [31]. The embedded connection generally performs better as additional resistance is contributed by the steel tube and the concrete. However, the embedded connection can sustain crushing in the vicinity of the steel plate under seismic forces which reduces its structural performance.

Hsu et al. [31] proposed a new type of connection, shown in Figure 2.5a, for square CFT by strengthening the embedded connection with stiffeners which would minimize the tendency of concrete to crush. The experimental results, under combined axial and lateral load, showed that the embedment improved the structural behavior of the connection and an addition of stiffeners improved the energy dissipation capacity.

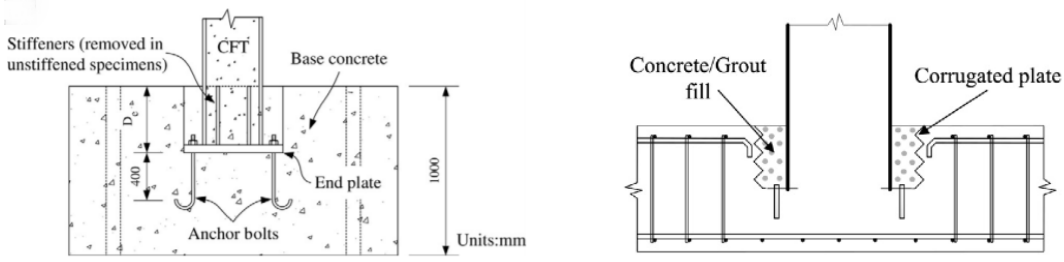

(a) Embedded connection [31] (b) Embedded connection [42]

Figure 2.5: Configuration of embedded connections.

Lehman et al. [22] carried out an experimental study on CFT to foundation connections (Figure 2.5b) to evaluate ductile connections of CFT without the use of

any dowels or internal reinforcement. The research used grouts to fill the voids once the CFT is placed in a precast member. In this case, a high-strength fiber-reinforced grout was filled to achieve composite action.

Xiao et al. [30] carried out testing on two CFT column base connections; one which used a stiffener - base plate detail and the second one using welded studs. The connections were tested under combination of constant axial and horizontal cyclic force. Despite the difference in force transfer mechanism, both connections were able to develop full plastic hinging up to drift levels of 6% after which the CFT failed by steel rupture. The connection showed a stable hysteresis response and sufficient energy dissipation; however, the specimen did sustain limited damages to the concrete base.

Marson et al. [34] used a fixed base detail with encased (embedded in concrete) steel C-sections and steel tube welded to end plates. The detail was designed without the use of any reinforcing bars and the channels and plates were used to transfer the moment from the column. The specimens were tested under axial and cyclic load. Results showed that all specimen exhibited good energy dissipation and reached a 7% drift ratio after which the tubes ruptured. The concrete footing with embedded C-sections and steel plates did not undergo damages. The partially embedded and ring type are variations of encased and base plate connection. The design, construction and behavior of these connections are also similar to their parent connection; therefore, for sake of brevity, these are not discussed in detail.

2.2 CFT Connection for ABC applications

In buildings, CFT to steel beam connection has been extensively evaluated and used in practice [43]. However, in bridge design, there is a lack of connection design

for CFT to foundation and pier cap which hinders the use of CFT (especially in the U.S). Recently, research efforts in the U.S. have increased for developing design recommendations on connection of CFT in bridge structures particularly by the Washington Department of Transportation [44].

Design of connection is one of the most important parts of structural design particularly for bridges located in high seismic regions. The column to footing connection must achieve sufficient strength and ductility to dissipate energy due to earthquake events. In the current design guidelines for bridges, a capacity design approach is used for column design in which the column's ultimate capacity is used to estimate the capacity of footing and cap beam. This implies that the column and connection design control the member size and structural design of the cap beam and footing. The connection of steel tube with foundation or pier cap is to be designed to prevent any premature failure.

Stephens et al. [45] carried out an extensive experimental study on the connection of CFT column with precast concrete elements. The authors proposed different connection details (Figure 2.6) for foundation and cap beam which were numerically and experimentally tested and design expressions were proposed [45].

2.3 Ultra-High Performance Concrete Based Connections

Reinforced concrete (RC) is a widely available construction material and its dominant use in built structures is mainly attributed to its low cost and material characteristics. In bridge infrastructure, however, the RC structures can be exposed to deleterious agents which may render them susceptible to deterioration [46] [47]. The enhanced service life of these structures demands periodic inspections and maintenance which is time consuming and costly [48] [49].

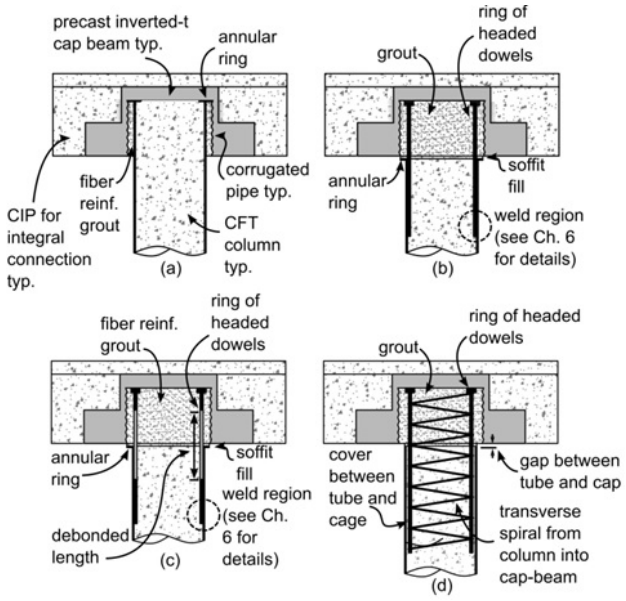

Figure 2.6: ABC connections for cap beam [45].

UHPC is an advanced cementitious material which offers excellent durability and mechanical characteristics [50] [51]. UHPC offers higher compressive and tensile strengths if compared to normal concrete. The improvement in tensile strength is almost 2 to 3 times while the compressive strength can reach up to five times of normal concrete [52]. Due to the low water to binder ratio and optimized packing, UHPC has a dense micro-structure which reduces porosity and permeability. Testing on the chloride diffusion coefficient of UHPC has shown that the material exhibits 30-600 times lower rates than higher performance concrete and normal concrete [53] [54] [51]. Pyo et al. [55] evaluated abrasion resistance and results showed that the UHPC has at least 3 to 7 times lower abrasion if compared to high strength concrete and normal concrete. Thus, an encasement of UHPC can preemptively protect against chemical attack due to low chloride intrusion of the material. Also, the concrete fill is structurally integrated with the UHPC formwork which can improve the structural performance. UHPC has been used for many bridge applications including retrofitting, repair, and construction of new elements [26], [25], [56].

The embedment requirement for reinforcing steel in UHPC requires eight times bar diameter ($8d_b$) which is less than what is required for the normal strength concrete (NSC). Recent research activities have used UHPC for connecting different bridge elements [27]. The use of UHPC for connection of precast concrete columns has been investigated by Shafieifar et al. [57]. The UHPC band at the interface of concrete column to cap beam shifted the plastic hinge away from the capacity protected element. Tazrav et al. [58] experimentally evaluated the connection of RC column to footing using duct connection incorporating UHPC and concluded that the connection was emulative of conventional connection.

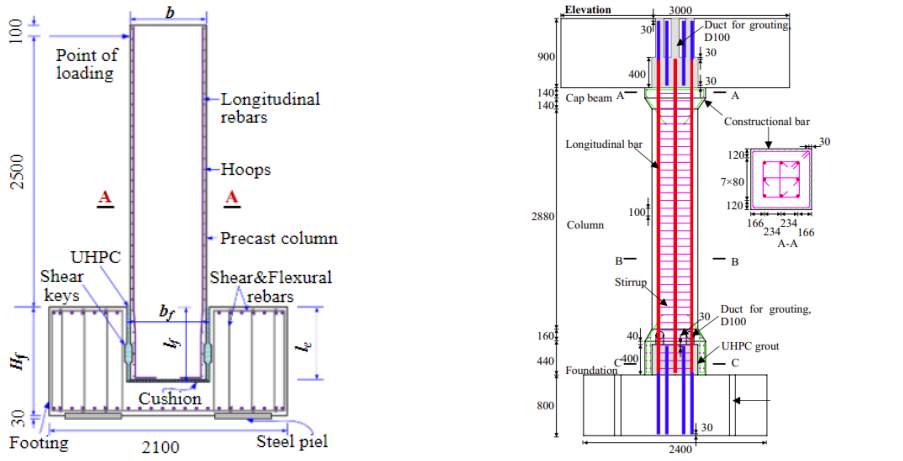

(a) UHPC socket connection [59]. (b) UHPC pocket connection [60].

Figure 2.7: UHPC pocket and socket connection.

Zhang et al. [59] tested 1:3 scale UHPC socket reinforced column-foundation connection and results were compared with CIP specimen. Four specimens were designed to check the effect of shear key in joint area and embedment length as shown in Figure 2.7a. An embedment depth of 0.8 x width of precast column was considered emulative of a CIP connection. Wang et al. [60] tested a pocket connection for precast column to cap beam and foundation and compared results to a monolithic connection detail. The pocket specimen consisted of lap-spliced reinforcing bars and the cavity is filled with UHPC as shown in Figure 2.7b. Similar to socket connection,

the pocket connection performance was also emulative of a monolithic reinforced column. Mohebbi et al. [24] also carried out investigation on pocket connection with UHPC for bent caps and found that 1.0 times the column section in cap beam pockets was sufficient to develop column plastic moment. The connection was subjected to successive motions simulating scaled versions of the 1994 Northridge-Sylmar earthquake and comparison with reinforced concrete column showed that UHPC reduced plastic hinge damage.

Based on the literature research, the effectiveness of the embedded and encased connection has been demonstrated by many researchers. These connections can be further improved upon using UHPC at critical sections of the section. Based on these advantages, a new concept for CFT connection is envisioned to develop the full flexural capacity of the CFT which can undergo large displacement ductility. The details of the proposed connection and construction sequence are presented in the next section.

2.4 Proposed Connection

The test results have shown that the exposed steel base connections with anchor bolts are prone to failure through yielding or pull-out of the anchors. For encased and embedded CFT connections, the surrounding concrete and the steel tube contributes to additional resistance, and therefore these connections provide larger strength and stiffness when compared to base plate connections. Therefore, for ABC applications, embedded and encased connections are more promising when compared to other types of connections. These connections require recess openings which are then filled with cementitious material such as UHPC or grout.

Based on similar principles, a new concept for CFT connection is envisioned to develop the full flexural capacity of the CFT which can undergo large displacement ductility. The new connection consists of CFT embedded in the precast member and encased within a layer of UHPC. The embedment depth filled with UHPC inside the precast element provides structural strength and an encasement outside the concrete ensures that the plastic hinge is outside the footing which is typically designed as a capacity protected element. Additional dowels near UHPC layer perimeter are designed to accommodate the force transfer in the connection.

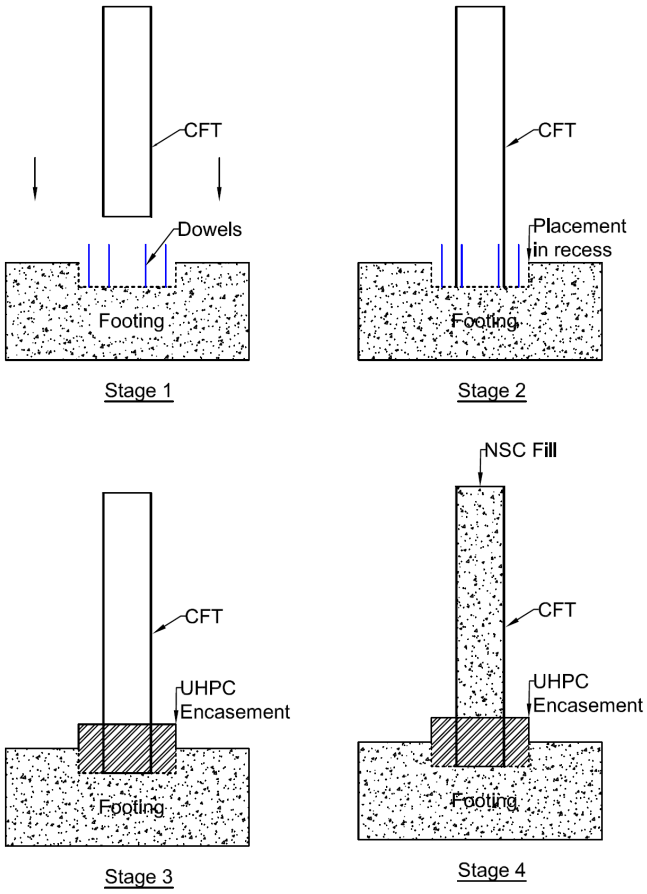

Figure 2.8: Construction sequence of proposed connection detail.

Figure 2.8 shows a schematic of the construction sequence. A recess, larger than the diameter of CFT, is formed in the precast RC element with a corrugated

interface. Internal and external dowels in the recess are developed in the concrete footing. Next, the CFT is placed inside the recess between the dowels. The recess inside the precast element and an additional outside encasement is filled with UHPC. In the final stage, the remaining CFT column is filled with NSC. To resist slippage and improve the transfer of forces from CFT to UHPC, different details can be used such as the inclusion of shear connectors, threaded rods, ring plates or a combination of these. The embedded layer is designed for pullout resistance and the precast concrete is checked for punching shear. The depth of the UHPC layer is controlled by the anchorage requirements of the dowels. On the other hand, the diameter of the UHPC layer should be adequate to provide a cover of at least three times dowel diameter ($3d_b$) for perimeter dowels. The sequence of construction is suitable for ABC applications for construction of footings and cap beams.

2.4.1 Moment Curvature Analysis

Moment curvature analysis is used to represent the behavior of a structural cross-section using nonlinear stress strain relationships of the constituent materials. The moment curvature analysis is typically performed using commercial software, but the validity of these analysis depends on the available stress-strain relationships.

In order to design the experiment, the moment capacity of the steel tube was estimated using analytical approach where the curvature is incrementally increased, and location of neutral axis is iteratively determined for each curvature [61]. Initially, the neutral axis is obtained using force equilibrium. The forces acting on the section consist of compressive and tensile force in tube and concrete. The tensile stress in normal concrete is ignored and since the concrete is confined inside the tube, the analytical approach uses confined concrete model proposed by Mander et al. [62].

Based on this model, the confined compressive strength is given as follows:

$$f_{cc} = f'_{co}(-1.254 + 2.254\sqrt{1 + \frac{7.94f'_l}{f'_{co}}} - 2\frac{f'_l}{f'_{co}}) \tag{2.1}$$

Where f'_{co} is the unconfined compressive strength. For the constitutive model of steel, rigid-ideally plastic material is assumed [61].

$$f_{yt} = 1.05\, f_y \tag{2.2}$$

$$f_{yc} = 0.95\, f_y \tag{2.3}$$

Since the anticipated fracture of tube was anticipated outside of the UHPC region, confined UHPC stress-strain was not considered in calculation of moment curvature. For proof of concept, a commercially available diameter for CFT was chosen for experimental program. The tube used for the study consists of $d = 12.75\, in.$ and $t = 0.25\, in.$ The moment curvature is plotted in Figure 2.9 with a set of concrete strength $f'_c = 4$ to $6\, ksi$ and $f_y = 40$ to $50\, ksi$. Using the results of these analysis, different parameters of the experiment were designed.

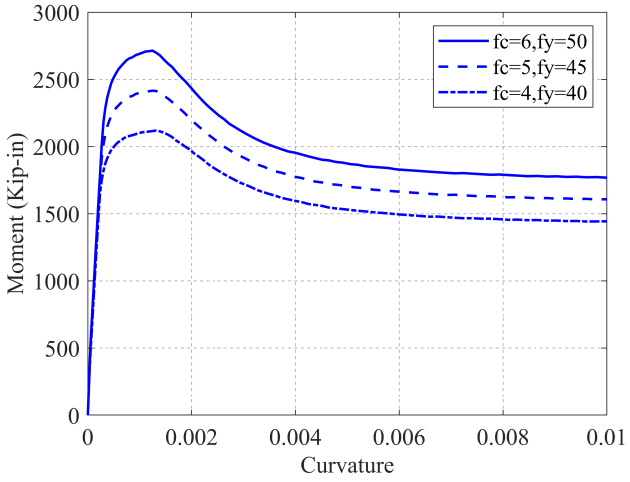

Figure 2.9: Moment curvature for CFT tube with $d = 12.75\, in.$ and $t = 0.25\, in.$

2.4.2 P-M Interaction Curves

The P-M interaction curve is calculated using the procedure outline by Perea et al. [63]. In this procedure, the axial and flexural strength is based on plastic stress distribution method. The method assumes that the steel section can develop fully plasticity for both compression and tension. The contribution of concrete in tension is not considered and the compression is adopted using an equivalent block concept (F_c) which is given by following equation:

$$F_c = 0.85(f'_c + \frac{1.558\, F_y t}{D_c}) \leq 0.9 \tag{2.4}$$

The squash capacity is calculated using the material properties of concrete and steel using the following equation and the corresponding strength is calculated by multiplying with strength component:

$$P_o = P_c + P_s = A_s\, F_y + A_c\, F_c \tag{2.5}$$

The pure tension capacity is calculated using the strength of steel tube using following equation:

$$T_o = -\, P_s \tag{2.6}$$

The plastic stress distribution is shown in Figure 2.10 for a given position of plastic neutral axis [63].

This method can be used to plot different points of the P-M interaction curve using a continuous function provided as follows:

$$P_{cs}(y) = (\theta(y) - \pi)K_s + (\theta(y) - sin\theta(y))K_c \tag{2.7}$$

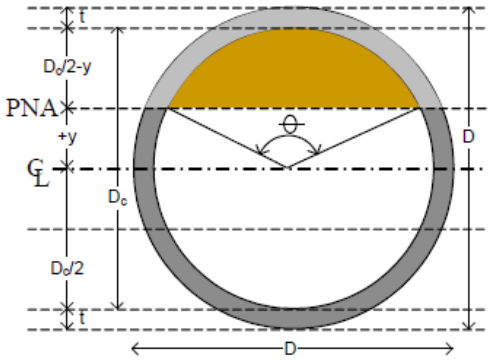

Figure 2.10: Plastic stress distribution in a circular concrete filled steel tube for a given plastic neutral axis position [63].

The K_s and K_c correspond to steel and concrete parameters, respectively. The effect of material strengths on the plots in shown in Figure 2.11. The plots are made for a $d = 12.75 in.$ and $t = 0.25 in.$ The graph shows that moment and axial capacity of the section can be significantly increased with increase in material strength.

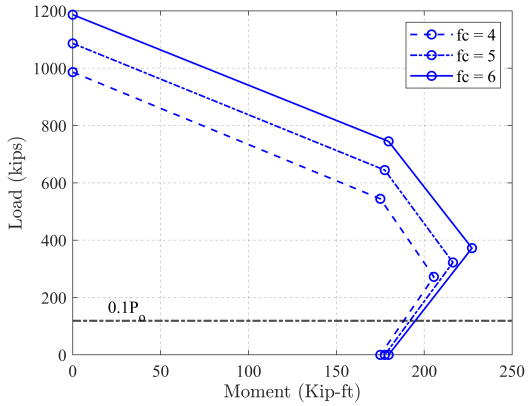

(a) Effect of f'_c

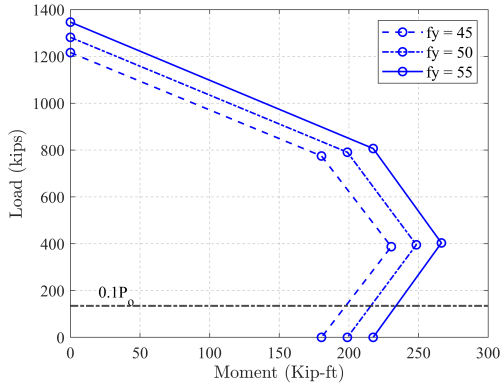

(b) Effect of fy

Figure 2.11: P-M interaction curves for different a) concrete strength and, b) yield strengths of the steel tube.

2.5 Pretest Finite Element Analysis

Finite element (FE) modeling has been used in structural engineering to comprehend and understand the behavior of elements under different boundary and loading

conditions [64] [65]. Before carrying out large scale experimental study on the connection, a pretest FE analysis was carried out.

Moon et al. [66] carried out an analytical study on prior experimental results for concrete filled steel tubes. Moon et al. [42] carried out FE on monolithic embedded CFT connections. The analytical result from this research showed that embedment length had significant effect on the connection and diameter-to-tube thickness (d/t) ratio did not impact the results for well anchored tubes. Based on experimental studies, Han et al. [67] carried out FE analysis to simulate response under seismic loading on reinforced concrete encased connections for CFT. Five different failure modes were observed, and the reinforced encasement improved the response of the structure. Also, shear studs, modeled as nonlinear springs, resulted in an improvement in calibrated results.

Another embedded connection was experimentally and numerically studied by Park et al. [68] for modular embedded in a recess which was later filled with mortar. Monotonic load was applied to the models and results showed that large compressive stresses are developed between CFT and footing which is resisted by footing concrete. Stephens et al. [20] also applied monotonic loading to investigate the effect of different parameters on CFT to cap beam connections. To limit the computation time, the most researchers do not consider cyclic loading.

The accuracy of the FE model is dependent on various factors including material models, element type, mesh details, loading and boundary conditions. There is a need to carry out a comprehensive FE analysis on CFT connections using realistic boundary and loading schemes. Experiments from existing literature are used to model and calibrate material models, modeling parameters, etc. The 3D FE was performed using static structural suite in ANSYS [69]. The details of the FE model are provided.

2.6 Material and Element Definitions

2.6.1 Steel Reinforcement

The reinforcement bars were modeled using 3D discrete reinforcing elements (REINF264) available in ANSYS mechanical [69]. This element type uses a 3D base element and defines a reinforcing fiber with respect to the base element's coordinates. The reinforcing element has uniaxial properties (similar to links or truss elements) however shares the same nodes as the base elements. A schematic of the reinforcement element for an 8-node base element as defined by Ansys is shown in Figure 2.12.

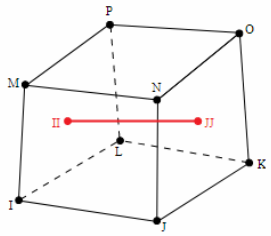

Figure 2.12: Schematics of 8-node REINF264 element in ANSYS [69].

The stress-strain behavior of the steel reinforcement was modeled using bi-linear isotropic hardening plasticity as shown in Figure 2.13. The material definition is by an initial yield surface (in terms of yield stress) and a tangent modulus for the post-yield behavior. The defining parameters of the material properties for the steel reinforcement are provided in Table 2.2.

Table 2.2: Material definition of steel reinforcement

Parameter	**Value**
Modulus of elasticity (ksi)	29000
Poisson ratio	0.3
Yield stress (ksi)	69.7

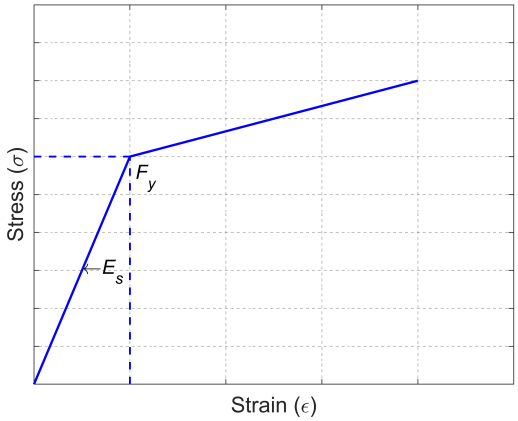

Figure 2.13: Bi-linear model of steel.

2.6.2 Structural Steel

Ansys allows modeling of thin to moderately thick shell structures with SOLSH190 element as shown in Figure 2.14. Like 3-D solid, this element has eight nodes each with three degrees of freedom. SOLSH190 is fully compatible with 3-D constitutive relations. Compared to classical shell elements that are based on plane stress assumptions, SOLSH190 usually gives more accurate predictions when the shell is thick.

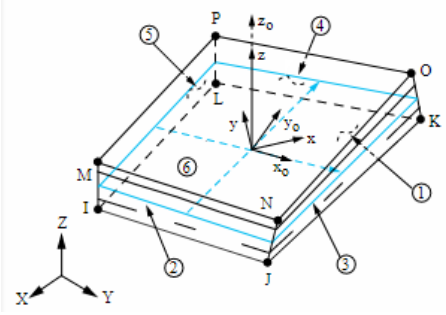

Figure 2.14: SOLSH190 geometry [69].

Shear connectors were modeled with Solid185 which is a 3-D element with eight nodes and each node with three degrees of freedom. The element has plasticity, hyper-elasticity, stress stiffening, creep, large deflection, and large strain capabilities [69]. The stress strain diagram for shear connector is shown in Figure 2.15.

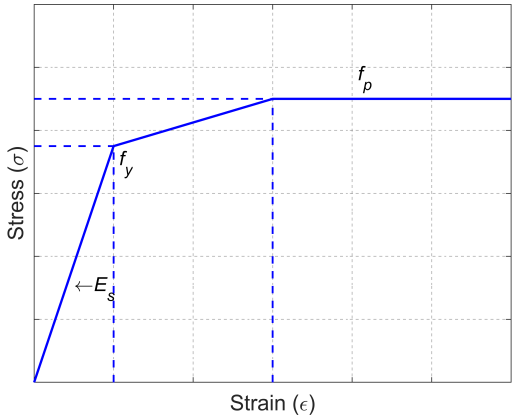

Figure 2.15: Stress stress for stud.

2.6.3 Microplane Model for Concrete and UHPC

Concrete exhibits a complex behavior owing to its constituent materials such as aggregates and cement matrix. The material exhibits plasticity, micro-cracking, concrete crushing, and a generalized formulation of a constitutive model for nonlinear behavior is difficult. A validated material model for normal strength concrete was used. The coupled damage plasticity micro-plane model with the parameters defined in the Table 2.3 was used for modeling concrete materials. The microplane model is based on plasticity-damage framework which is aimed for dimensional damage and fracture analysis [70]. In this algorithm, induced anisotropy is induced in both plasticity and damage. Figure 2.16 shows the microplane cap yield function which is based on Drucker-Prager function and introduces caps for both compression and tension regions [71].

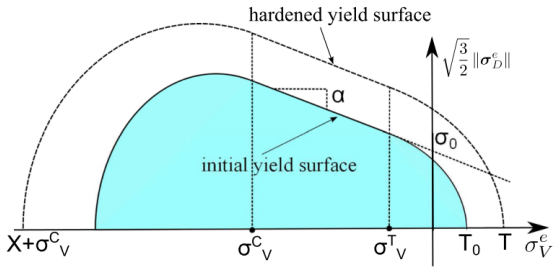

Figure 2.16: Smooth three-surface microplane cap yield function [71].

CPT215 element is used for microplane which is a 3-D eight node coupled physics element with translational degree of freedom at each node as shown in Figure 2.17.

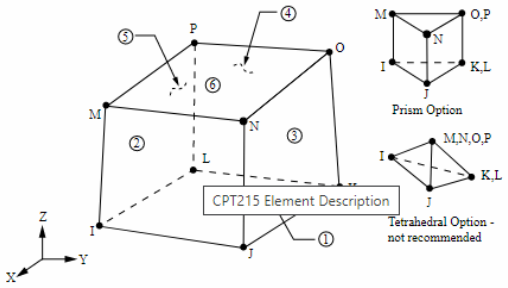

Figure 2.17: Schematics of 8-node CPT215 element in ANSYS [69].

Table 2.3: Material definition of NSC

Parameter	**Value**
Uniaxial compressive strength, f_{uc} (MPa)	$1.2f'_c$
Biaxial compressive strength, f_{bc} (MPa)	$5f_{uc}$
Uniaxial tensile strength, f_{ut} (MPa)	f_{cr}
Intersection point abscissa between compression cap and Drucker-Prager yield function (MPa)	$-2/3f_{bc}$
Ratio between the major and minor axes of the cap	2
Hardening material constant (N^2/mm^4)	1
Tension cap hardening constant	20000
Tension damage thresholds	0.003
Compression damage thresholds	0.001
Tension damage evolution constants	80
Compression damage evolution constants	2000
Nonlocal interaction range parameter (mm^2)	30
Over-non local averaging parameter	1

2.7 Calibration Study

The specimens consisted of CFT which was partially filled with the UHPC at the location of the connection while the remaining portion of the steel tube was filled with NSC. A model validation through comparison with existing results from literature was carried out to understand confinement effect of composite column for both

NSC and UHPC. An emphasis is given to performance of shear connectors in UHPC and normal concrete under different loading conditions. Existing experimental data was used to understand the effect of material properties, geometry, and modeling techniques on performance of shear connectors. The outcomes of this pretest numerical analysis is then used to perform a calibration and parametric study on the column connection.

2.7.1 Normal Strength Concrete Confined by CFT

Schneider [72] tested a series of concrete filled stub columns subjected to compressive loading to investigate effect of wall thickness and shape of steel tube on ultimate strength of CFTs. Although, square and rectangular stub columns were also tested, numerical study was limited only to circular stub columns. Two circular stub columns from the study were used for calibration of the portion of the tubes filled with NSC. The D/t ratio of the specimen C1 and C2 were 47 and 21, respectively, while the L/D ratio was 4.3 for both of them. The detailed material properties of steel and concrete are referred to the literature [72]. The specimens were tested under concentric axial compression using a stiffened end cap placed at the top and bottom of the specimen.

The two stub columns were modeled using the Ansys and consist of a circular concrete filled tube filled with NSC. The concrete was modeled using CPT215 element and the steel tube was modeled using SOLSH190. The stiffened caps were modeled using linear structural steel material with Solid185 elements. The column was constrained at the bottom cap using fixed conditions. A friction contact was modeled between the steel tube and the core concrete with a friction coefficient of 0.4. A displacement was applied to the top stiffened cap and vertical displacement

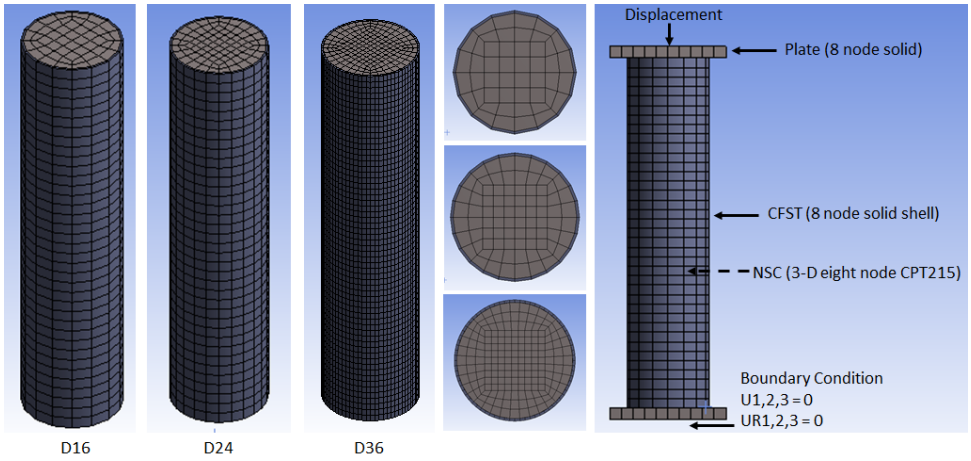

Figure 2.18: Finite element model for NSC confined by steel tube.

was monitored for corner nodes of top cap. The meshed model and boundary conditions are shown in Figure 2.18. A mesh refinement study was carried out. The results of the experiment and FE analysis are compared in Figure 2.19 and shows a good agreement.

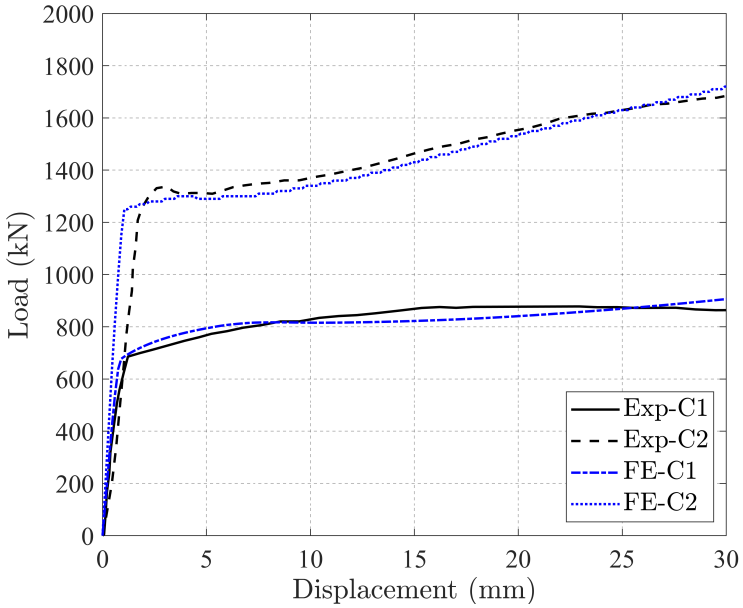

Figure 2.19: Comparison of numerical and experimental results of Schneider et al. [72].

2.7.2 Push-out Test for Shear Studs

Although, extensive experimental data is available for push-out behavior of shear studs embedded in normal strength concrete, only a handful number of experiments have been conducted on shear studs connected to steel sections and embedded in the UHPC.

Cao et al. [73] conducted experimental study on push-out behavior of shear studs in UHPC. The push-out tests were conducted on an I-shaped steel section embedded in two adjacent layers of UHPC. The geometry, material properties and loading protocol for the experiment are derived from the literature [73, 74]. For the 3D model, CPT215 element is used for modeling of UHPC, while the steel plate was modeled using the solid shell elements. The reinforcement is represented as 2d beam elements. The geometry was created using the SpaceClaim modeler. Due to high computational requirements, the model was sliced along orthogonal axis. In Ansys, symmetry region option is selected which prevents out of plane displacements at user defined axis. The FE model is shown in Figure 2.20.

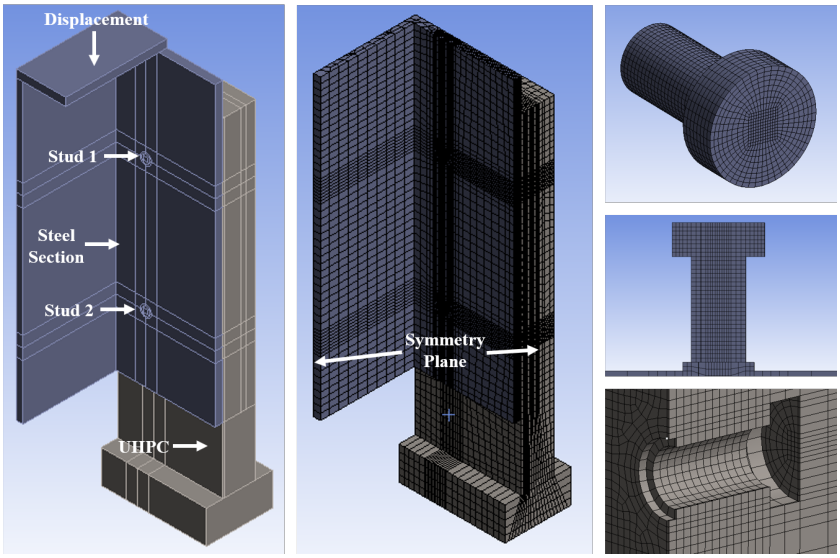

Figure 2.20: Finite element model of push-out test setup with weld collar [73].

A remote displacement is applied at the top reference surface. The model is constrained at three translational degrees of freedom at the bottom surface of the UHPC layer. The interaction surfaces between steel plate-to-UHPC and UHPC-to-shear studs was modeled using a frictional contact. The friction of coefficient was taken as 0.4 [74]. In order to verify the effect of weld, two models were considered i) without weld collar and, ii) with weld collar. Without explicitly modeling the weld collar, the load-slip shows a softer response. Figure 2.21 shows the load-slip comparison of experimental and numerical model. The slip is defined at the location of the shear stud and is an average relative displacement of UHPC layer and steel section.

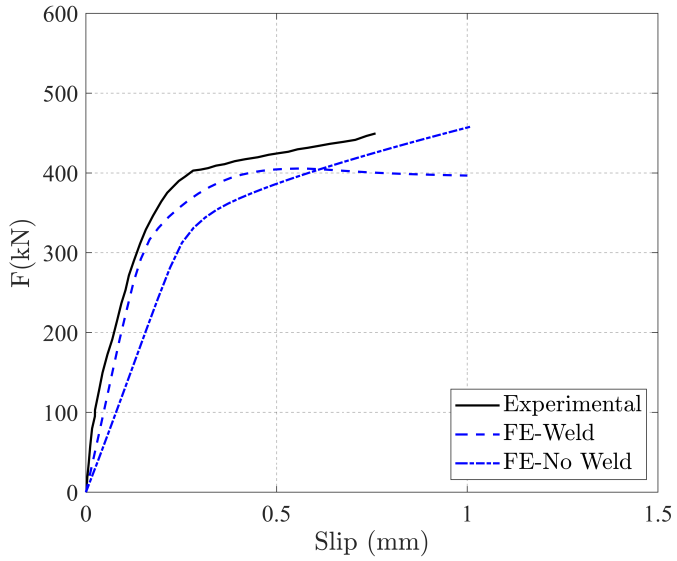

Figure 2.21: Comparison of load-slip for experimental and numerical models.

It can be observed that the load-slip behavior of case (i) without weld collar and (ii) with weld collar showed slight differences. For case (i), the model showed a relatively softer response. The increase in slip is linear for both cases while non-linear behavior of stud results. The compression and tension damage in the UHPC layer are plotted in Figure 2.22. The compression damage shows that the UHPC is

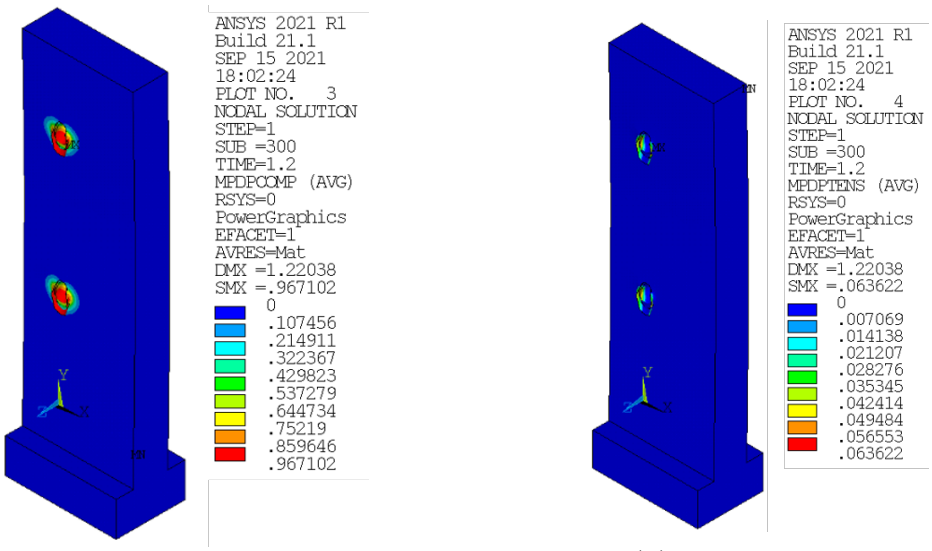

(a) Compression damage

(b) Tension damage

Figure 2.22: Damages in UHPC layer at location of shear studs.

extensively damaged in the direction of the push out loading while tension damage is observed at the opposite side. The evolution of principal stress in shear studs is shown in Figure 2.23. For sake of clarity, the surrounding concrete is deactivated. It can be observed that the weld collar and bottom of shank undergo maximum stresses at the onset of loading and progresses upwards in the shank. Also, it was observed that the first layer of shear stud contributed more in stress.

2.7.3 Stud Pull-Out Tests

For composite members, the stud connectors are subjected to different loading conditions. A composite action is expected to be achieved between studs and adjacent concrete member under a combination of different loading conditions. In this section, pull out tests which simulate tension loads are modeled and which are used for understanding the behavior of the shear connectors embedded in concrete. After the model is calibrated, the behavior of stud embedded in UHPC is studied using calibrated material model for UHPC.

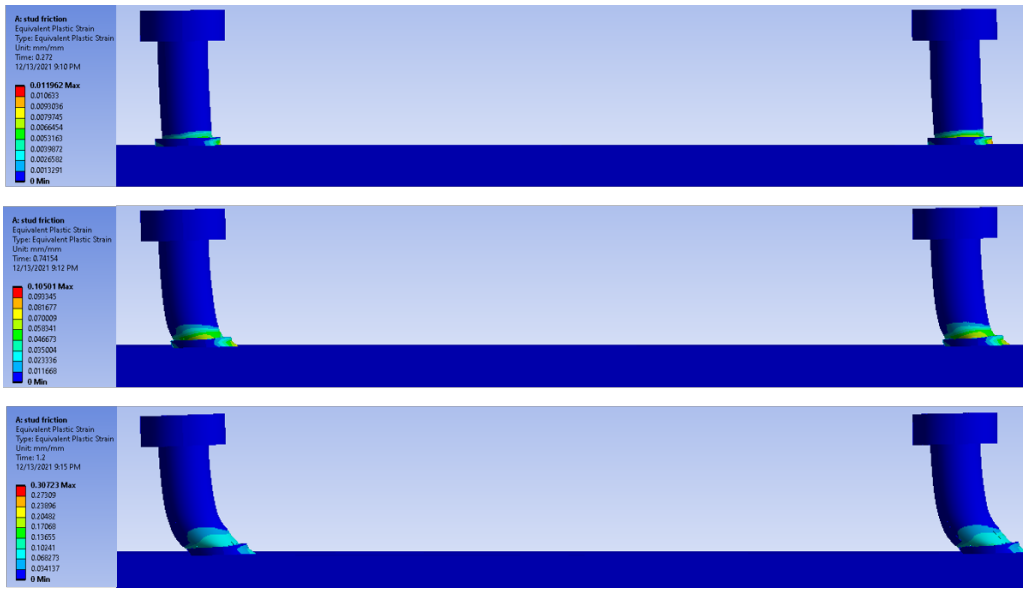

Figure 2.23: Evolution of principal stress in shear connectors.

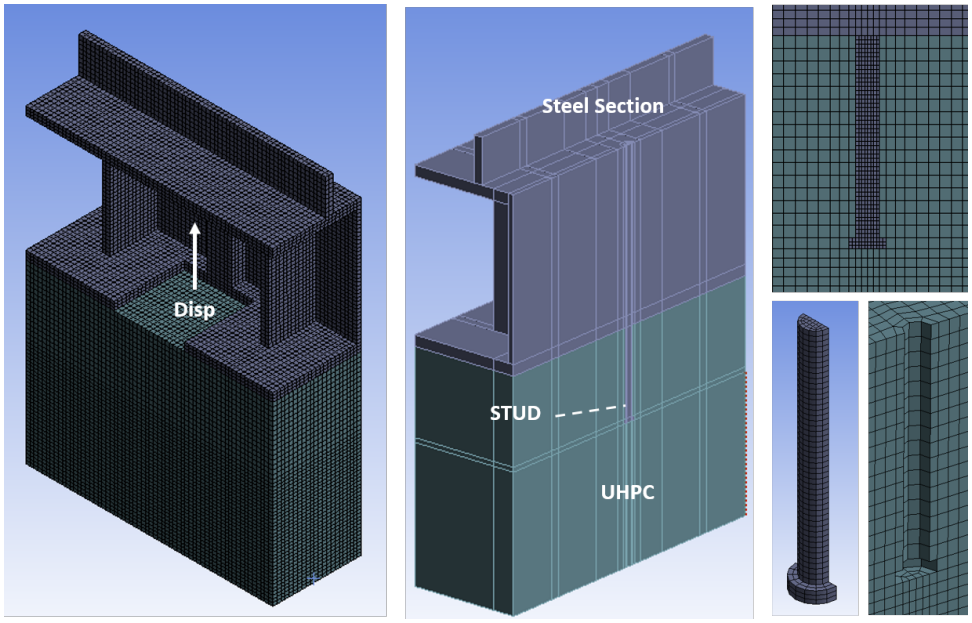

Figure 2.24: Finite element model of stud under tension based on experimental study of Lin et al. [75].

A FE analysis is carried out on behavior of studs under tensile loads. An experimental study carried out by Lin et al. [75] on behavior of studs embedded in UHPC is used for modeling and all material, geometric and testing conditions are derived from the literature. The test specimens consisted of a single steel stud welded to a

steel beam and embedded in concrete. For the FE modeling, two experiments were modeled with overall length of stud $h_s = 200\,mm$ and $h_s = 300\,mm$, respectively. The diameter of shank, diameter of head, and height of stud were kept constant and equal to $22\,mm$, $35\,mm$, and $10\,mm$ respectively. The FE model and meshing conditions are shown in Figure 2.24. The authors used a lubrication between steel beam and concrete to reduce the effect of any bond or adhesion between the two materials. Therefore, frictionless surface was modeled between concrete and steel interface. The steel beam is modeled as linear solid elements and concrete is modeled using CPT215 elements.

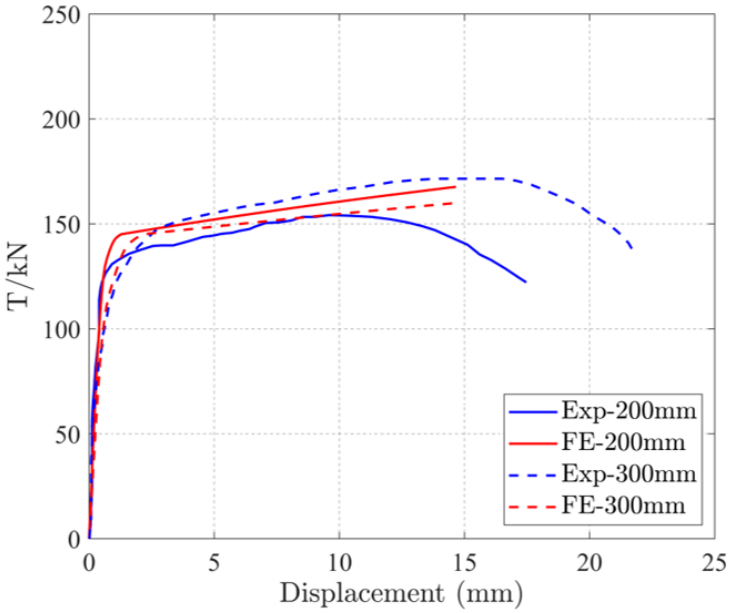

Figure 2.25: Comparison of experimental and numerical load-displacement for studs under tension [75].

Taking advantage of the symmetry conditions, one half of the model was considered for analysis. A symmetry condition is applied to the model on face normal to the cut plane. A friction coefficient of 0.41 was applied between the surfaces of the stud and the adjacent concrete. The relative separation between the steel beam

and block is plotted against load as shown in Figure 2.25. The comparison graph shows a general agreement with experimental results.

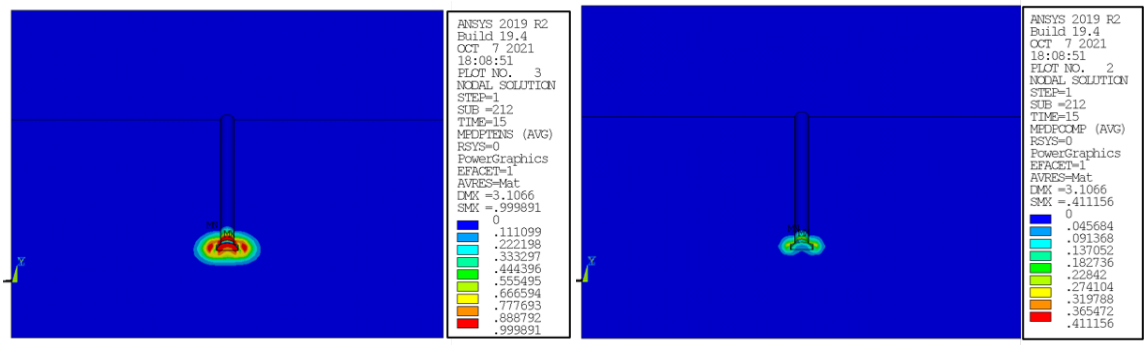

(a) Compression damage (b) Tension damage

Figure 2.26: Compression and tension damages in concrete block at location of $h_s = 300$ mm studs (front view).

The compression and tension damages for $h_s = 200\,mm$ and $h_s = 300\,mm$ is shown in Figure 2.27 and Figure 2.26. The damage contours shows that the extensive damage did not occur in the concrete block. The results of FE show that the shank underwent ductile failure and necking was observed. Since both studs had similar diameter and shank failure mode was observed, the load for both stud lengths were almost equal. An attempt was also made to mode $h_s = 100\,mm$ but due to extensive damages in concrete block, a convergence solution was not obtained. Comparing the damage contours, the area of influence was more prominent for $h_s = 200\,mm$ than $h_s = 300\,mm$.

Using the calibrated model for tension pull-out, the concrete block was replaced with UHPC. A comparison is plotted in Figure 2.28 between corresponding concrete and UHPC block specimens whereas all other conditions are unchanged. The figure shows that the UHPC slightly improves the pull-out load when compared to equivalent NSC model.

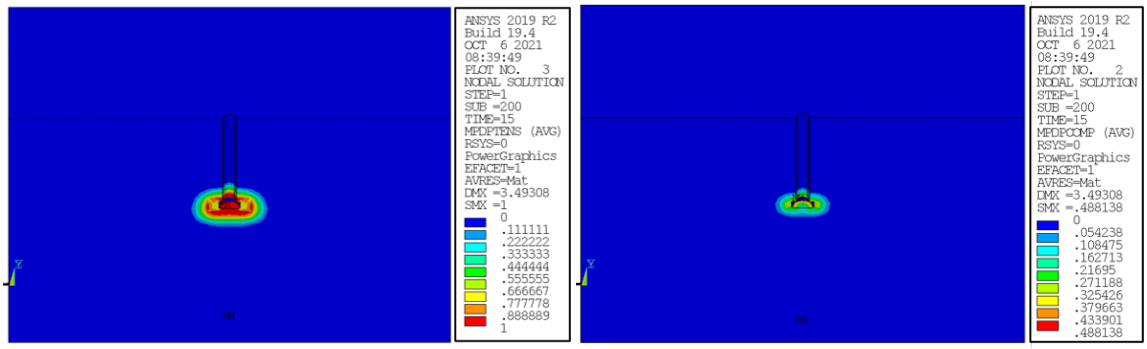

(a) Compression damage (b) Tension damage

Figure 2.27: Compression and tension damages in concrete block at location of $h_s = 200$ mm studs (front view).

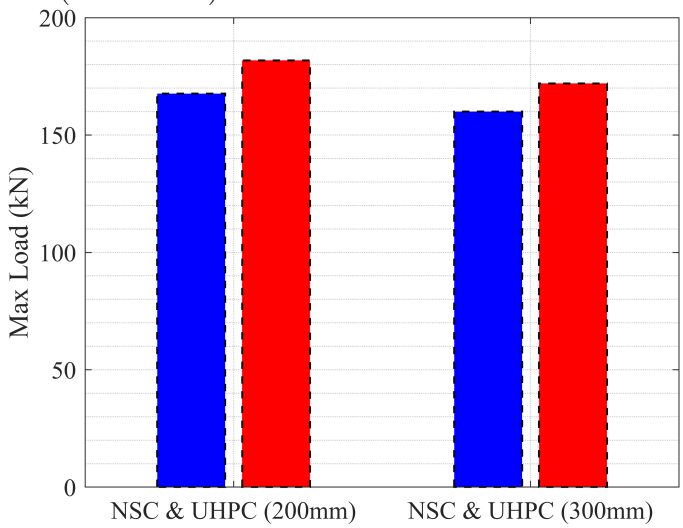

Figure 2.28: Comparison of maximum pull out load for 200, and 300 shear studs for UHPC and NSC.

2.7.4 Effect of Grouped Connectors

Tong et al.[76] carried out experimental study on stud shear connectors in UHPC. The results of grouped connectors were used to understand the behavior of closely spaced connectors in a UHPC pocket under static pushout loading. The study concluded that even though the group effect reduces the shear stiffness per stud, the use of UHPC improves the shear capacity when compared to conventional concrete.

The model consisted of six connectors in a grid pattern (spacing 65 mm x 50 mm). The stud consisted of 19 mm diameter and a length of 80 mm embedded in a

pocket of UHPC. The studs were connected to high strength steel beams. Detailed description of the test is provided in [76]. The steel beam is modeled as linear solid elements and UHPC is modeled using CPT215 elements. Taking advantage of the symmetry conditions, one half of the model was considered for analysis. A symmetry condition is applied to the model on face normal to the cut plane. A friction coefficient of 0.41 was applied between the surfaces of the stud and UHPC. The model is shown in Figure 2.29.

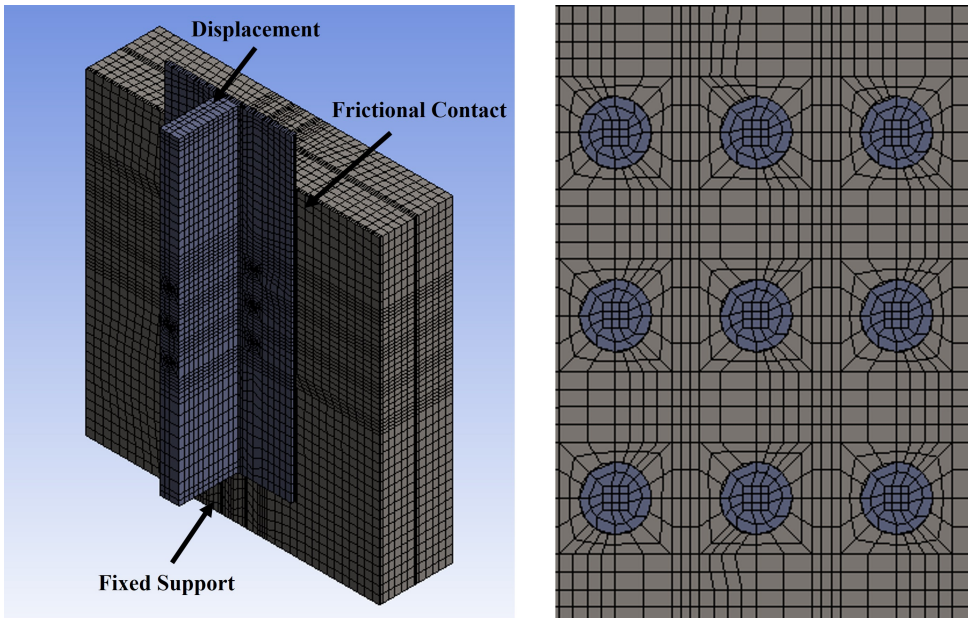

Figure 2.29: FE model of group connectors based on experimental study by Tong et al. [76].

Due to large degree of damages, the model did not converge, and a comparison plot could not be plotted for the entire load vs slip. The tension and compression zones are plotted in Figure 2.30 for initial values of slip. The figure shows that the compression damage zones overlap at the onset of loading, and which can reduce the shear capacity due to higher localized damage in UHPC. This numerical analysis was limited to one model with an aim to understand the behavior of studs in a group. However, further improvement in numerical model and calibration of microplane

model is required to provide conclusions.

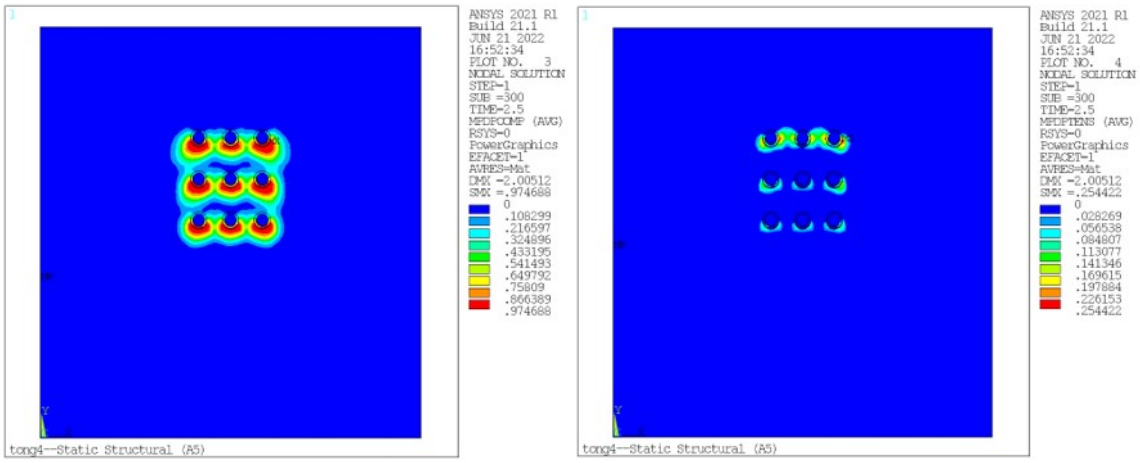

(a) Compression damage (b) Tension damage

Figure 2.30: Compression and tension damage in UHPC block.

2.8 Summary of Pretest Finite Element Analysis

A pretest finite element study was carried out on different aspects of the proposed connection detail. All the pretest FE analyses were calibrated using experiments from past literature. A brief summary of the pretest finite element is presented as follows:

- Microplane model for confined UHPC and NSC was calibrated using experiments from literature.
- Mesh sensitivity and friction coefficient was also performed for NSC confined by steel tube.
- The behavior of the connectors under shear was evaluated by means of a shear test setup from existing literature and a comparative study was performed to understand the behavior of weld collar on the load slip. The results showed

that the weld collar reduced the slip but did not significantly improve the load carrying capacity.

- Behavior of connector under tension loads was also performed to evaluate the effect of shear connector length for both UHPC and NSC. The length of the stud did not significantly improve the load carried in tension. Other parameters such as diameter of stud head, thickness of head was not evaluated.
- Grouped behavior of connector was limited to a single model due to convergence issues. The damage contours for connectors overlapped when connectors are located in close vicinity. Also, the damage contours for first layer of stud (near to the loading plane), undergo maximum deformation and stress.

CHAPTER 3

EXPERIMENTAL STUDY ON CONCRETE FILLED STEEL TUBE CONNECTIONS

Parts of this chapter was published in a technical paper titled "Experimental Study on Concrete Filled Steel Tubes to Footing Connection using Ultra-High Performance Concrete" in Engineering Structures [28].

3.1 Introduction

The synergistic interaction of steel and concrete in concrete filled steel tube (CFT) composite members improves structural performance by delaying local buckling of steel tube. Compared to localized confinement provided by discreet ties in reinforced columns, the steel tube provides continuous confinement to infill concrete which results in improved energy dissipation and ductility performance [77]. However, the ultimate strength of filled and unfilled steel tubes is almost similar due to outward buckling which is not constrained by the infill concrete [78]. Circular CFT provides higher confinement for lower slenderness (L/D) ratios when compared to rectangular and square CFT columns [79].

The strength and ductility of CFT column are proportional to the diameter to thickness (D/t) ratio. The thin-walled steel tubes are erected on site which acts as formwork for concreting and are designed to sustain construction loads. For most applications, CFT does not require additional steel reinforcement cage which reduces the labor cost and improves construction efficiency. In addition, the steel tube has better fire resistance due to infill concrete acting as heat sink and delays temperature rise in steel section when subjected to fire [80]. Owing to these advantages, CFT

has been widely used in infrastructure work, industrial construction and high-rise building columns.

3.2 Experimental Program

Previous research has demonstrated the effectiveness of an embedded and encased connection. Based on similar principles, a new concept for CFT connection was envisioned with an aim to develop the full flexural capacity of the CFT which can undergo large displacement ductility. Different details were envisioned for the connection of CFT-to-precast concrete element. Based on the envisioned connection details, an experimental program was established. The new connection consists of CFT embedded in the precast member and encased within a layer of UHPC. Three connection details were tested: i) a partially embedded connection ii) an encased connection and, iii) a fully embedded connection. The specimens were designed to be tested under incremental lateral cyclic and constant axial load. This section presents the design, construction, and details of the specimen.

The embedment depth filled with UHPC inside the precast element provides structural strength and an encasement outside the concrete ensures that the damage is located outside the footing which is typically designed as a capacity protected element. Additional dowels in the UHPC layer are designed to accommodate the force transfer in the connection.

Different details are envisioned for the connection of CFT-to-footing. Among the possible options, three main parameters are investigated. This includes a) the location of UHPC layer, b) the type of transfer mechanism (shear connectors), and c) depth of embedment.

The development of dowels and the width of the UHPC layer is dependent on the minimum embedment depth of the reinforcing dowels and the cover requirements. Figure 3.1 shows the schematic and geometric variables of the specimen. The embedment depth is comprised of two components, d_e (depth of embedment in footing) and d_s (depth of encasement), which are encased in a layer of UHPC, d_t (UHPC depth) which is sum of both d_e and d_s. The width (D) of the UHPC layer depends on the outside diameter (d) of the CFT and additional width required to encase dowels within cover requirements of UHPC. The geometrical variables of the precast footing including length (L) and thickness (T), also shown in Figure 3.1, are determined based on the moment curvature analysis.

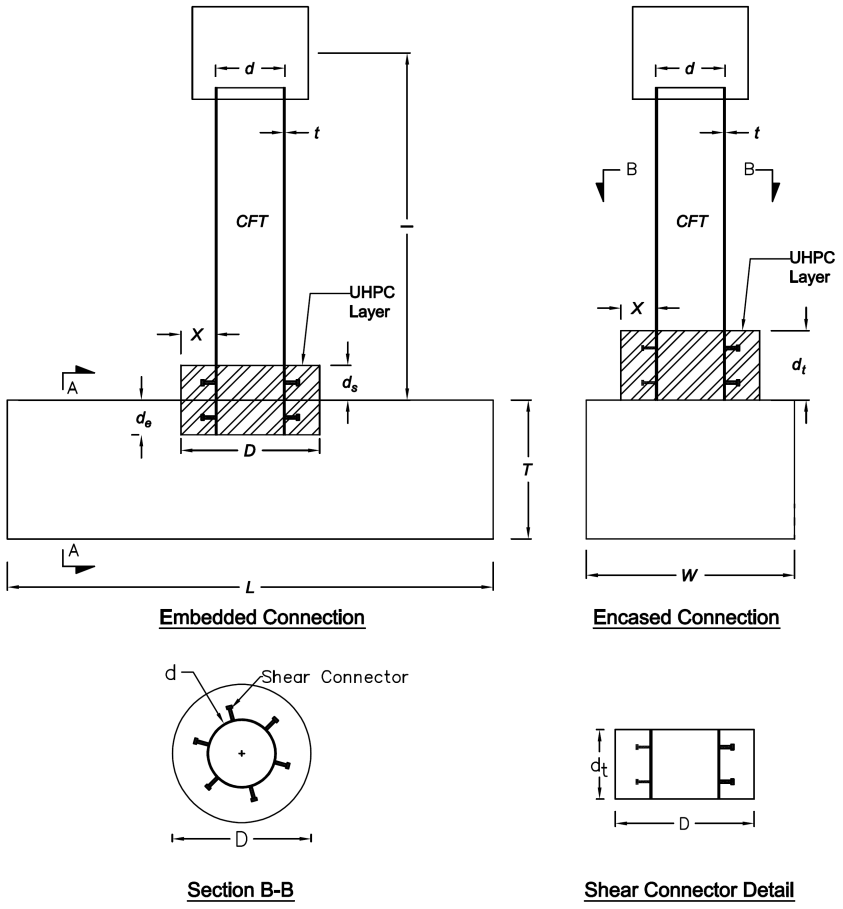

Figure 3.1: Different design parameters for the proposed connection detail.

Based on the envisioned connection details, an experimental program was established at Florida International University (FIU). Three connection details were tested i) a partially embedded connection (Specimen-1), ii) a fully encased connection (Specimen-2) and, iii) a fully embedded connection (Specimen-3). The details of test specimens are provided in Table 3.1.

Table 3.1: Test parameters for proposed connection detail.

Parameters	**Specimen-1**	**Specimen-2**	**Specimen-3**
Diameter to thickness ratio (d/t)	51	51	51
Length to dia ratio (l/d)	4.94	4.58	4.65
Embedded Depth	$0.5d_i$	-	$0.75d_i$
Encased Depth	$0.5d_i$	$0.85d_i$	-
UHPC Layer Width (D)	24 in.	24 in.	24 in.

The material and geometric properties of different sections were used to calculate the capacity of the section for the test specimen. The CFT column consisted of a spiral weld tube which conforms to ASTM A252 standards. The compressive strength of NSC and UHPC were assumed to be 6.5 ksi and 24 ksi, respectively. For the test specimen, the outer diameter of the CFT column was 12.75-in with a wall thickness of 0.25-in. The shear connectors consisted of 0.75-in diameter deformed reinforcing steel which conforms to the ASTM A615 specification. The shear connectors used in the specimen-1 and 2 had a shaft diameter of 0.5-in, and an aspect ratio of 5. The shear connectors in specimen-3 consisted of shank diameter of 0.5-in, but an aspect ratio of 4.

3.3 Design of Test Specimen

Specimen-1 was designed as an embedded connection which consisted of a total of 18 shear connectors that were welded to the tube made of low carbon steel conforming

to ASTM A29. The cover thickness (horizontal direction) over the head of the shear connector was 2.75-in which conforms to the AASHTO-LRFD specification [81]. The diameter-to-depth (d/t) ratio of the CFT column was 51 which is less than 87 based on AISC specifications [82]. This limit ensures the local stability of the tube. The UHPC layer depth (d_e+d_s) was taken as 1.0 x internal diameter of the column (d_i). The recess in the specimen was octagonally shaped with a maximum dimension of 24-in. This recess was corrugated to provide a composite action with the adjacent NSC.

The design of the shear studs should be based on the load transfer between the tube and UHPC. It is assumed that for composite behavior the total strength of shear connectors should be capable of developing yielding of the CFT section. Assuming material properties, the total number of 0.5-in. studs required for the load transfer from the tube to UHPC can be estimated based on Article 6.10.10.4.1 of AASHTO LRFD. Although this equation is used for interface between concrete deck and steel section to resist interface shear but can be conservatively used to calculate the number of shear connectors as follows:

$$Q_n = 0.5 A_{sc} \sqrt{f'_c E_c} < A_{sc} F_u = 11.98 Kips \tag{3.1}$$

The modulus of elasticity (in psi units) of UHPC was calculated based on Graybeal [52] as follows:

$$E_c = 49,000 \sqrt{f'_c} \tag{3.2}$$

$$n = \frac{A_t F_{ut}}{Q_n} \approx 69 \tag{3.3}$$

It is assumed that the stud will have the capacity to transfer the forces when the tube is at its ultimate capacity. Considering the 12.75-in. diameter of the specimen and 1.0 x d_i embedment length in UHPC, placing 69 studs would not be feasible.

Kruszewski et al. [83] concluded that bigger weld area can increase the push-off capacity of a stud. Therefore, in this study a 1/6 in. fillet weld was used to connect the studs to the tube. As mentioned before, the spiral weld of the CFT is sufficient for providing the composite action. Adding a weld on the outside regardless of the shear stud would help with force transfer similar to the ribs on deformed bars. The bigger weld on the studs would increase the area at the base of the stud four times. This can reduce the number of studs required to 18. Finally, a total of 18 studs were welded to the steel tubes.

Based on Caltrans provisions, the connection was designed to resist the maximum over-strength moment which is defined as 1.25 times the plastic moment capacity of the column. For specimen-1 design, the capacity was evaluated at different sections such as CFT section (A-A), UHPC layer section (B-B), and footing section (C-C). Moment-curvature analyses were conducted for sections at these locations using fiber approach, and the moment capacities of the sections are provided in Table 3.2. Based on over-strength requirements, the concrete section was proportioned, and the reinforcement was determined as shown in Figure 3.2.

Table 3.2: Moment capacity of sections for specimen-1.

No.	**Moment (M1)**	**Moment (M2)**	**Moment (M3)**	**Moment (M3/M2)**	**Moment (M1/M2)**
Specimen-1	318	228	353	1.5	1.4

Specimen-2 was designed as an encased type connection which also consisted of a total of 18 shear connectors to transfer forces at the connection. The embedment length (d_s) was taken as 0.85 x d_i. No recess was provided in this type of connection which translates into simpler reinforcement details for the footing. The width of encasement layer in the specimen was 24-in diameter to provide sufficient cover for reinforcing dowels and shear connectors. Similar to specimen-1, the ca-

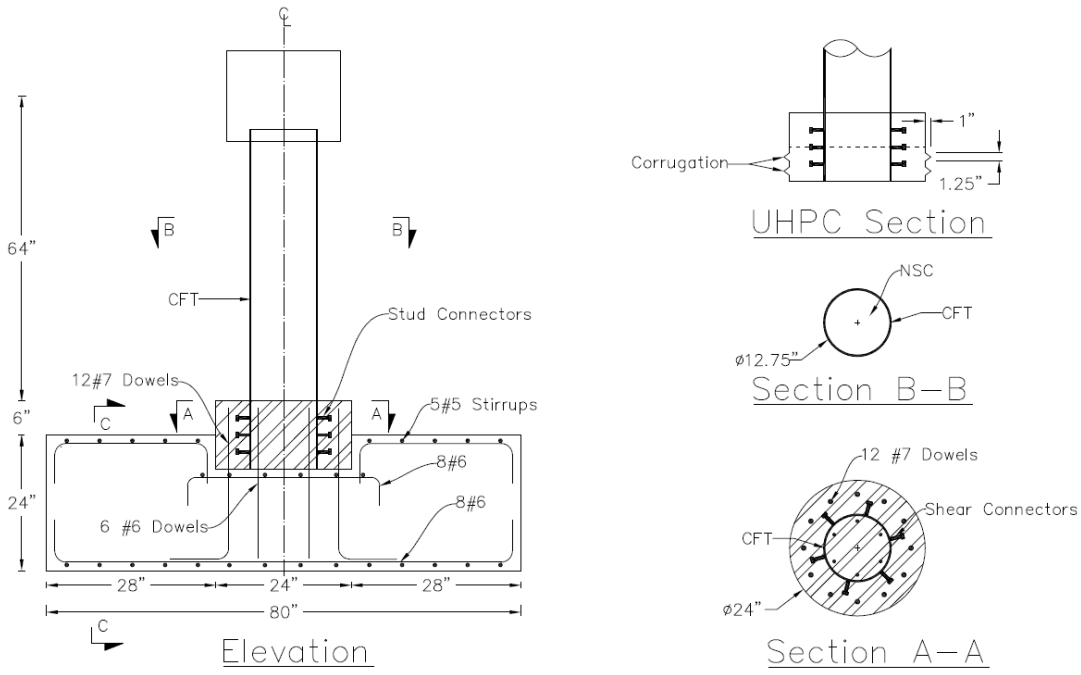

Figure 3.2: Schematic detail of specimen-1 showing dimensions and reinforcement details.

pacities of sections were evaluated at different sections such as CFT section (A-A), UHPC layer section (B-B), and footing section (C-C). Moment-curvature analyses were conducted for sections at these locations using fiber approach, and the moment capacities of the sections were provided in Table 3.3. Based on over-strength requirements, the concrete section was proportioned, and the reinforcement was determined as shown in Figure 3.3.

Table 3.3: Moment capacity of sections for specimen-2.

No.	**Moment (M1)**	**Moment (M1)**	**Moment (M1)**	**Moment (M1/M2)**	**Moment (M1/M3)**
Specimen-2	302	228	468	2.1	1.3

In some applications of proposed detail, provision of encasement (full or partial) may not be possible. Besides construction difficulties, the encasement may be undesirable from aesthetics point-of-view. Therefore, specimen-3 was designed as a fully embedded connection. The connection also consisted of 18 shear connectors to

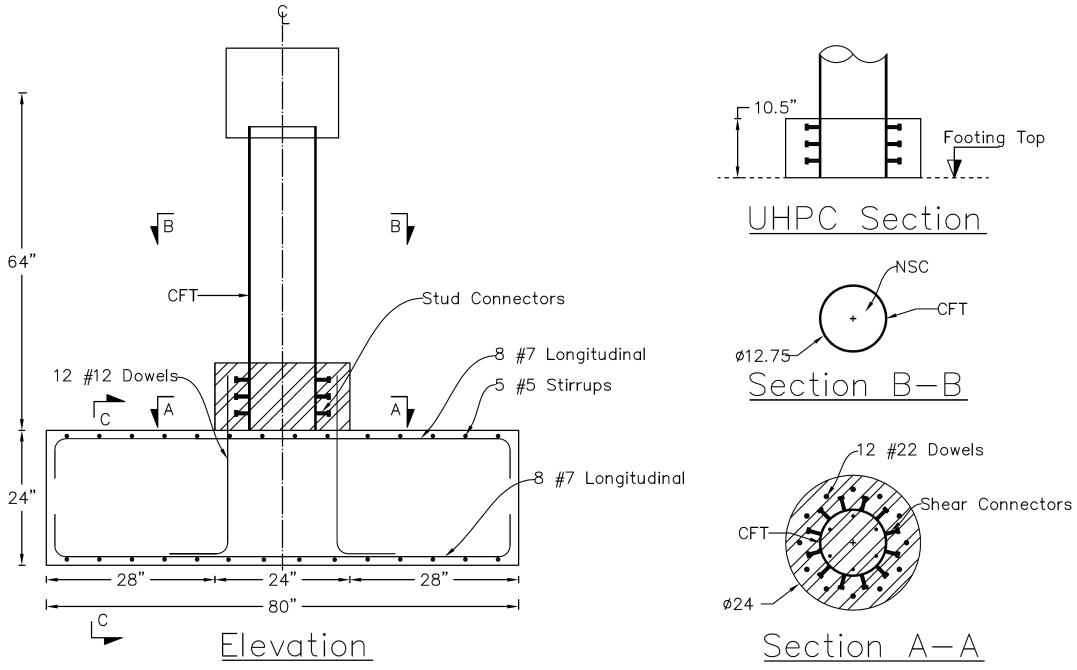

Figure 3.3: Schematic detail of specimen-2 showing dimensions and reinforcement details.

transfer forces at the connection. However, based on the results of the specimen-2, it was decided to provide shear connectors with sufficient cover to the edge of adjacent concrete. In order to accommodate 18 connectors within the bottom of the tube while maintaining a minimum center-to-center distance between the connectors, a staggered arrangement was used.

Since the UHPC was completely confined by concrete member for specimen-3, a lower embedment length (d_s) of 0.75 x d_i was used. In order to keep the d/t ratio similar to other two specimens, the footing depth was increased. This required a deeper recess into the footing. The width of encasement layer in the specimen was 24-in diameter to provide sufficient cover for reinforcing dowels and shear connectors. The capacities were evaluated at different sections such as CFT section (A-A), UHPC layer section (B-B), and footing section (C-C) which are provided in Table 3.4. Based on over-strength requirements, the concrete section was propor-

tioned, and the reinforcement was determined as shown in Figure 3.4. As can be seen, a thin layer of UHPC was also cast on top of the precast element in addition to the layer required for complete embedment.

Table 3.4: Moment capacity of sections for specimen-3.

No.	**Moment (M1)**	**Moment (M1)**	**Moment (M1)**	**Moment (M1/M2)**	**Moment (M1/M3)**
Specimen-3	302	228	468	2.1	1.3

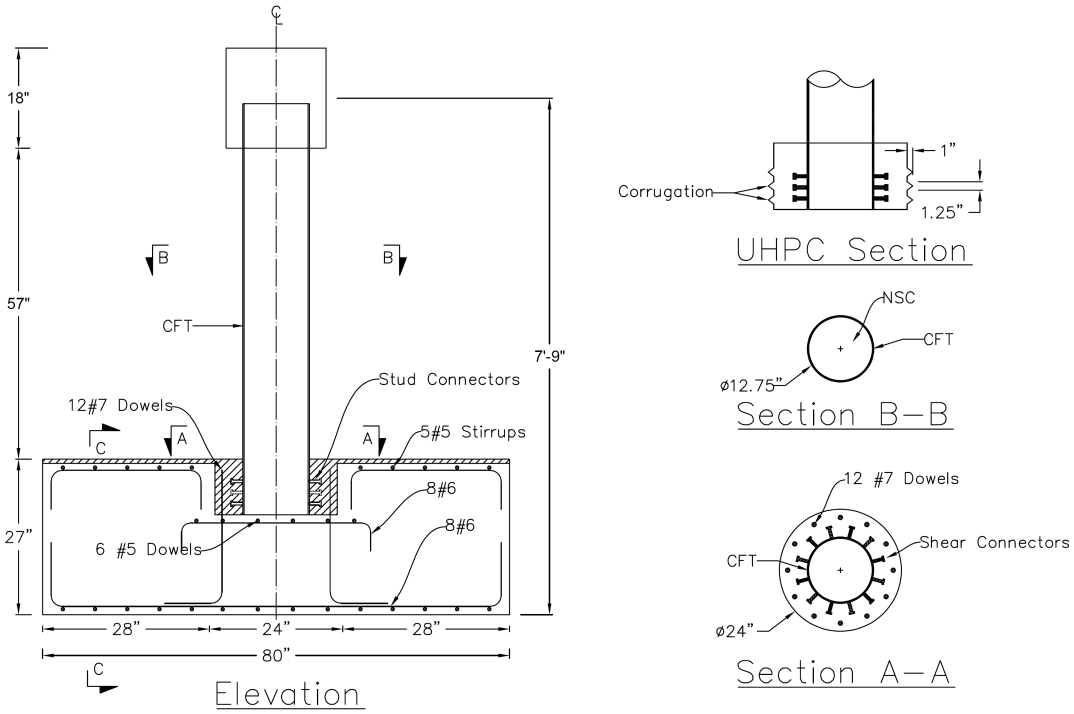

Figure 3.4: Schematic detail of specimen-3 showing dimensions and reinforcement details.

3.4 Construction Details

A propriety UHPC (Ductal ®) was used for all elements with similar mix composition which is provided in Table 3.5 [52]. Premix bags were first placed in the batch mixer until and then water and superplasticizer were added. After about 15 minutes

Table 3.5: Constituents of Ductal UHPC.

Parameters	**UHPC lb/ft^3**	**Percentage by weight**
Portland cement	44.4	28.5
Fine aggregates	63.7	40.8
Ground quartz	13.1	8.4
Silica fume	14.4	9.3
Accelerator	1.9	1.2
HRWR	1.9	1.2
Water	6.8	4.4
Steel fibers (2%)	9.7	6.2

of mixing, the matrix transformed into a wet paste. The fibers were slowly added to the mix for few minutes until the fluid paste achieved a uniform texture and fiber distribution. Depending on the size of the specimen, the UHPC volume was calculated to minimize the number of batches. During each batch, cylinders were cast for material testing. A local supplier provided the ready-mix concrete with a slump of 4 inches. The compacting procedure for NSC specimens was performed according to ASTM specification (ASTM C 31-69). Concrete cylinders were also taken during casting.

3.4.1 Partially Embedded Connection

Figure 3.5 shows the sequence of construction for specimen-1. The footing reinforcing bars with dowels were placed before casting of normal concrete. In the first stage, a prefabricated footing was cast with a recess. The recess was fabricated into the footing using a styrofoam mold. The profile of the styrofoam was corrugated at its circumference to allow transfer of forces between UHPC and adjacent concrete footing. Before casting, the mold was embedded in the footing and NSC was cast. After curing, the styrofoam mold was removed and the interface at the bottom surface of the recess was chipped off to improve bond between the footing concrete and the UHPC. To allow UHPC to flow inside the CFT, two grooves were cut at the

bottom of the CFT. In the encasement region, a total of 18 shear connectors were welded (using arc welding method) equidistant around the tube. An encasement formwork was placed with a 24-in Sonotube and the CFT tube was placed inside the recess. Then the UHPC was cast into the recess for a total depth of 12-in with 6-in encasement above the footing. The UHPC connection was covered with burlap and allowed to cure for 7-days before concrete in-fill for CFT was cast. A concrete loading block was constructed at the top to apply incremental lateral cyclic and constant axial load. Further details of construction procedure are documented in Figure A.1.

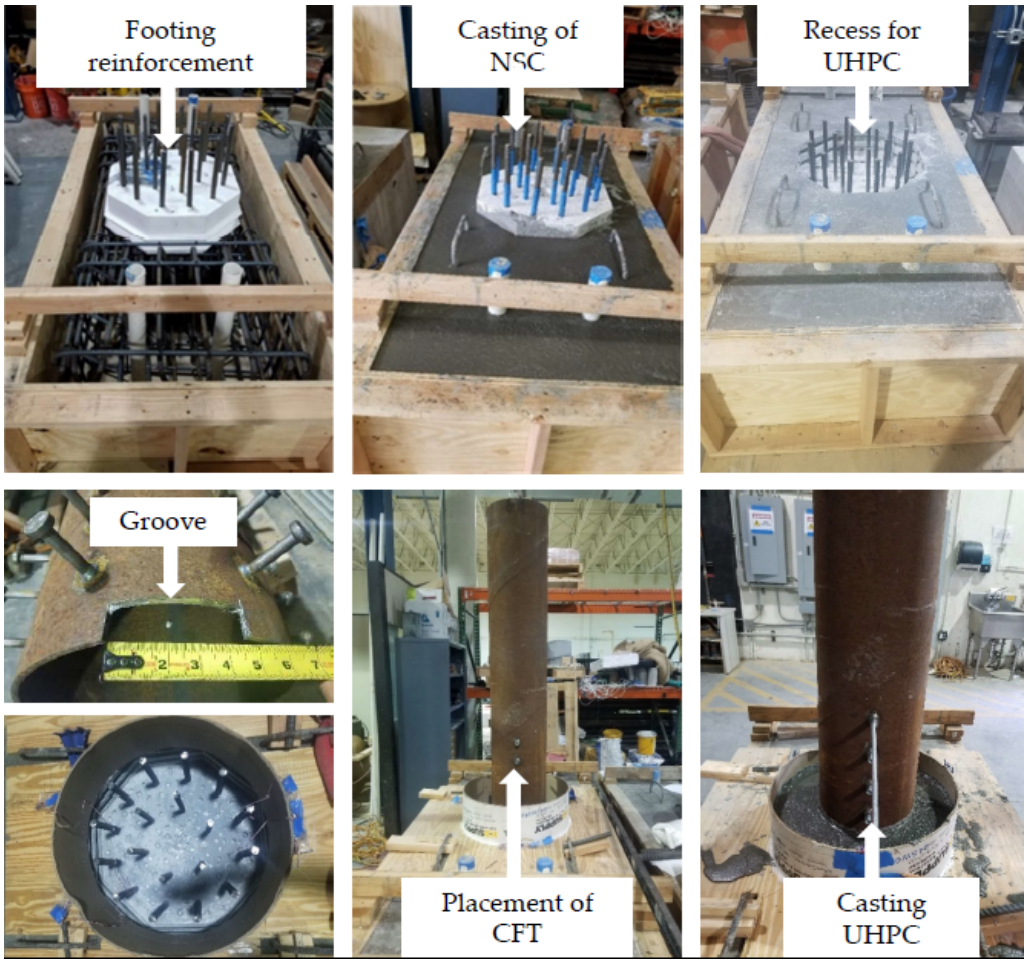

Figure 3.5: Construction of partially embedded connection (specimen-1).

3.4.2 Encased Connection

The construction of encased connection (specimen-2) was similar to specimen-1. Since the connection is designed as encased, the UHPC is completely located outside the precast concrete element. Figure 3.6 shows pictures of the construction sequence for specimen-2. After casting of normal concrete of footing, the interface between UHPC encasement and the footing was roughened to about half-inch depth. The dowel bars and the steel tube were instrumented with strain gauges prior to the casting of UHPC. The encasement layer was cast using a sonotube of 24-inch diameter and a depth of 10.5 inches ($0.85d_i$). Similar to specimen-1, two grooves were cut at the bottom of the CFT to allow UHPC to flow inside the tube. After casting of UHPC encasement, the steel tube was filled with normal concrete. A concrete cap was also cast at the same time which is reacted against the hydraulic ram. Further details of construction procedure are documented in Figure A.3.

Figure 3.6: Construction of encased connection (specimen-2).

3.4.3 Fully Embedded Connection

The embedded connection was constructed using similar approach for partially encased connection. Since the fully embedded connection required a deeper recess, a styrofoam was placed inside the footing which was flushed with the top of the footing. The dowels were embedded inside the foam. Similar to specimen-1, the styrofoam was corrugated at the edges to provide a shear transfer mechanism with adjoining concrete element. At this stage, the dowels and footing reinforcement was instrumented with strain gages. In the next stage, the footing was cast using the conventional construction procedure. After curing for a period of seven days, the styrofoam was removed as shown in Figure 3.7.

Figure 3.7: Construction of fully embedded connection (specimen-3).

The styrofoam was designed to furnish grooved finished for a depth of 9.5 inches which is equivalent to $0.75d_i$. The grooved finish was only made on the sides while the top of the recess was chipped off to a depth of 0.5 inches using manual drill. Before casting of the NSC, the exposed concrete surfaces were covered with wet burlap for a duration of 24 hours. Then the tube was placed inside the recess and UHPC casting was carried out. It should be pointed out that besides the recess the casting of UHPC was continued to the entire area of the footing for a depth of

0.5 to 0.75 inches. Additional strain gages were placed on the tube and the shear connector in the loading direction. The specimen was completed by fabricating a formwork for the loading cap and NSC was cast for the remaining length of tube and the cap. The specimen was tested after 28-days of casting of in-fill concrete.

The casting of footing concrete, UHPC layer and infill concrete was carried out at different stages. During each batch, cylinders were cast for material testing. Concrete cylinders were taken during casting and compacting procedure for NSC specimens was performed according to ASTM specification (ASTM C31-69). The material strengths are provided in Table 3.6.

Table 3.6: Material properties of UHPC and NSC.

Materials	**Specimen-1**	**Specimen-2**	**Specimen-3**
Footing Concrete f'_c	6.3	6.4	5.9
UHPC f'_{uhpc}	24.0	23.0	21.2
In-fill Concrete f'_c	6.3	6.4	4.9

3.5 Test Setup and Loading Protocol

The specimens were designed to be tested in a cantilever configuration with concrete component anchored to the strong floor. The cyclic load was applied on loading block using a 150-kips servo-hydraulic actuator. The cyclic load was based on displacement-control loading scheme which was applied as incremental drift ratios. The test setup and some of the instrumentation are shown in Figure 3.8.

Prior to testing, the specimens were instrumented extensively with string potentiometers, steel strain gauges, linear potentiometers, and load cells which are tabulated in Table 3.7. The dowels were typically instrumented with strain gauges at critical locations. Similarly, strain gauges were also installed on the outer surface of the CFT tube at different depths. Coupling nuts were also welded on the steel

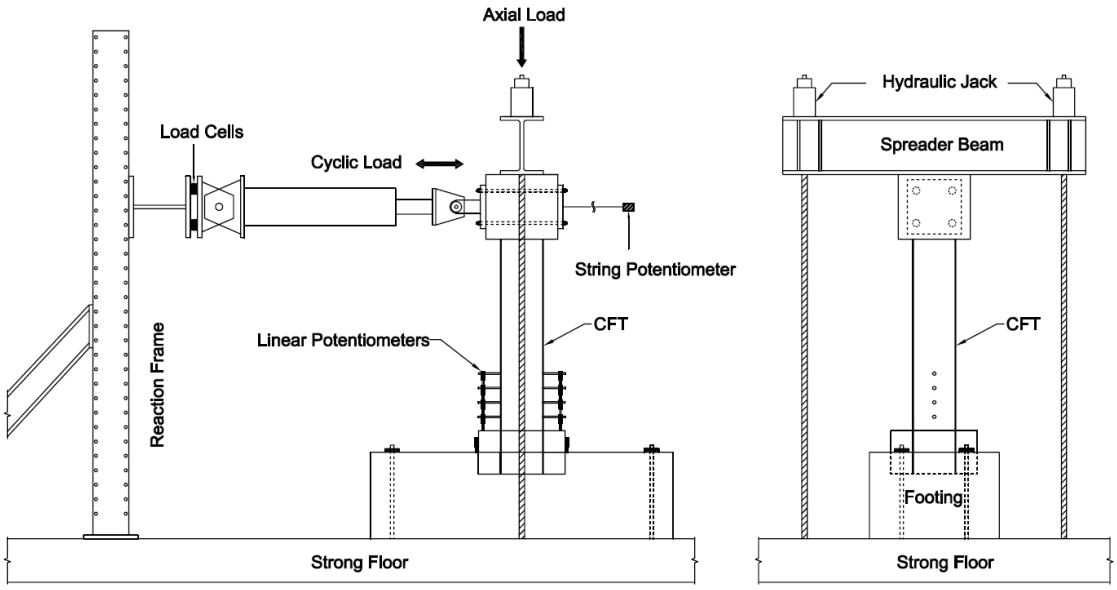

Figure 3.8: Schematic of load setup.

tube to allow for the installation of linear potentiometers. Video cameras were used to record the damage progression of the specimens throughout the test.

Table 3.7: Instrumentation summary for all specimens.

Instrumentation	**Specimen-1**	**Specimen-2**	**Specimen-3**
Load Cells	10	10	10
Steel dowel strain gauges	3	12	10
Steel tube strain gauges	13	26	15
String Potentiometers	1	1	6
Pressure Transducers	3	3	3
Linear Potentiometers	10	10	-
RC component steel gauges	2	3	2

The response of the test specimen during the test was typically monitored to evaluate the connection under a combination of cyclic and axial loading. Displacement-controlled cyclic loads with increments of first yield displacement, Δy, were applied to the CFT until failure as shown in Figure 3.9. The first yield displacement of the column can be estimated during the first cycles from idealized bi-linear models. After estimating the first yield displacement, displacement was applied in pull and push direction as a multiplier of yield displacement. Due to slight difference in pull

and push direction, adjustment was made to calibrate the displacement for zero load. Each cycle was repeated three times and the test was continued until failure was observed. Observations for damages and failure mode were typically performed at different displacement levels. The photographs of the test setup for both specimen are shown in Figure 3.10.

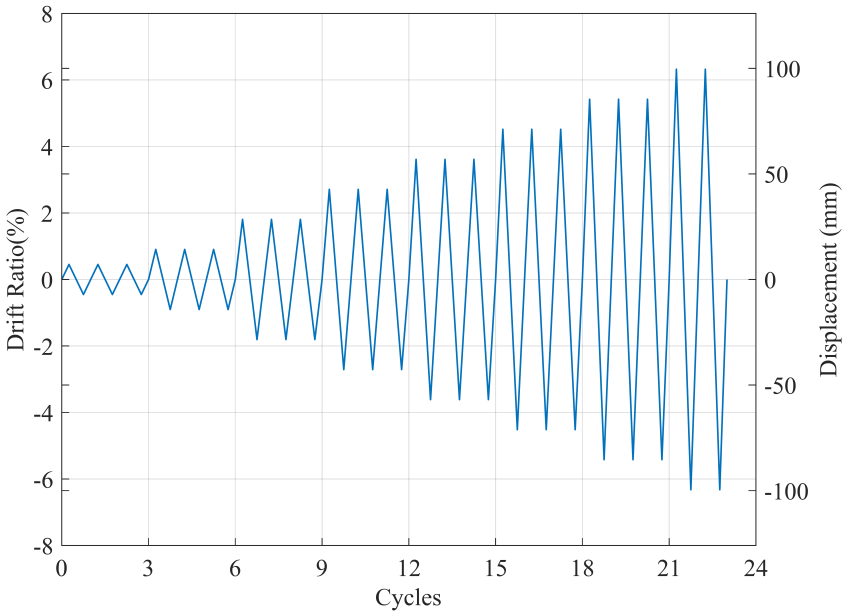

Figure 3.9: Loading protocol for cyclic testing.

3.6 Experimental Results

The proposed connection details are tested under constant axial and flexural loading. The proposed connection detail consists of anchor dowels and shear connectors welded to the steel tube in the connection region for force transfer. This section presents the failure modes, load displacement and strain response at critical sections.

Figure 3.10: Pictorial view of the test setup.

3.6.1 Failure Mode for Partially Embedded Connection

The response of the specimen-1 during the test was monitored to evaluate the connection under a combination of cyclic and axial loadings. Displacement-control cyclic loads with increments of first yield displacement, Δy, were applied to the CFT until failure. The response of the specimen-1 during the testing is shown in Figure 3.11. During the initial cycles, hairline cracks were observed in the UHPC encasement. This cracking is attributed to a construction shortcoming from a void which was left during casting of UHPC. These cracks were limited to initial cycles and neither propagated nor widened until the end of testing.

The physical bulging in the steel tube was visually observed at $2\Delta y$ and progressed with increase in displacement levels. Finally, the steel tube failed through ductile tearing during the second cycle of $7\Delta y$ and the test was halted. The buckling and rupture of the steel tube, shown in Figure 3.11d, before observing damage in the footing and connection is the desired behavior. The system showed a composite

Table 3.8: Damage in specimen-1 at different displacement levels.

Disp	**Specimen-1**
1 Δy	No damage observed
2 Δy	Minor cracks in UHPC encasement
3 Δy	Bulging of the steel tube visible in 3rd cycle – Few additional cracks in UHPC encasement
4 Δy	Increase in bulging of the steel tube
5 Δy	No key damages observed
6 Δy	Substantial bulging of the steel tube
7 Δy	Tube fracture – Termination of testing

behavior at the encasement location and minimal separation between the tube and the surrounding UHPC. The connection was able to fully transfer the loads from the column to the footing while the capacity protected (footing) element remained elastic. Some of the major observations during each Δy are provided in Table 3.8.

(a) Buckling of tube at $2\Delta y$

(b) Buckling of tube at $3\Delta y$

(c) Buckling of tube at $5\Delta y$

(d) Tearing of tube at $7\Delta y$

Figure 3.11: Damage progression in partially embedded connection (specimen-1).

3.6.2 Failure Mode for Encased Connection

Compared to the first specimen, the design of the second specimen was modified. In the second specimen, the inner dowel bars were removed, and the embedment length inside UHPC was reduced slightly to about 10.5 in (0.85 d_i). Displacement-control cyclic loads with increments of first yield displacement, Δy, were applied to the specimen until failure. During the testing, observations were made for damages in footing and UHPC at the end of each increment in displacement level.

The response of the specimen-2 during the testing is shown in Figure 3.12. At the initial displacement level, cracks were observed in the UHPC encasement. These cracks increased with an increase in displacement levels and can be seen in Figure 3.12a. The second specimen although reached same levels of ductility, did not show any sign of buckling in the steel tube. This means most of the damage was occurring inside the UHPC encasement. As shown in Figure 3.12c, the top layer of shear connectors pushed out of UHPC. This failure of first layer of shear connectors resulted into reduction of load carrying capacity. This failure of the first layer of shear connectors did not result in a substantial decrease in the lateral load-carrying capacity. However, the specimen was able to sustain further load as the other two layers of shear connectors were engaged. The concrete footing did not sustain any damage during the testing. The testing was continued up to $7\Delta y$ with progressive increase of cracking in the UHPC section and the test was halted. Some of the major observations during each Δy are provided in Table 3.9.

3.6.3 Failure Mode for Fully Embedded Connection

The response of specimen-3 (fully embedded connection) was monitored to evaluate the connection under a combination of cyclic and axial loading. Initially, the spec-

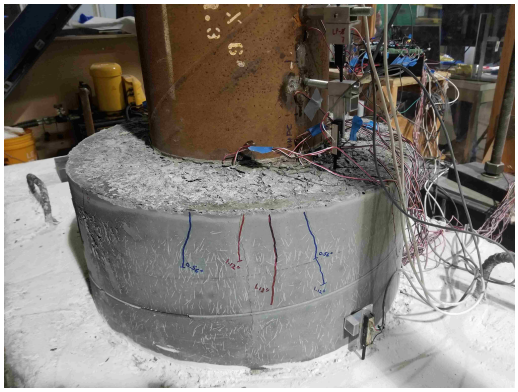

(a) Cracks in UHPC encasement

(b) Protruding of UHPC at $2\Delta y$

(c) Damage of UHPC at $4\Delta y$

(d) Shear stud pull out

Figure 3.12: Damage progression in specimen-2.

Table 3.9: Damage in specimen-2 at different displacement levels.

Disp	**Specimen-2**
1 Δy	Crack initiation in UHPC encasement
2 Δy	Crack propagation and pushout of studs initiated
3 Δy	Breakout cone of studs developed – Drop in lateral load
4 Δy	Damage in UHPC encasement around periphery of the tube – Debonding between tube and UHPC
5 Δy	No key damages observed
7 Δy	Termination of testing

imen was tested under low load levels to ensure the instrumentation was working. Thereafter, axial load was applied to $0.1P_o$. Displacement-control cyclic loads with increments of first yield displacement, Δy, were applied to the CFT until failure. During the entire course of testing, no cracks were observed in the vicinity of the

tube in the UHPC layer nor the footing concrete. No separation between the tube and the UHPC layer was observed until $6\Delta y$. During the second cycle of $7\Delta y$, approximately 1/16 in. separation was observed at the interface. Also, no debonding between the concrete and top layer of UHPC was observed.

The initiation of buckling was observed during the $3\Delta y$ which was progressed with increasing displacement. Due to the axial load setup used for the testing, the specimen's axial load varied at extreme displacement levels due to additional tension in the rods. Between $4\Delta y$ to $6\Delta y$, no significant observations were made except the incremental increase in the buckling. The buckling caused axial shortening of the column, and therefore additional axial load was applied to the specimen after end of each Δy to retain initial $0.1P_o$. The fully embedded specimen failed due to buckling of the tube and ultimate fracture during second cycle of $8\Delta y$. The damage occurred on both push and pull side and testing was halted at this stage. The response of the specimen-3 during the testing is shown in Figure 3.13. Some of the major observations during each Δy are provided in Table 3.10.

Table 3.10: Damage in specimen-3 at different displacement levels.

Disp	**Specimen-3**
1 Δy	No key damages observed
2 Δy	Initiation of bulging observed at push side
3 Δy	Gradual increase in bulging observed
4 Δy	Debonding between tube and UHPC
5-7 Δy	No key damages observed
8 Δy	Fracture of the tube and termination of test

3.6.4 Load Deformation Response

The load-drift hysteresis curves for the three test specimen is presented in Figure 3.14 to Figure 3.16. The drift ratio is obtained by dividing the lateral displacement to the length of column taken from top of UHPC layer to the middle of the loading

(a) Displacement level at $2\Delta y$

(b) Displacement level at $4\Delta y$

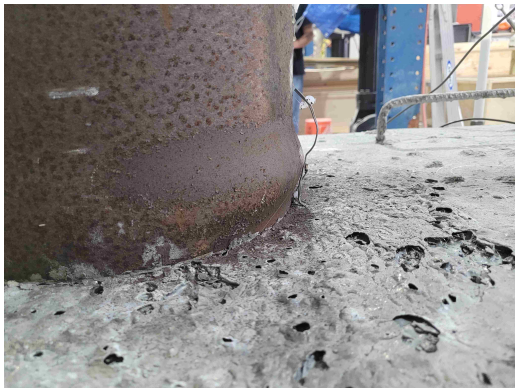

(c) Displacement level at $5\Delta y$

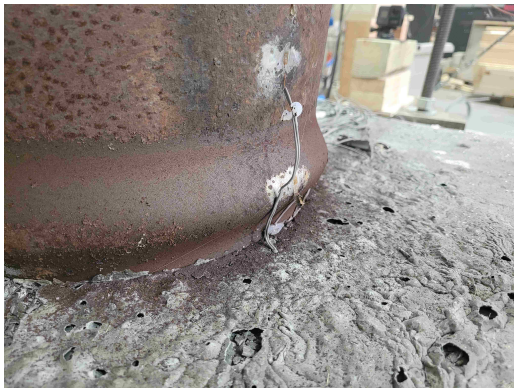

(d) Displacement level at $6\Delta_y$

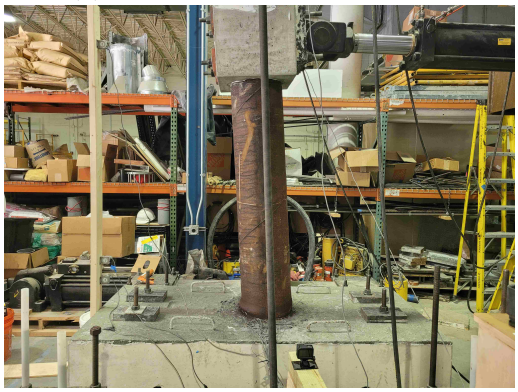

(e) Displacement level at $8\delta_y$

(f) Fracture in steel tube

Figure 3.13: Damage progression in specimen-3.

cap. For specimen-1, the force displacement hysteresis curve showed a symmetrical response with sufficient ductility and energy dissipation. The column was able to reach a drift ratio of about 6.3. For specimen-2, the area of hysteresis loop was reduced significantly when compared to specimen-1. The load deformation response

of specimen-3 was similar to specimen-1 except that due to slightly higher l/d ratio, the specimen failed at lower load. The completely embedded connection also showed a symmetric hysteresis with sufficient energy dissipation at each drift level.

As can be seen from the load-drift curve shows the poor behavior of the second specimen. There is also a pinching behavior observed in the second specimen's graph. This behavior is believed to be due to the cracking in the UHPC encasement and push out of the first layer of studs. During each north-south loading of the specimen, the vertical cracks in UHPC on the south side and the protruded studs and UHPC gap on the north sides were opening. On the return loading these cracks and gaps were closing and the opposite side were opening, and this resulted in the pinching behavior of the column and small hysteresis area of the graph. In the second specimen, the steel tube did not fail until $7\Delta y$ displacement level, and the testing was stopped due to the observed damage in the UHPC encasement.

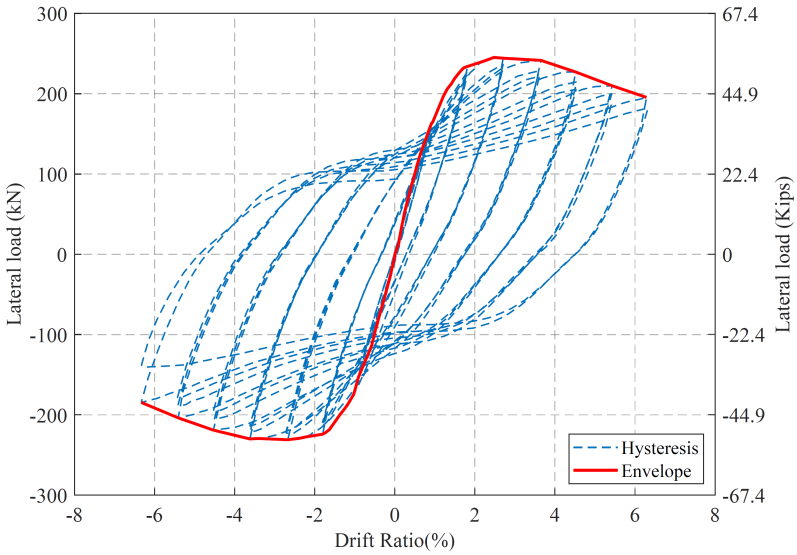

Figure 3.14: Load vs drift ratio plot for specimen-1.

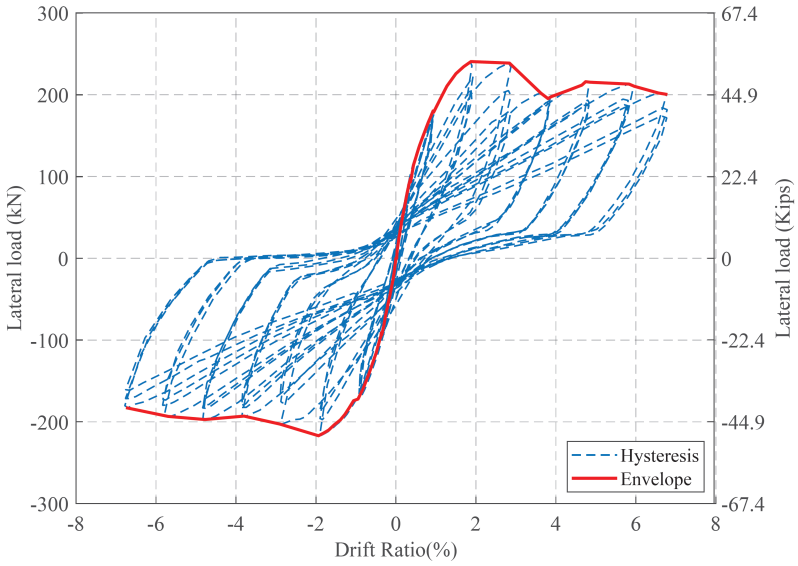

Figure 3.15: Load vs drift ratio plot for specimen-2.

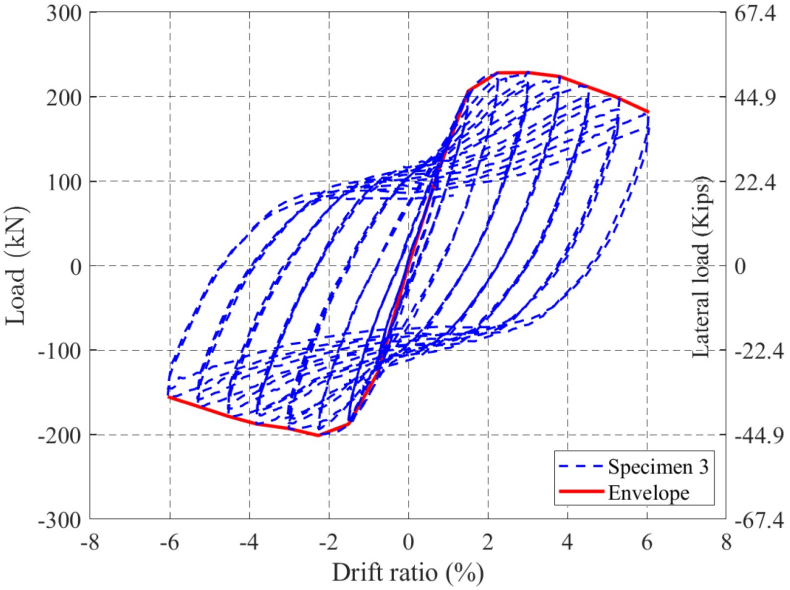

Figure 3.16: Load vs drift ratio plot for specimen-3.

3.6.5 Curvatures

Curvatures were also measured at the encasement level and results are plotted in Figure 3.17. Average curvatures are reported at these heights since buckling of the tube caused inconsistencies in measurement system. The details on the location of

linear potentiometers is provided in appendix Figure A.5. The curvatures on the column were monitored as an indicator of the plasticity near the connection. For specimen-1 the measured curvature near the UHPC encasement was averaged and plotted as a single point due to the excessive buckling of the steel tube. This point (distance from top of encasement of 3.5 in.) shows the curvature for the bottom 7 in. of the column. The plotted curvature at 5 in. was calculated from the linear transducers attached to near the interface of the UHPC and footing, which indicate that the interface did not experience any opening or rotation. The data at higher drift ratios are not reported since some of the linear potentiometers were disengaged at these levels.

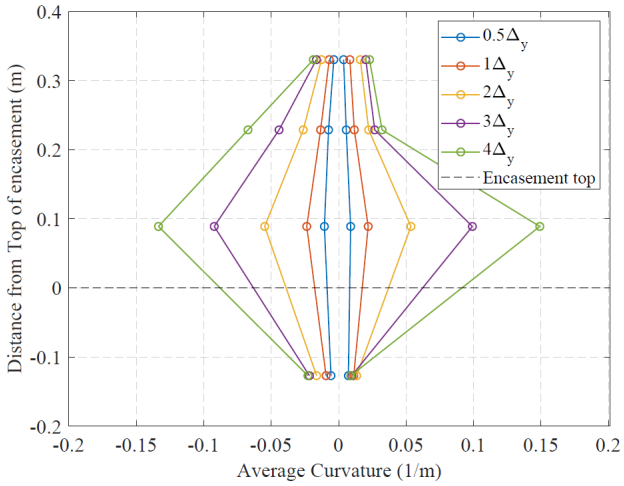

Figure 3.17: Curvature plot for specimen-1.

Curvatures for specimen-2 are plotted in Figure 3.18. The plot shows that the UHPC encasement did not undergo any rotation at the base. There is an increase of curvature at the termination of the encasement. This increase in the curvatures does not imply bulging but rather the opening and closing of cracks at the top of the encasement layer. Due to inherent difficulties in obtaining curvatures in plastic hinge zone of CFT, curvatures were not measured for specimen-3. The buckling of

the tube causes spurious movement of the linear potentiometers causing errors in readings.

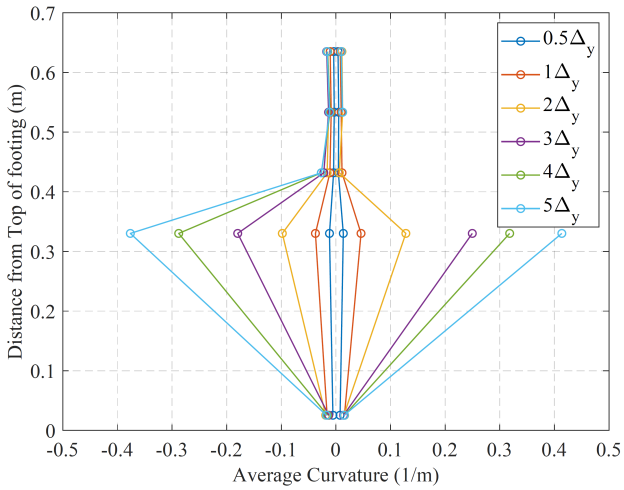

Figure 3.18: Curvature plot for specimen-2.

3.6.6 Tube Strains

Strains in tube were measured at different heights above the concrete footing which are shown in Figure 3.19 and Figure 3.20. The details on the location of strain gauges is provided in appendix Figure A.6. In the graph corresponding to the first specimen, it can be observed that the critical section was located above the UHPC encasement while the strain gauges located inside the footing either remained below or about the yield point. The first row of strain gauges inside the UHPC encasement were located above the first row of studs, that is the reason for large strains just under the top of encasement dashed line. Although this figure shows large strains in the tube at different level, the maximum strains occurred in the first 4 in. of the column from the top of encasement. There were no strain measurements in this region for the first test, but the extent of damage and buckling in this part is evidence of large strains, larger than recorded on the adjacent parts.

Strain profile in the steel tube for the second specimen is shown in Figure 3.20. As compared to the results from the first specimen, the level of maximum strains remained lower in the second specimen. After the observed push-out of the studs at about $3\Delta y$ displacement level, the strains in the tube did not increase substantially due to the rigid body motion of the CFT and the damage taking place in the UHPC encasement. The data at higher drift ratios are not reported since the strain gauges were damaged at these levels. Strains were observed for the dowel bars and footing longitudinal reinforcing bars and results showed that these reinforcing bars did not reach their yield point.

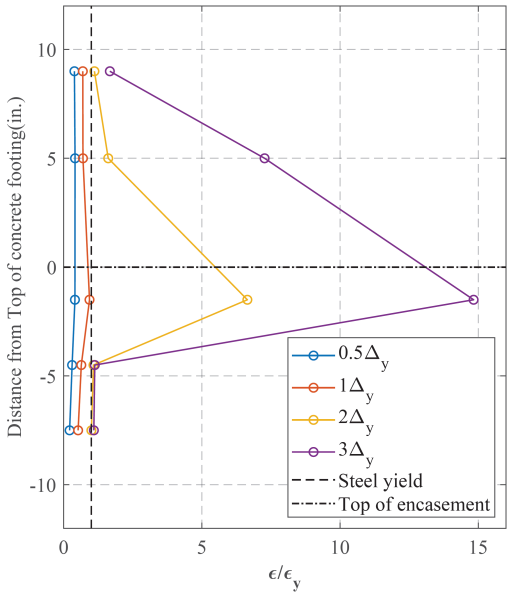

Figure 3.19: Strains in steel tube specimen-1.

3.6.7 Dowel Strains

The steel dowels were located in both specimens extending from footing to the UHPC layer. These dowels were instrumented with steel strain gauges to determine their response during the cyclic loading. The behavior of these dowel strains for

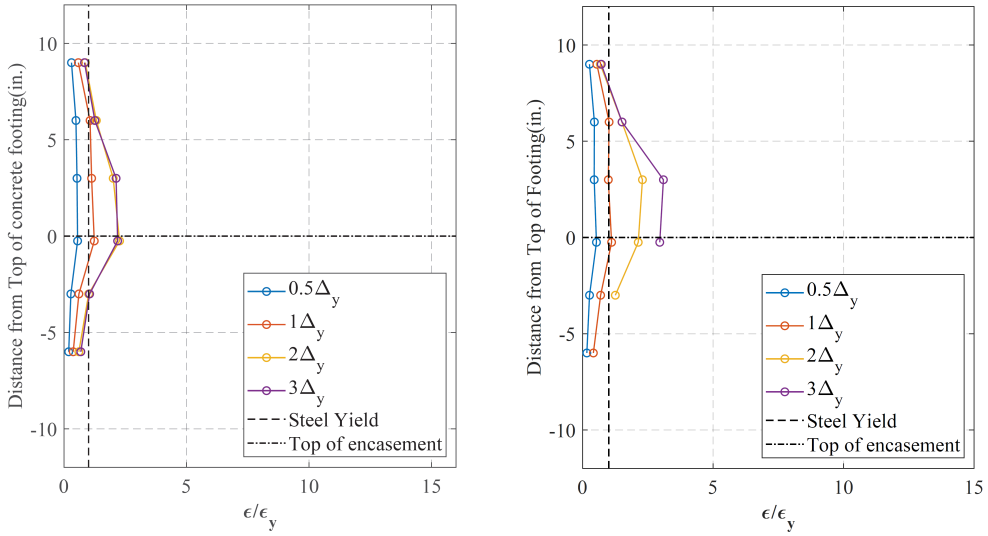

(a) Strain in Tube (North Side) (b) Strain in Tube (South Side)

Figure 3.20: Strains in steel tube specimen-2.

specimen-3 is shown in Figure 3.21. The plot shows the evolution of strains with increasing $\Delta y's$. As can be seen, the extreme dowels undergo maximum strains in the north (pull) and push (south) direction. The value of strains then decreases incrementally along the radial direction with minimum values for the east and west of the specimen. The diameter of the circle shows the magnitude of the strain in each dowel.

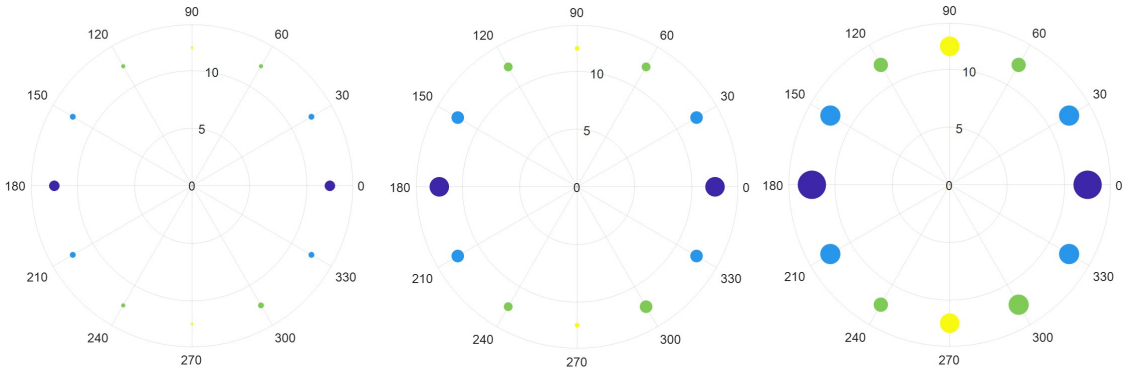

Figure 3.21: Outer layer dowel layout for specimen-3.

The response of the dowels in specimen-1 is plotted in Figure 3.22 and the north and south dowels showed almost a symmetric response. The results are plotted for different $\Delta y's$. Strains were observed for the dowel bars and footing longitudinal reinforcing bars and results showed that these reinforcing bars did not reach their yield point. At $7\Delta y$, the normalized strain is half of yield strain which means there was no inelastic strain in the dowels. The response of the dowel strain gauges for specimen-2 differed for north and south directions. During initial cycles, the dowels showed almost symmetric response but at $3\Delta y$, both north and south dowels showed asymmetric response due to crack opening and closing. As observed in Figure 3.23, the dowels exhibit either tension and compression strains for a complete cycle. However, at higher $3\Delta y$ the dowels on the south side were essentially in tension while the north dowels remain in compression during the cycle. This anomaly can be explained by the rigid body motion with a focal point located at the level of the encasement which was damaged at this point.

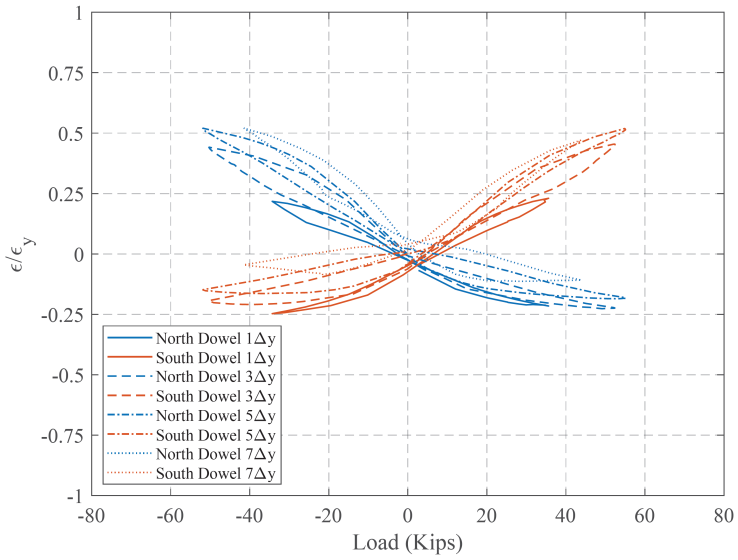

Figure 3.22: Strain in dowels of specimen-1 for different Δy.

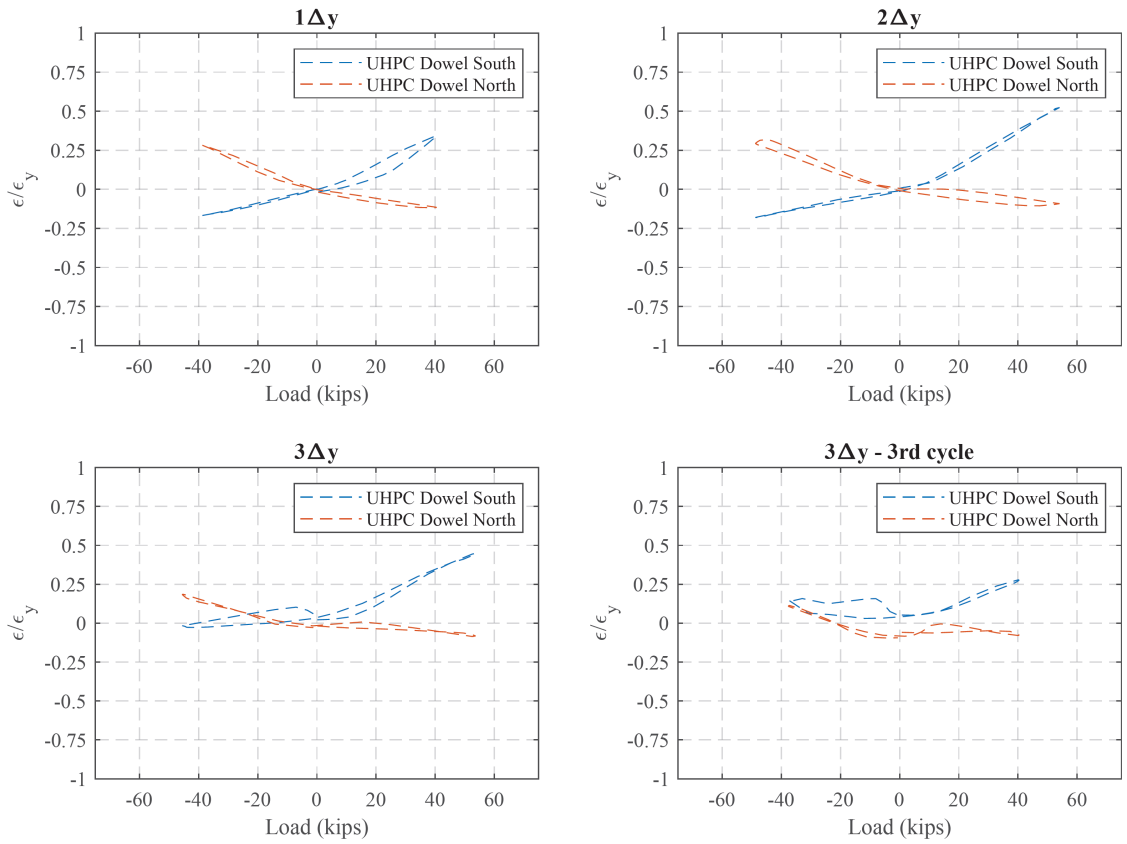

Figure 3.23: Strain in dowels of specimen-2 for different Δy.

3.6.8 Shear Connector Strains

The pretest FE analysis shows that the top layer of the shear connectors (parallel to the loading direction) is engaged at the onset of loading. For specimen-3, the shear connectors were arranged in a staggered pattern to reduce the center-to-center distance between the shear connectors. The shear connector in the direction of the loading was instrumented with strain gage.

Figure 3.24 shows the strain vs load for the shear connector for different Δy. The stud exhibits an asymmetric response in the push and pull direction. The compressive strain in the shear connectors is considerably lower than the tensile strains. Also, the hysteresis of the strain shows no increased area under the curve for higher Δy and strain softening is observed after peak load. The high initial stiffness

shows that the strains are engaged at onset of loading and provide sufficient shear and flexural resistance during the cyclic loading.

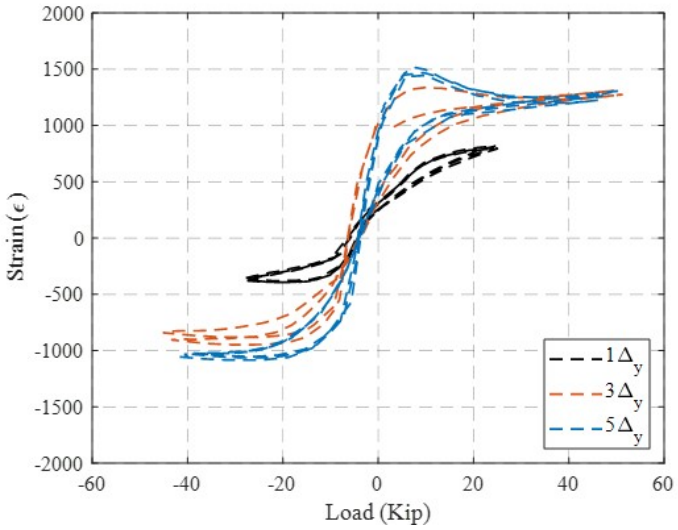

Figure 3.24: Strains in shear connector for specimen-3 for different Δy.

3.7 Comparison

All the specimens were almost identical in geometrical and boundary conditions. However, there was a slight difference in l/d ratio of the specimen due to increase in height of the encasement for specimen-2 and specimen-3. Despite these minor differences, a comparison can be established to understand the failure mechanisms of these specimen. The stiffness degradation is calculated using the following equation, where k_- and k_+ means stiffness of the specimen for each cycle [84].

$$K = \frac{K_+ + K_-}{2} \tag{3.4}$$

The stiffness degradation of the specimens are plotted in Figure 3.26. The concept of stiffness degradation, plotted in Figure 3.25, is calculated by estimating the

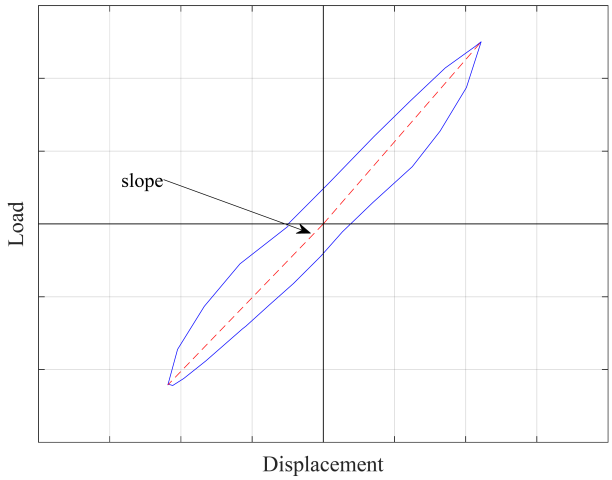

Figure 3.25: Stiffness degradation concept.

peak slopes for each cycle in load-displacement plots. As expected, due to lower l/d of specimen-2, the stiffness of the system is higher. The difference in stiffness can also be attributed to material properties. After initial displacements, the reduction in stiffness of specimen-2 is much greater than that of specimen-1 which is possibly due to cracking initiation in the UHPC encasement. As the displacement level increases, the stiffness of specimen-2 falls below specimen-1 which indicates softening of the system due to failure of the connection. The stiffness degradation of specimen-1 and 3 were quite similar. However, due to higher l/d of specimen-3, the stiffness was lower than specimen-1.

The energy dissipation of all specimen is compared in Figure 3.27. The energy dissipation is calculated by taking the area under the curve for each cycle. At initial cycles, the specimens have similar energy dissipation. On the onset of cracking in UHPC layer for specimen-2, the difference in energy dissipation diverges. At the end of the testing, the difference in the energy dissipated is almost twice for the specimen-1 which shows the superior performance of the embedded connection. Similar to stiffness degradation, the energy dissipation of specimen-3 was similar to specimen-1. The small difference is attributed to different l/d of these specimens.

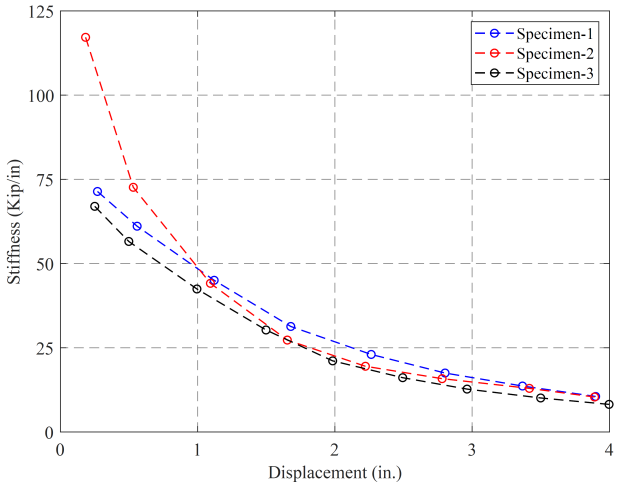

Figure 3.26: Comparison of stiffness degradation.

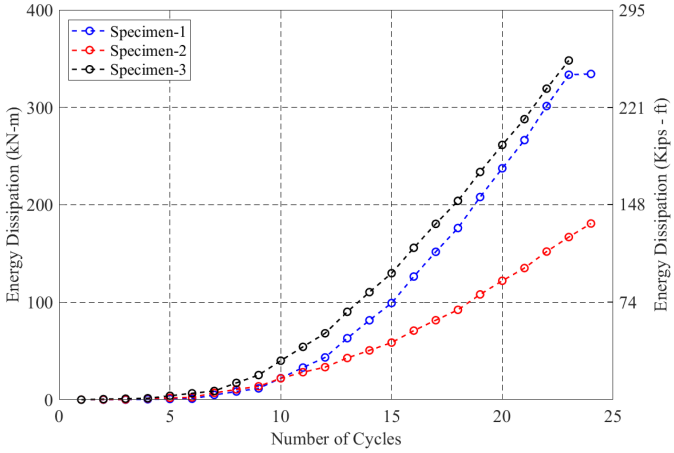

Figure 3.27: Comparison of energy dissipation.

The comparison of backbone curves is shown in Figure 3.28. The backbone curves are obtained by joining the peaks of each cycle of the lateral load. Due to similar d/t ratio of all the specimen, it was expected that the maximum load carried by the connection will be in similar range. The softening of the branch was similar and symmetric for all the connection types.

The comparison of moment vs drift ratio is shown in Figure 3.29. The axial load on the specimen was applied via spreader beam attached to high strength axial rods. The moment at critical section was calculated by summation of moment at the top

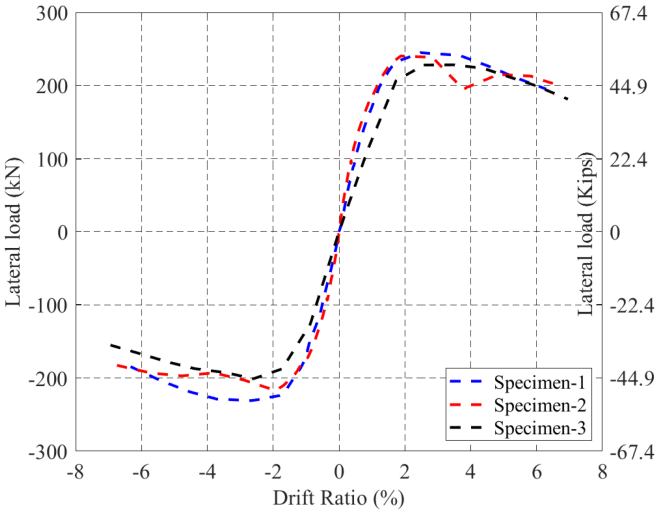

Figure 3.28: Comparison of backbone curves.

of the UHPC section including the P-Δ effect. The figure shows that specimen-1 and 3 have similar moment hysteresis but due to pinching behavior of specimen-2, the hysteresis loop is relatively smaller.

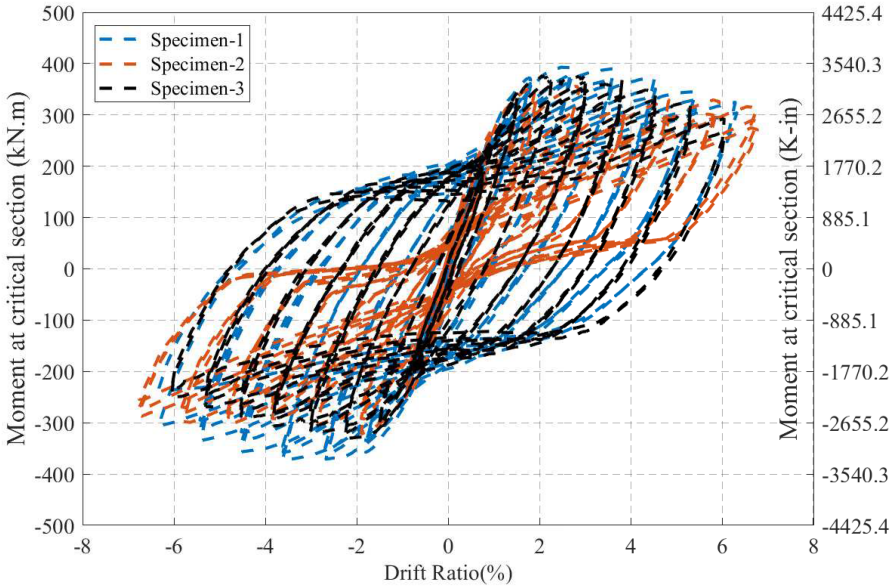

Figure 3.29: Comparison of moment hysteresis.

3.8 Discussion

One important aspect in designing a connection for connecting CFTs to footing using the concept presented herein, would be the design of shear connectors. As explained before the number of shear connectors provided was equal in all tests; however, in specimen-2, the top layer of shear connector pushed out of the UHPC as shown schematically in Figure 3.30. To overcome this issue, the depth of the top shear connectors and the dowel bars configuration should be considered.

As shown in Figure 3.20, the strain in the tube dropped significantly after the top layer of shear connector pushed out the UHPC. This indicates that the top layer of shear connectors was transferring large forces. The preferred mode of failure would be avoiding the breakout as it occurred in specimen-2. To avoid this type of failure, anchorage can be added for the top layer of shear connectors, or the dowels can be arranged such that they act as anchors for the shear connectors. In this case, the dowels should be developed above the failure surface, which would be feasible due to shorter development length required for UHPC.

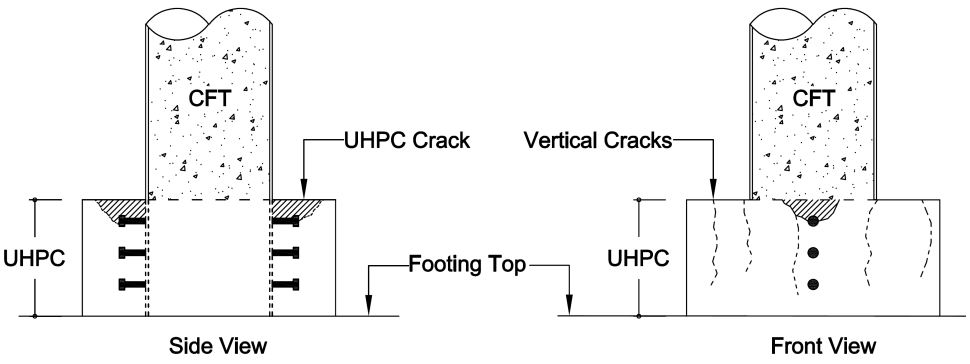

Figure 3.30: Schematic of damages in specimen-2.

An important design consideration that resulted in premature failure of specimen-2 is the vertical cracking of the UHPC encasement. It is believed that the UHPC encasement cracked mainly due to the shear transfer from the CFT to footing. The

UHPC encasement can be considered as two parts: the core (the part cast inside the tube) and the donut or ring (cast outside the tube), as shown in Figure 3.31a both parts are separated by the tube. The shear forces in the tube can be transferred partially to the core and the donut. The core portion of the encasement would not fail in a shear failure mode as the length of this cylinder is almost equal the depth of the section and it is confined by the tube. Therefore, this portion is more susceptible to flexural failure. Since the shear connector and dowels are placed outside the tube the transfer of the moment is mostly to the outer portion of the encasement (the donut). However, if shear forces are to be applied (partially or fully) to the donut this section can fail as shown in Figure 3.31b.

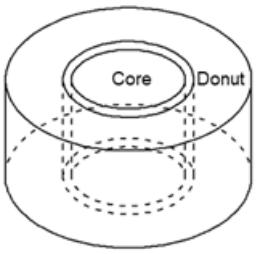

(a) Core and donut definition

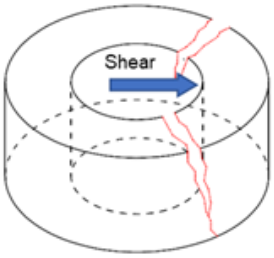

(b) Vertical cracking in the donut

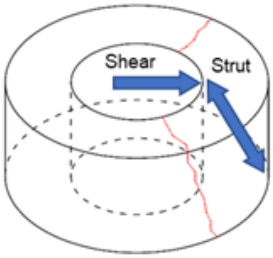

(c) Compression strut forming in the donut

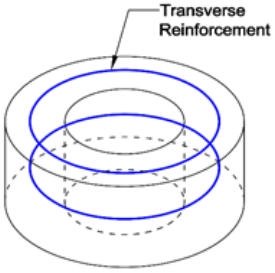

(d) Reinforcement for donut

Figure 3.31: Failure and load-transfer mechanism in the UHPC encasement.

In this case, the outer part of the encasement should be reinforced transversely to account for the shear transfer from the CFT to the footing. In specimen-1, due to partially embedment of the UHPC in the footing, the compression strut formed with a smaller angle and shear was fully transferred to the footing with minimal

cracking in the UHPC encasement (Figure 3.31c). It is recommended, as safety measure, that the transverse reinforcement should be provided for all cases above the footing surface (Figure 3.31d).

The proposed connection for CFT offers several cost benefits over precast concrete or cast in situ columns.The UHPC is strategically placed only in the connection region which is both economical and is ideally suited for ABC applications. These advantages are tabulated as follows:

- CFT columns do not require formwork and scaffolding which reduces construction cost. Also, in most applications, the reinforcement cage is not required which reduces material cost.
- The development length of steel reinforcement dowels is lower in UHPC when compared to NSC. The lower development length helps decrease the embedment and encasement depth.
- The recess in the footing for partially and fully embedded connection is lower which simplifies the reinforcement detail. For encased connection, the recess is not required but additional shear transfer mechanism may increase the cost.

3.9 Summary of Experimental Study

This study presents a new detail for CFT connections to precast members which is applicable for ABC applications. In this detail, steel dowels from footing are developed in a UHPC layer which also embeds the CFT. The reinforcement dowels are used for force transfer between the UHPC layer and the concrete footing. Due to high mechanical strength of UHPC, the development length of dowels can be reduced compared to grouted or NSC layer.

Three variations of the detail i) a partially embedded, ii) encased and, iii) completed embedded details were studied based on the location of the UHPC layer. For the embedded detail the UHPC was partially embedded in the footing. In the encased connection, the UHPC layer was placed completely outside the footing. For fully embedded, the entire UHPC layer was located inside the footing. The design of the specimen was based on an analytical study to evaluate the specimen's flexural capacity at critical sections. Based on these analyses, an experiment was carried out to evaluate the performance under a combination of constant axial and incremental lateral cyclic loads. The behavior of the connection showed varying response. The encased connection performed relatively poorly due to lack of shear mechanism in the UHPC layer. The partially embedded detail performed superior without developing any significant cracks in the UHPC region. The completely embedded connection detail showed favorable response by fracture of the tube outside the UHPC layer.

To complement the experimental study, a finite element analysis is carried out in the next section. The calibrated finite element model is used to perform a parametric study on different parameters of the design.

CHAPTER 4

NUMERICAL ANALYSIS ON CFT CONNECTION DETAILS

4.1 Introduction

The previous chapter presented details of the experimental program which consisted of three connection details. It is neither economical nor feasible to experimentally study the effect of all connection parameters. For the experimental program, the effect of shear connectors, axial load, strength of UHPC, dowels and many other factors were not evaluated. To complement the results of experimental study, an elaborate 3D non-linear finite element analysis (NLFEA) was carried out. This chapter presents the details of numerical analyses and after calibration with experimental and pretest finite element anlaysis, a parametric study was carried out. on various of CFT to footing or cap beam connections.

4.2 Methodology

The results of the experimental program showed two different kinds of failure modes depending on the embedment location and shear connector configuration. The undesired failure mode can be suppressed by either confining the UHPC layer with transverse reinforcement or embedding the connection completely in the footing. It is therefore desired to identify the parameters which can effect the connection. A detailed study is presented earlier on the behavior of shear connectors under different loading conditions to better comprehend the behavior and provide a basis for design of these shear connectors in the connection region. The results of the pretest finite element analysis and experimental study is used to model complete specimens. This

chapter presents a numerical study on various parameters which affect the behavior of the connection.

4.3 Finite Element Analysis of CFT Connections

Full scale model of all connection details were modeled using Ansys. The geometric properties and material properties of the specimen are detailed in earlier sections. Symmetry conditions were not used in the model. A displacement is applied on the specimen unidirectionally along one of the axis. The translation at the bottom of footing was fixed in all directions. Since no rotation was observed between the encasement and the concrete, a fixed contact surface was used between these two interfaces. The axial load is applied as a remote force at the top surface of the model. A fine mesh is used in the UHPC encasement. The reinforcement in the footing and UHPC layer is modeled using 2-D beam elements. A friction coefficient of 0.41 was used between the steel tube and in-fill concrete. The model and boundary conditions are shown in Figure 4.1. The partially and fully embedded details were modeled using similar approach. The force was monitored for the applied displacement.

The deformed shape and the von-Mises stress state for specimen 1 and 3 is shown in Figure 4.2. The stress state for both the specimens show development of compressive stress near the plastic hinge zone (for the loading direction). The deformed shape shows the development of buckling above the location of the UHPC encasement. Since the load was applied monotonically along one of the axis, the evolution of progressive buckling in the specimen was not captured. The encased connection (not shown here) showed similar stress state for the steel tube but extensive compression damage was also observed in the UHPC layer. The tension damage in microplane concrete is shown for specimen 1 and 3 is shown in Figure

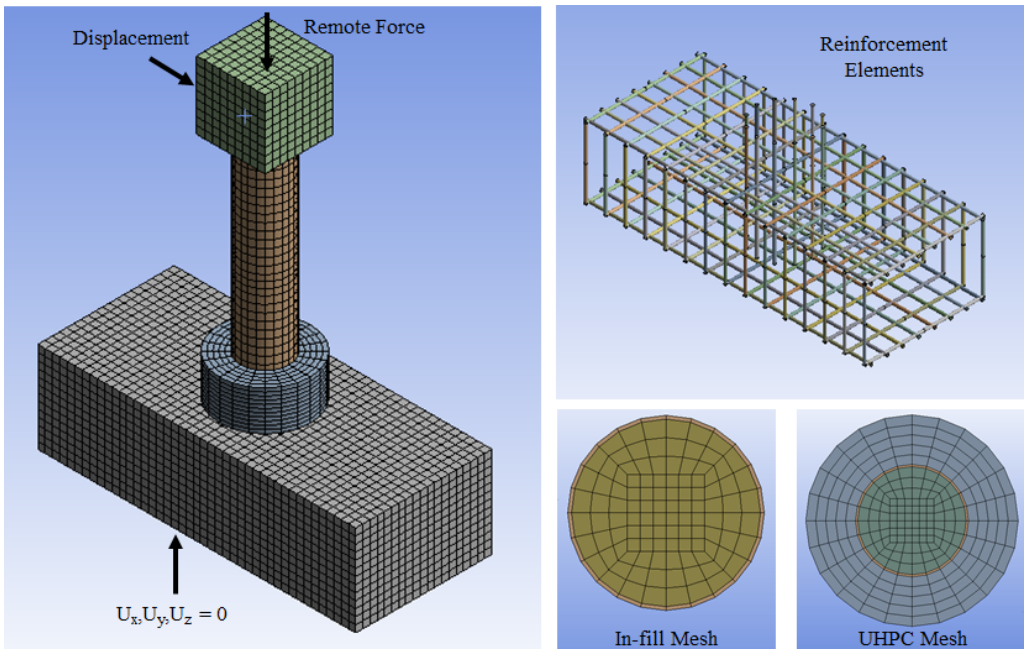

Figure 4.1: Finite element model for the CFT connections.

4.3. The figure shows that the concrete sustains tension damage along the direction of loading. The tension damage is more pronounced in specimen-1 as compared to specimen-3.

The results for the load displacement comparison are plotted in Figure 4.4. The ascending branch of the load displacement has good agreement with the experimental results but the degradation of the stiffness and damage evolution is not predicted with high accuracy. For specimen-2, the stud pull-out caused premature failure of the encasement which caused abrupt drop in load and this was not observed in the FE model. A more elaborate calibration of cyclic loading for the microplane model used for the UHPC and concrete can provide the evolution of damages and possibly predict the stiffness degradation after maximum load.

The difference between experimental and numerical results is given in Table 4.1. The error varies between 2 (%) and 8 (%) for specimen-1 to specimen-3 for the backbones values of push loading.

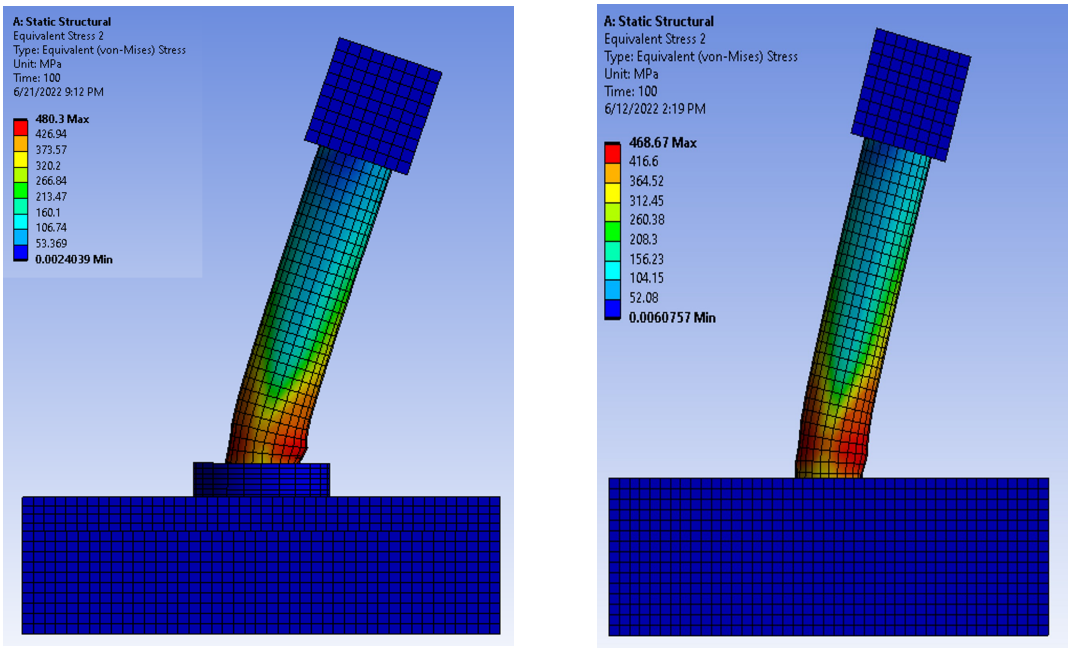

(a) von-Mises stress specimen-1

(b) von-Mises stress specimen-3

Figure 4.2: Deformed shape and von-Mises stress for specimen-1 and 3.

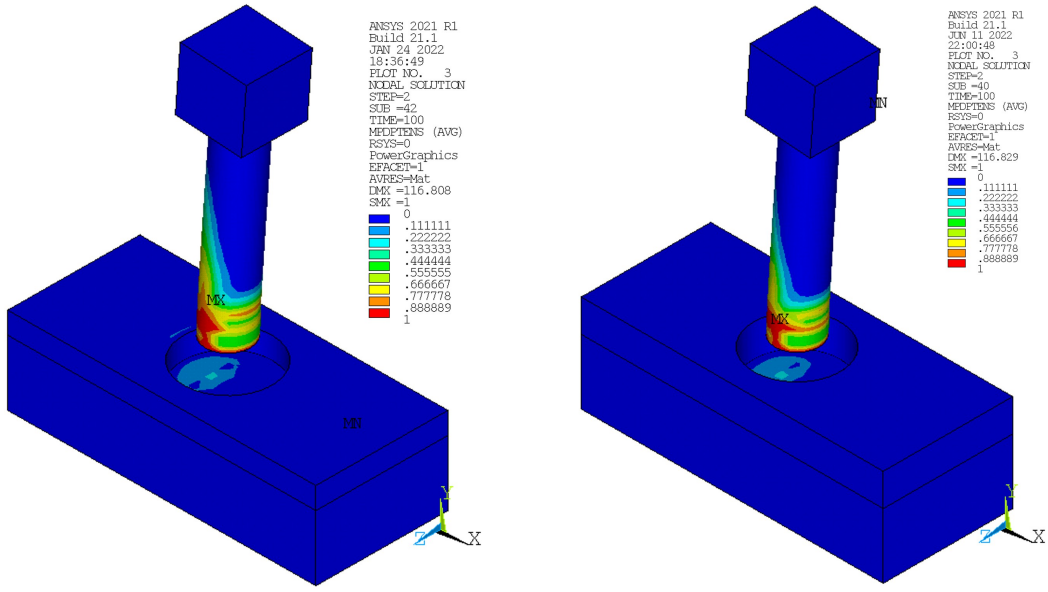

(a) Tension damage in specimen-1

(b) Tension damage in specimen-3

Figure 4.3: Tension damage in specimen-1 and specimen-3.

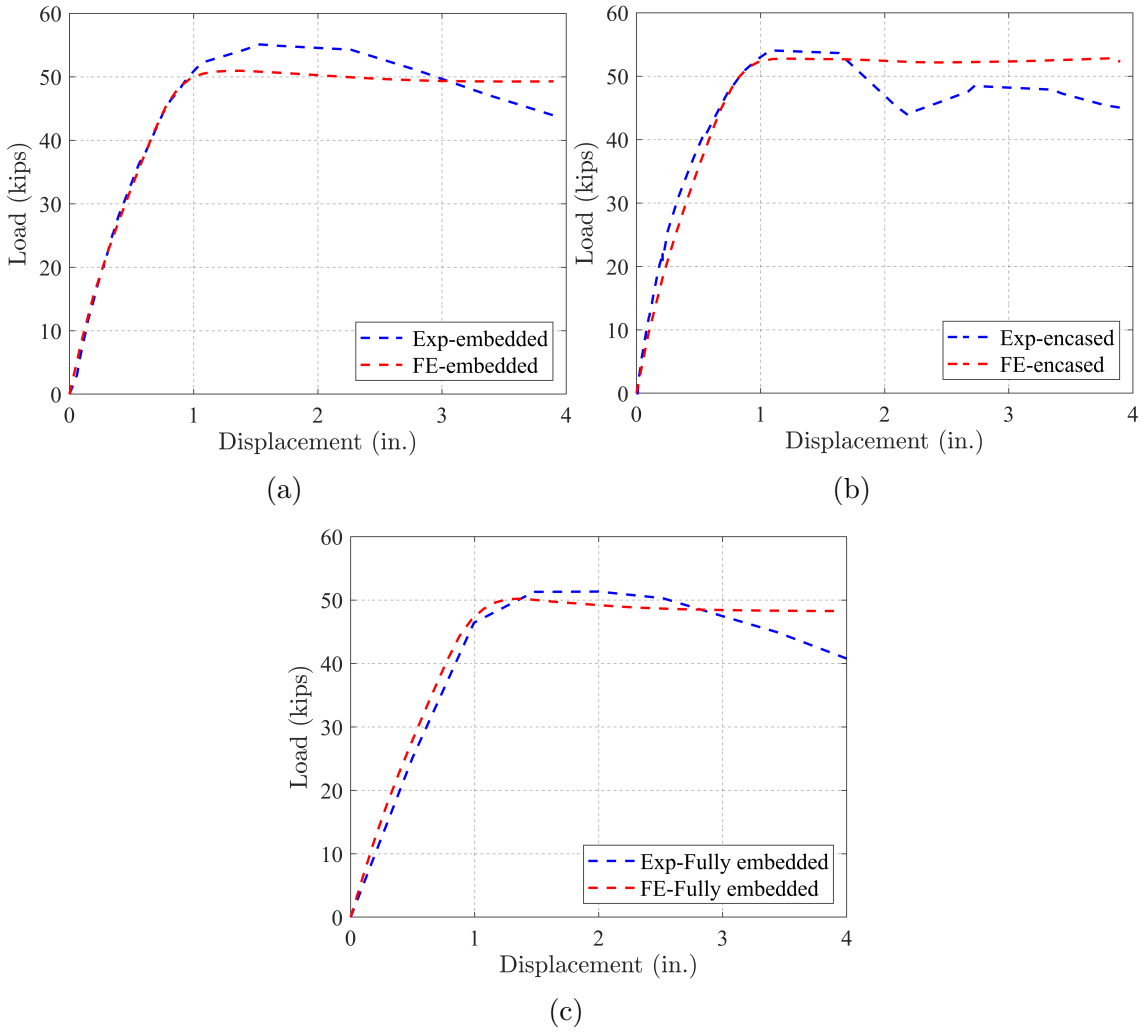

Figure 4.4: Comparison of experimental and numerical model for a) partially embedded, b) encased connection and, c) fully embedded connection.

Table 4.1: Error between Experiment and FE analysis

Specimen	**Experimental (Kips)**	**Finite Element (Kips)**	**Error** (%)
Specimen-1	55.1	50.96	7.51%
Specimen-2	54.06	52.80	2.34%
Specimen-3	51.34	50.20	2.22%

4.4 Parametric Studies

The numerical model for the connections shows there is an interaction of different components. Based on these analysis, a parametric analysis is carried out to com-

prehend the influence of important parameters on the experimentally tested CFT connection. The parameters that are varied includes material, geometric and loading properties.

4.4.1 Effect of Yield Strength of CFT

The yield strength of the steel tube plays an important role in the behavior of CFT. For most commercially available spiral weld tubes the yield strength varies 350 to 400 MPa, therefore for the parametric analysis, the yield strength $f_{y(cft)}$ is varied from 350 to 450 MPa in increments of 50 MPa. As anticipated, the maximum load carried by the specimen is proportional to the yield strength. However, no change in the initial part of the slope is observed. The rate of increase or decrease in the load (for change in yield strength) was similar for all the specimen as shown in Figure 4.5.

4.4.2 Effect of Axial Load Ratio

Axial load ratio is one of the most important parameters in testing of columns for seismic applications. The higher axial load has significant bearing on the seismic performance of a column. Literature has shown that the strength, stiffness and deformation capacity is largely influenced by axial load [85]. Due to the limitations of the test setup, it was not possible to apply high axial load ratio. Therefore, the calibrated model is used to apply axial load of 20%, 40% and 50%. The results for the three specimen is shown in Figure 4.6.

The results show that as the axial load is increased, the specimen sustain more damages in the connection region. The peak load of the specimens is reduced significantly with increase in axial load levels. The load deformation also shows a dif-

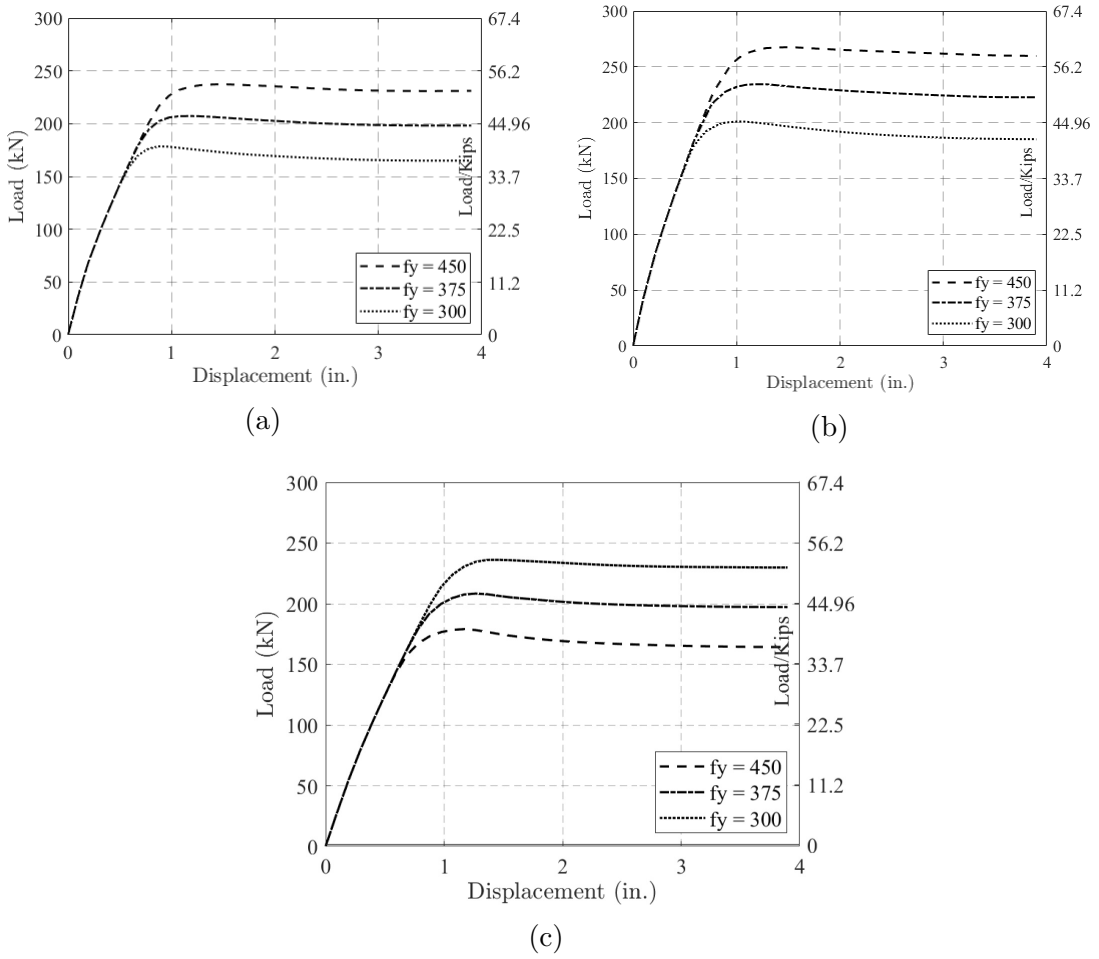

Figure 4.5: Effect of f_y on load-displacement relation of a) embedded, b) encased and, c) fully embedded connection.

ferent behavior with the load level. Higher axial load changes the load deformation response to an abrupt peak and valley curve. The decrease in the load deformation for specimen-1 to specimen-3 for 20% axial load is 2.45%, 3.33% and 2.08%, respectively. The decrease in the load deformation for specimen-1 to specimen-3 for 40% axial load is 21.31%, 25.06% and 21.39%, respectively. The decrease in the load deformation for specimen-1 to specimen-3 for 50% axial load is 34.89%, 38.77% and 35.03%, respectively. The secant stiffness of the specimens varied marginally but before peak load, but the stiffness slope drops at an increased rate with higher axial load.

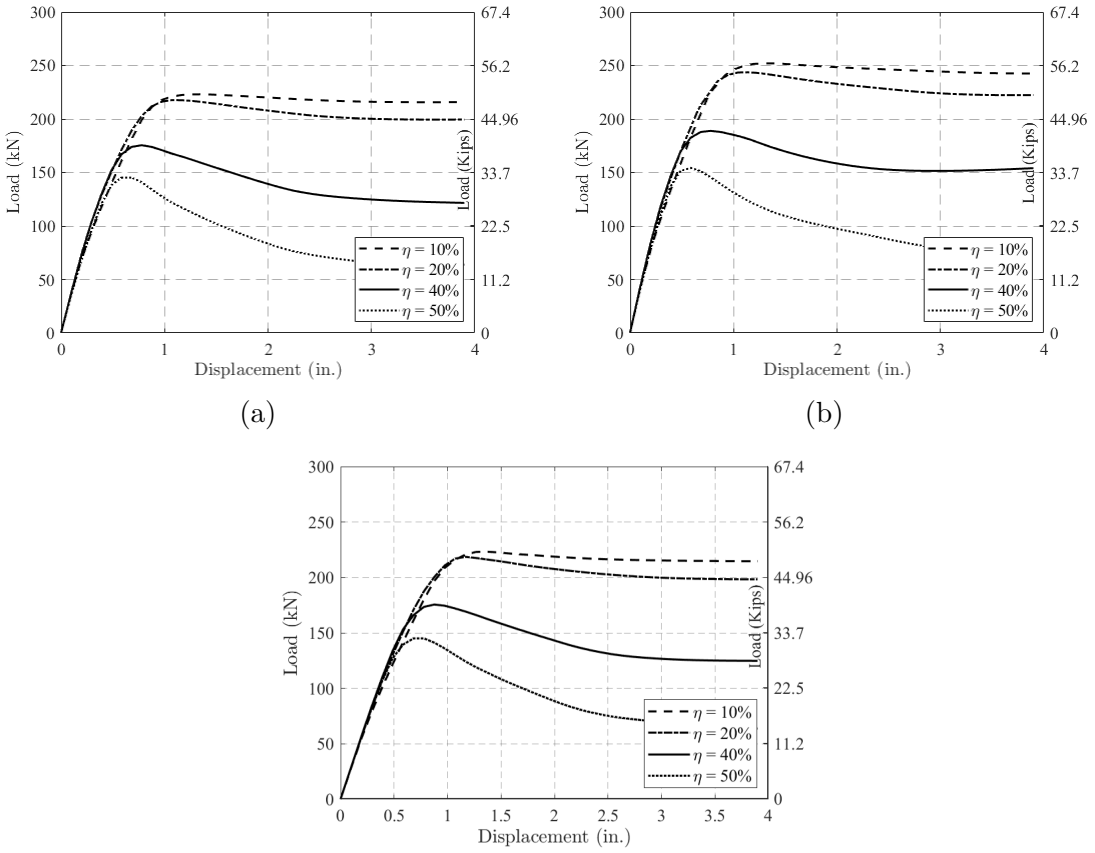

Figure 4.6: Effect of axial load ratio η on load-displacement relation of a) partial embedded , b) encased and, c) fully embedded connection.

4.4.3 Effect of Diameter to Thickness Ratio

The effect of diameter of tube (d) and the thickness of tube is shown here. Although, the diameter of the tube is kept constant, the thickness is incrementally varied from 1/8 in to 3/8 inches. The matrix for the analysis is provided in Table 4.2. The result for specimen-3 is plotted in Figure 4.7 and the trend is similar to the effect of yield strength of CFT.

For the test matrix, the material properties are kept constant and only the effect of d/t is evaluated. As can be seen in Figure 4.8, as d/t increases, the area of steel is reduced. This in turn also reduces the lateral loading carrying capacity of the section.

Table 4.2: Parameters for evaluating effect of d/t ratio

Parameters	**d**	**t**	A_s/A_c	**d/t**
Specimen-1 - 3	12.75	0.125	4.04%	102
	12.75	0.1875	6.15%	68
	12.75	0.25	8.33%	51
	12.75	0.375	12.89%	34

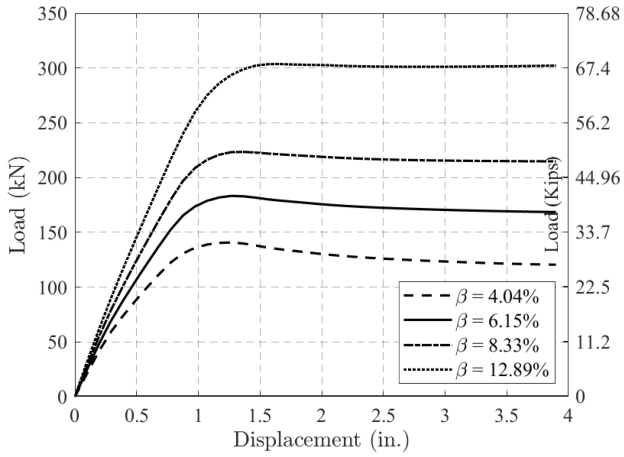

Figure 4.7: Effect of d/t on load carrying capacity for fully embedded connection.

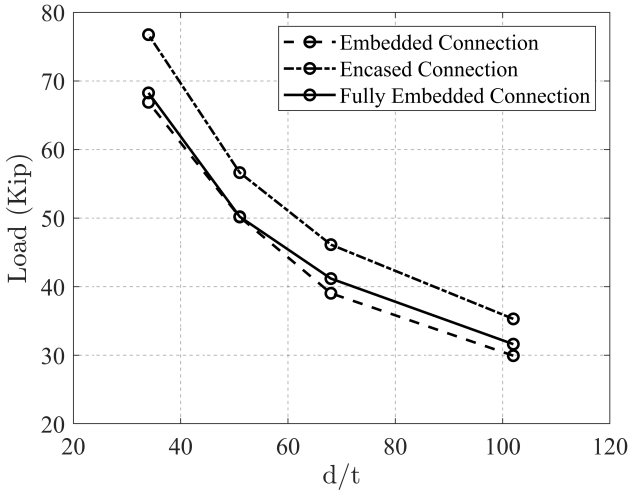

Figure 4.8: Effect of d/t on load carrying capacity.

4.4.4 Effect of Shear Connectors

In the previous section, the FE model consisted of bonded connection between the steel tube and UHPC. The shear connectors were not explicitly modeled. The ra-

tional behind the simplified approach was that in all the test results, significant gap between steel tube and UHPC was not observed. Although this approach provided good agreement with experimental results, the effect of shear connectors on connection parameters was not evaluated.

In order to understand the performance of shear connectors, a refined model was used. The modeling approach in the pretest FE modeling was used in defining the refined model as shown in Figure 4.9. Symmetry conditions were used in this approach and only half of the connection region was modeled. Since the results of the experimental study showed that the footing remained elastic, therefore the footing was not modeled. The shear connectors were modeled using 2 mm (0.078 in.) hexahedral elements. A friction surface was modeled between: i) in-fill concrete and steel tube, ii) UHPC and steel tube and, iii) shear connector faces and UHPC. Since in all experiments, the shear connector did not fracture at the weld collar, therefore the interface between shear connector and the steel tube was modeled as bonded. The computational time for the model was high due to fine mesh. The displacement was modeled using a rigid link and a remote force was applied on the top of the column. The bottom surface was fixed for all translations.

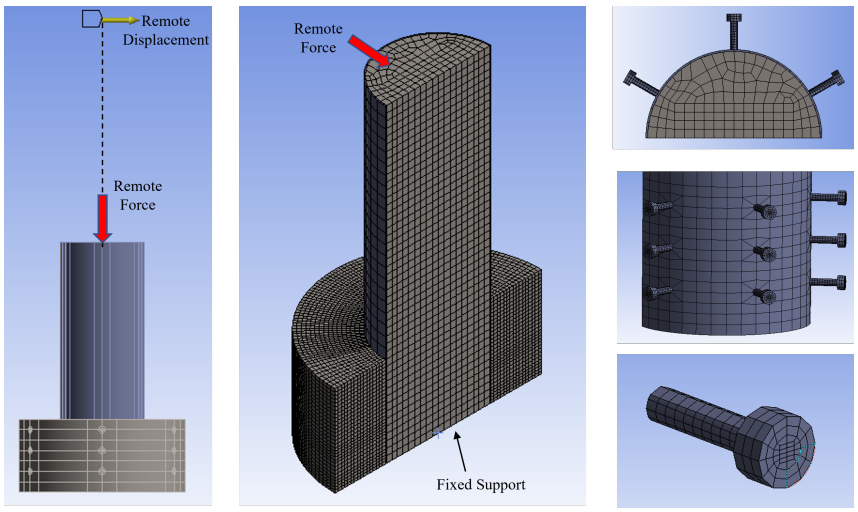

Figure 4.9: Finite element model of connection details with shear connectors.

Figure 4.10 shows the buckling of the tube and the von Mises stress in stud connectors at maximum displacement. The FE results show that the top layer of shear connectors contribute maximum resistance and which reduces with the depth of the connectors. This difference in contribution was also observed in the pretest FE study for both push-out tests and affect of grouped connectors. The steel tube develops stress in the entire region surrounding the UHPC layer but buckles outside the boundary of encasement.

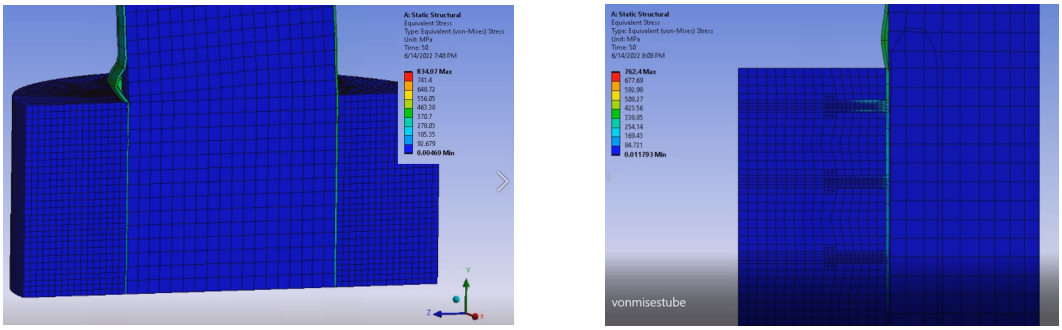

(a) Buckling of tube (b) Section showing von Mises for connectors

Figure 4.10: Failure pattern for refined model.

The effect of number of connectors is also modeled. Two cases are considered: i) nine shear connectors and, ii) six shear connectors. The comparison of load deflection for fully embedded, nine and six connectors is shown in Figure 4.11. The model with shear connector is able to show softening of the backbone curve which was not observed in the bonded connection models. The six connector showed lower maximum load and a higher ductility than the nine connector model.

4.5 Summary of Finite Element Analysis

A detailed FE analysis was carried out on an all connection types. Prior to modeling the CFT experiments, a pretest finite element study was carried out using existing experiments from the literature.

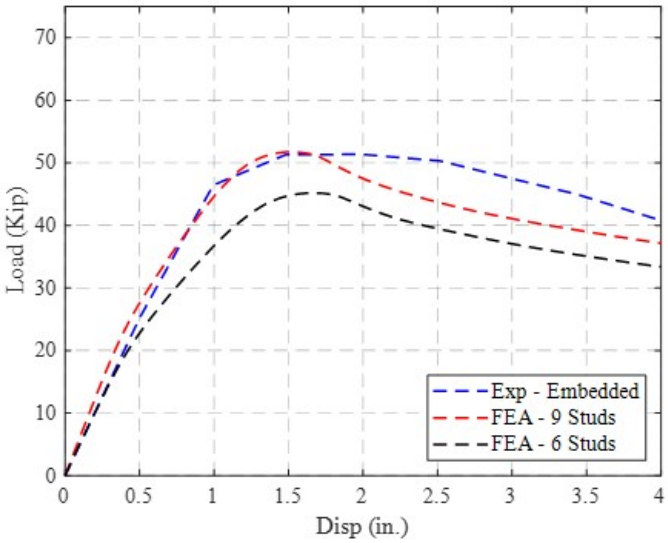

Figure 4.11: Finite element model of connection details with shear connectors.

The results showed that the increasing the yield strength of the tube improves the lateral load carrying capacity. However, significant difference is not observed when material strengths of in-fill concrete and UHPC are changed. Also, the axial load ratio has significant bearing on the load displacement plot. Higher load ratio causes an abrupt drop in loading carrying capacity after the peak load. The effect of d/t ratio on the specimens is similar to that of the material strength; the higher the ratio of the steel tube to concrete, the larger the force carried by the member.

CHAPTER 5

CONCLUSIONS

5.1 Highlights and Contributions

This research presents a new detail for CFT to precast concrete component (cap beam or footing) using a UHPC layer which is feasible for ABC applications. A literature review of the past research has shown the effectiveness of an embedded and encased connection over other CFT connections. Due to high mechanical strength of UHPC, the embedment length can be reduced compared to grouted or NSC layer. An analytical study was performed to evaluate the specimen flexural capacity at critical sections. Based on this, an experimental program was designed to evaluate the performance of the system under a combination of constant axial and incremental lateral cyclic loads. Following is the summary and conclusion of the research program:

- A new connection detail is envisioned with potential applications for substructures of high speed rail network. The inherent construction benefits of CFT and construction sequence of proposed connection provides an alternative to precast and in-situ concrete columns.

  Pretest Finite Element Analysis

- Pretest finite element analysis on different parameters of the proposed connection detail. Element types, material models and loading conditions were modeled which best represented confined concrete, UHPC and shear connector behavior under different loading conditions. Microplane model for UHPC and NSC was calibrated for confined and unconfined concrete using experiments from past literature.

- Behavior of shear connectors under push off and tension loading was evaluated using experiments from literature. The results showed that the weld collar in push off tests contribute to slip resistance. The length of shear connectors in tension did not contribute significantly to load resistance. However, the tension pull out of connector located in UHPC slightly increased when compared to NSC. Similarly, the effect of group connectors was evaluated using past literature. The effect of group connectors showed overlap of compression damages which can reduce the load carried by connectors in close vicinity.

  Partially Embedded Connection

- The partially embedded connection was able to reach a drift ratio of 6.3% and load-hysteresis curve showed a symmetrical response with sufficient energy dissipation. On the second cycle of $7\Delta y$ the steel tube underwent ductile tearing which is the preferred mode of failure.

- Minor cracking was observed in the UHPC at initial cycles which is attributed to a construction deficiency. These cracks did not propagate during the remaining course of testing. On the other hand, the precast RC component, which was designed as capacity protected element, did not undergo any damage.

  Encased Connection

- The encased connection suffered significant damages in the UHPC step. This failure is attributed to insufficient cover on shear connectors which protruded out of the UHPC at initial load levels. The specimen did not exhibit sufficient energy dissipation despite reaching a drift ratio equivalent to encased type connection.

- The push out of shear connectors is due to insufficient shear resistance of the encasement. To prevent damages in the UHPC layer, it is recommended that transverse reinforcement is provided in the encasement.

  Fully Embedded Connection

- The fully embedded connection exhibited favorable failure mode with plastic hinge zone located completely outside the precast element. The specimen failed after sufficient energy dissipation and testing was halted after ductile tearing of the tube was observed.

- For fully embedded connection the embedment depth was reduced from 0.75 times the external diameter of the tube which is 25% less than the partially embedded connection and 10% less than the encased connection. The significant reduction in fully embedded connection is attributed to high mechanical strength of UHPC.

- For all specimens, the results from strain gauges showed that the strains in the steel tube remained below the yield strain at initial Δy but higher strain values were observed with progress of testing. The strains in the steel tube for both connections showed that the critical location of stress is located just above the UHPC step.

- The steel strains observed in the dowels and RC component reinforcement for all specimens showed that the strain remained below yield. For all specimens, the capacity protected element did not suffer any damages. Separation between the steel tube and the UHPC step was observed for all specimens at higher Δy.

- The stud in fully embedded connection was instrumented with strain gage. The results show that the stud undergoes high strain at the onset of loading

which softens with increasing drift ratio.

Finite Element Analysis and Parametric Study

- FE model with fixed contact surface between tube and UHPC shows good agreement with the experimental results but does not capture the softening behavior.
- The effect of material and geometric properties is evaluated and shows that increase in yield strength and area of steel ratio improves the load carrying capacity. However, change in mode of failure is not observed.
- The effect of axial load ratio shows that an increase in axial load results into a decrease in load carrying capacity and more localized damages in the UHPC and infill concrete. The slope of the descending branch of the load displacement changes from a softening regime to a peak and valley curve.
- Using symmetry region and high-resolution finite element model is modeled for effect of shear connector on the mode of failure. The model captures the contribution of shear connectors and is able to predict better represent the softening branch of the experimental results.
- The pretest FE analysis and parametric study on connection shows that the shear connector located nearest to the surface transfers maximum stress and therefore requires adequate cover.

5.2 Recommendation for Future Study

The study presented an experimental investigation for the design of CFT connection to precast concrete member. Based on the results, recommendations were provided to achieve desired failure mode. Additional work is recommended on the following:

- Evaluating the connection by extending the force transfer mechanisms to different details including but not limited to shear connectors, stiffened plates or a combination of multiple mechanism etc.
- Experimentally and numerically investigate the loss of stiffness and strength of the member when subjected to fire.
- Evaluate the performance of the connection in marine environment when subjected to cross section loss due to corrosion.
- Perform a shake table analysis to assess the performance of the connection under ground motion of an actual seismic event.

APPENDIX A

MISCELLANEOUS DETAILS

(a) Reinforcement cage

(b) Formwork

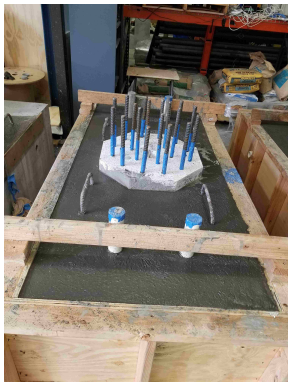

(c) Casting of RC component

(d) Removal of styrofoam

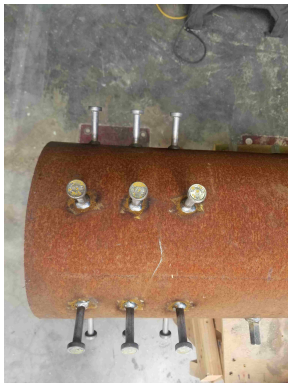

(e) Shear connectors welded on tube

(f) Steel dowels

Figure A.1: Construction details of specimen 1.

(a) Corrugated interface

(b) Groove dimension

(c) Steel strain gauges

(d) Sonotube for encasement

(e) Reinforcement of loading block

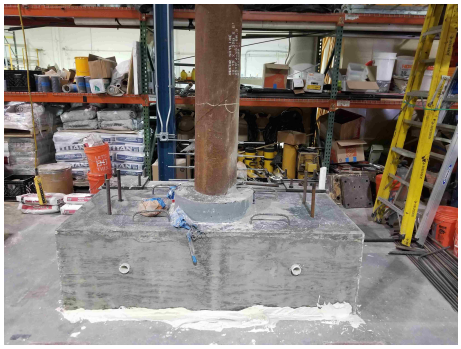

(f) Completed specimen

Figure A.2: Construction details of specimen 1.

(a) Reinforcement cage

(b) Casting of concrete

(c) Roughened interface

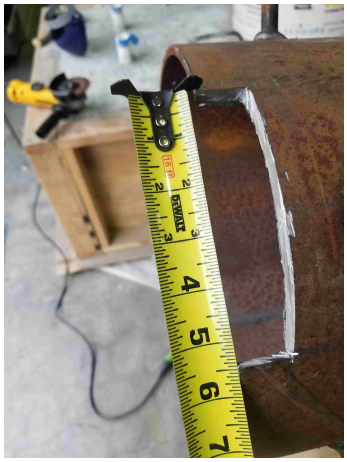

(d) Groove dimension

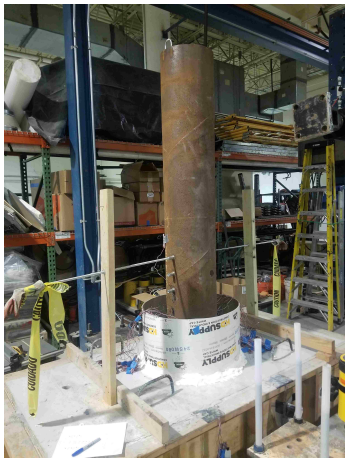

(e) Casting of UHPC

(f) Completed specimen

Figure A.3: Construction details of specimen 2.

(a) Reinforcement cage

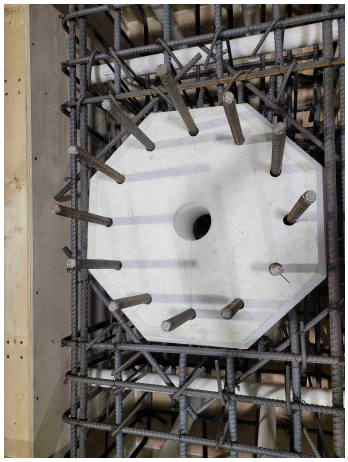

(b) Dowel arrangement

(c) NSC interface

(d) Roughened interface

(e) Stud pattern

(f) Groove detail

Figure A.4: Construction details of specimen 3.

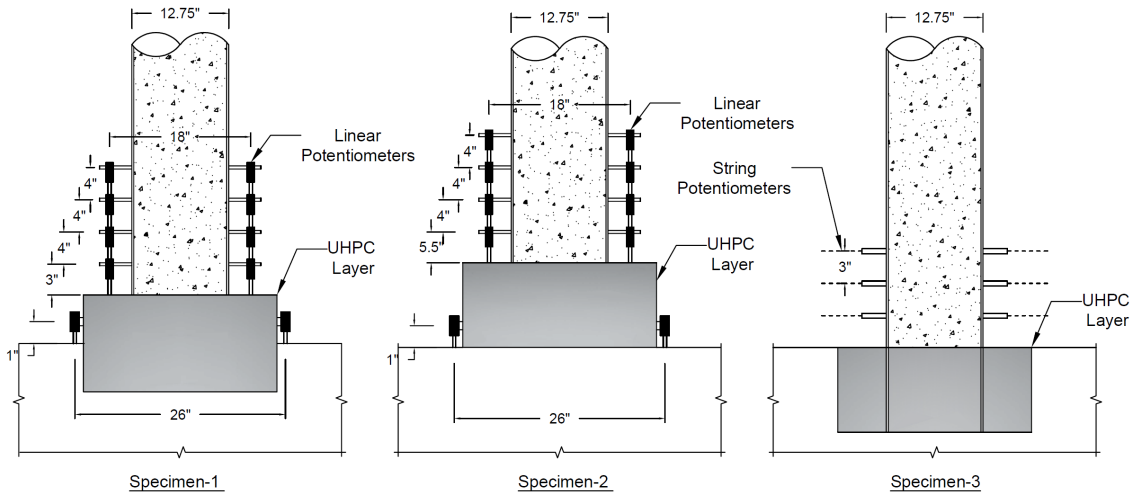

Figure A.5: Instrumentation detail for specimen-1, 2 and 3.

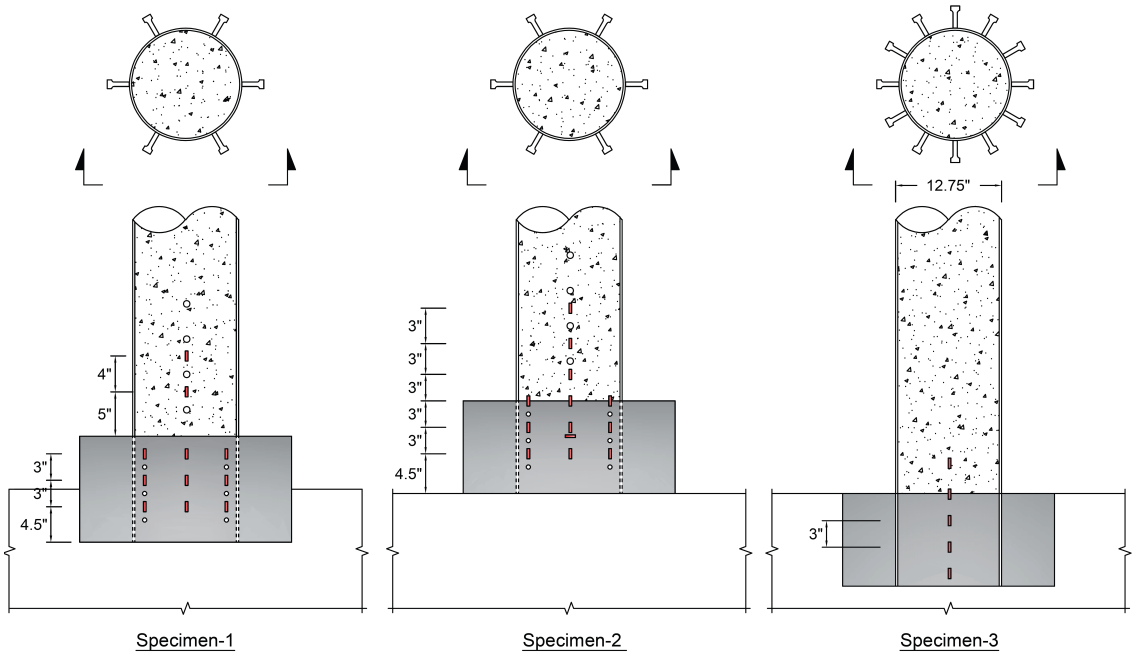

Figure A.6: Location of strain gauges for specimen 1, 2 and 3.

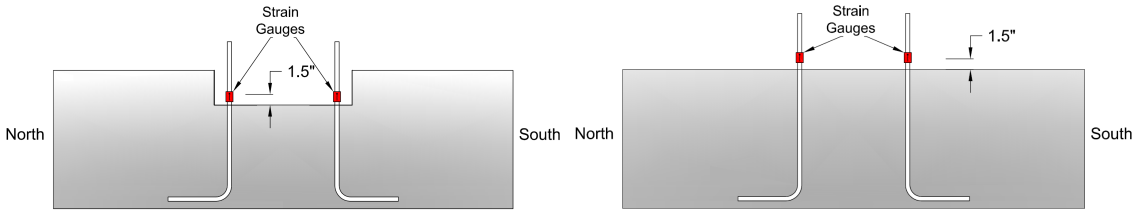

(a) Specimen 1 (b) Specimen 2

Figure A.7: Location of strain gauges in UHPC dowels for Specimen 1, 2 and 3.

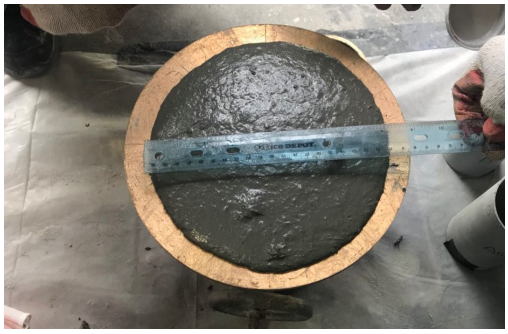

(a) Static Flow test

(b) Testing on 3” x 6” UHPC cylinders.

Figure A.8: UHPC material testing.

(a) NSC cylinders

(b) Testing on 4” x 8” NSC cylinders.

Figure A.9: NSC material testing.

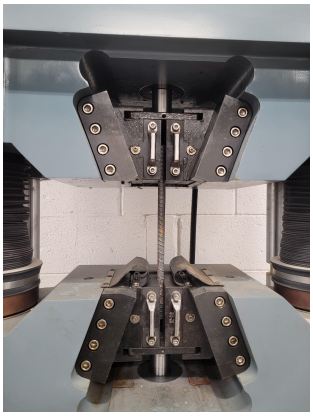

(a) Steel tensile test

(b) Rebar fracture.

Figure A.10: Failure of specimen.

BIBLIOGRAPHY

[1] Robert S Kirk and William Mallett. Highway bridge conditions: Issues for congress. 2013.

[2] ASCE. 2017 infrastructure report card. ASCE Reston, VA, 2017.

[3] Chongjie Kang, Sebastian Schneider, Marc Wenner, and Steffen Marx. Development of design and construction of high-speed railway bridges in germany. *Engineering structures*, 163:184–196, 2018.

[4] Nan Hu, Gong-Lian Dai, Bin Yan, and Ke Liu. Recent development of design and construction of medium and long span high-speed railway bridges in china. *Engineering Structures*, 74:233–241, 2014.

[5] Shunquan Qin and Zongyu Gao. Developments and prospects of long-span high-speed railway bridge technologies in china. *Engineering*, 3(6):787–794, 2017.

[6] Terry Gourvish. The high speed rail revolution: history and prospects. *Report of High Speed*, 2, 2010.

[7] Frédéric Dobruszkes. High-speed rail and air transport competition in western europe: A supply-oriented perspective. *Transport policy*, 18(6):870–879, 2011.

[8] LMD Arema. American railway engineering and maintenance-of-way association. *Manual for railway engineering*, 2013.

[9] Yinghong Cao, Todd Ude, Daniel Getter, and Brendan Gill. Design of high-speed railway bridges with earthquakes in the united states. *Structural Engineering International*, 29(1):18–25, 2019.

[10] Michael P Culmo, Byron Lord, Mary Huie, and Benjamin Beerman. Accelerated bridge construction: Experience in design, fabrication and erection of prefabricated bridge elements and systems: Final manual. Technical report, United States. Federal Highway Administration. Office of Bridge Technology, 2011.

[11] Michael P Culmo et al. Connection details for prefabricated bridge elements and systems. Technical report, United States. Federal Highway Administration. Office of Bridge Technology, 2009.

[12] Azadeh Jaberi Jahromi, Alireza Valikhani, Islam M Mantawy, and Atorod Azizinamini. Service life design of deck closure joints in abc bridges: Guidelines and practical implementation. *Frontiers in Built Environment*, page 152, 2020.

[13] Y F Yang and LH Han. Concrete filled steel tube (cfst) columns subjected to concentrically partial compression. *Thin-Walled Structures*, 50(1):147–156, 2012.

[14] Charles Roeder, Dawn Lehman, Ashley Heid, Todd Maki, et al. Shear design expressions for concrete filled steel tube and reinforced concrete filled tube components. Technical report, Washington (State). Dept. of Transportation. Research Office, 2016.

[15] Z Lai and AH Varma. Analysis and design of noncompact and slender concrete-filled steel tube (cft) beam-columns. In *Proceedings of the Annual Stability Conference Structural Stability Research Council*, 2014.

[16] Lin-Hai Han, Wei Li, and Reidar Bjorhovde. Developments and advanced applications of concrete-filled steel tubular (cfst) structures: Members. *Journal of Constructional Steel Research*, 100:211–228, 2014.

[17] Ahmed Elremaily and Atorod Azizinamini. Experimental behavior of steel beam to cft column connections. *Journal of Constructional Steel Research*, 57 (10):1099–1119, 2001.

[18] Ikhlas S Sheet, Umarani Gunasekaran, and Gregory A MacRae. Experimental investigation of cft column to steel beam connections under cyclic loading. *Journal of Constructional Steel Research*, 86:167–182, 2013.

[19] Atorod Azizinamini and Stephen P Schneider. Moment connections to circular concrete-filled steel tube columns. *Journal of structural Engineering*, 130(2): 213–222, 2004.

[20] Max T Stephens, Lisa M Berg, Dawn E Lehman, and Charles W Roeder. Seismic cfst column-to-precast cap beam connections for accelerated bridge construction. *Journal of Structural Engineering*, 142(9):04016049, 2016.

[21] Max T Stephens, Dawn E Lehman, and Charles W Roeder. Design of cfst column-to-foundation/cap beam connections for moderate and high seismic regions. *Engineering Structures*, 122:323–337, 2016.

[22] Dawn E Lehman and Charles W Roeder. Foundation connections for circular concrete-filled tubes. *Journal of Constructional Steel Research*, 78:212–225, 2012.

[23] Mohamadreza Shafieifar, Mahsa Farzad, and Atorod Azizinamini. Investigation of a detail for connecting precast columns to precast cap beams using ultrahigh-performance concrete. *Journal of bridge engineering*, 25(3):04020001, 2020.

[24] Alireza Mohebbi, M Saiid Saiidi, and Ahmad M Itani. Shake table studies and analysis of a precast two-column bent with advanced materials and pocket connections. *Journal of Bridge Engineering*, 23(7):04018046, 2018.

[25] Abbas Khodayari, Islam M Mantawy, and Atorod Azizinamini. Introducing a new connection detail for connecting prefabricated barrier to concrete deck using uhpc. Technical report, 2021.

[26] Atorod Azizinamini, Sheharyar Rehmat, and Amir Sadeghnejad. Enhancing resiliency and delivery of bridge elements using ultra-high performance concrete as formwork. *Transportation Research Record*, 2673(5):443–453, 2019.

[27] Ali Javed, Islam M Mantawy, and Atorod Azizinamini. 3d-printing of ultra-high-performance concrete for robotic bridge construction. *Transportation Research Record*, page 03611981211011645, 2021.

[28] Sheharyar Rehmat, Amir Sadeghnejad, Islam M Mantawy, and Atorod Azizinamini. Experimental study on concrete filled steel tubes to footing connection using ultra-high performance concrete. *Engineering Structures*, 242:112540, 2021.

[29] Wu Xu, Lin-Hai Han, and Wei Li. Seismic performance of concrete-encased column base for hexagonal concrete-filled steel tube: experimental study. *Journal of Constructional Steel Research*, 121:352–369, 2016.

[30] Yan Xiao, Zhongxin Zhang, Jianhua Hu, Sashi K Kunnath, and Pengxin Guo. Seismic behavior of cft column and steel pile footings. *Journal of Bridge Engineering*, 16(5):575–586, 2011.

[31] H-L Hsu and H-W Lin. Improving seismic performance of concrete-filled tube to base connections. *Journal of Constructional Steel Research*, 62(12):1333–1340, 2006.

[32] Hee-Ju Kim, Jong-Wan Hu, and Won-Sup Hwang. Cyclic testing for structural detail improvement of cft column-foundation connections. *Sustainability*, 7(5): 5260–5281, 2015.

[33] Angela Kingsley, Travis Williams, Dawn Lehman, and Charles Roeder. Experimental investigation of column-to-footing connections for high-strength vanadium steel concrete filled tube construction. *Int. J. Steel Struct*, 5(4):377–387, 2005.

[34] Julia Marson and Michel Bruneau. Cyclic testing of concrete-filled circular steel bridge piers having encased fixed-based detail. *Journal of Bridge Engineering*, 9(1):14–23, 2004.

[35] Jun Kawaguchi, Shosuke Morino, and Akiyoshi Tsuji. Fundamental behavior of cft semi-embedded type column base. In *Proc. US-Japan Seminar on Advanced Stability and Seismicity Concept for Performance-based Design of Steel and Composite Structure, Kyoto, pp.'l29-135*, 2001.

[36] Qi-yun Qiao, Wen-wen Zhang, Ben Mou, and Wan-lin Cao. Seismic behavior of exposed concrete filled steel tube column bases with embedded reinforcing bars: Experimental investigation. *Thin-Walled Structures*, 136:367–381, 2019.

[37] Christopher A Trautner, Tara Hutchinson, Philipp R Grosser, and John F Silva. Investigation of steel column–baseplate connection details incorporating ductile anchors. *Journal of Structural Engineering*, 143(8):04017074, 2017.

[38] Woo-Young Lim, Dongkeun Lee, and Young-Chan You. Exposed column-base plate strong-axis connections for small-size steel construction. *Journal of Constructional Steel Research*, 137:286–296, 2017.

[39] James M Fisher and LA Kloiber. Steel design guide 1-base plate and anchor rod design. In *AISC*, pages 801–06, 2006.

[40] Xian Li, Tao Zhou, Jian Li, Xiao-Bo Kuang, and Yu-Wei Zhao. Seismic behavior of encased cft column base connections. *Engineering Structures*, 182:363–378, 2019.

[41] SJ Fulmer, MJ Kowalsky, and JM Nau. Grouted shear stud connection for steel bridge substructures. *Journal of Constructional Steel Research*, 109:72–86, 2015.

[42] Jiho Moon, Dawn E Lehman, Charles W Roeder, and Hak-Eun Lee. Evaluation of embedded concrete-filled tube (cft) column-to-foundation connections. *Engineering structures*, 56:22–35, 2013.

[43] Atorod Azizinamini and James B Radziminski. Static and cyclic performance of semirigid steel beam-to-column connections. *Journal of Structural engineering*, 115(12):2979–2999, 1989.

[44] Charles Roeder, Dawn Lehman, et al. Initial investigation of reinforced concrete filled tubes for use in bridge foundations. Technical report, Washington (State). Dept. of Transportation. Office of Research and Library ..., 2012.

[45] Max Taylor Stephens, Dawn E Lehman, and Charles W Roeder. Concrete-filled tube bridge pier connections for accelerated bridge construction. Technical report, 2015.

[46] S Rehmat, K Lau, and A Azizinamini. Development of quality assurance and quality control system for post tensioned segmental bridges in florida: Case of ringling bridge—phase ii. *Tallahassee, Florida: Florida Department of Transportation*, 2018.

[47] Atta E Mustafa, Ali Javed, and Khawaja Ali. Safety assessment of cables of suspension bridge under blast load. In *Structures Congress 2022*, pages 79–93.

[48] Ali Javed, Amir Sadeghnejad, Aaron Yakel, Atorod Azizinamini, et al. Magnetic flux leakage (mfl) method for damage detection in internal post-tensioning tendons. 2021.

[49] Muhammad Faheem Ud Din Afzal, Yasunao Matsumoto, Hitoshi Nohmi, Shigekazu Sakai, Di Su, and Tomonori Nagayama. Comparison of radar based displacement measurement systems with conventional systems in vibration measurements at a cable stayed bridge.

[50] PI-Islam Mantawy. *OPTIMIZATION OF ADVANCED CEMENTITIOUS MATERIAL OVERLAYS AND UPGRADES, INCLUDING SHOTCRETE*. PhD thesis, Florida International University, 2020.

[51] PI-Atorod Azizinamini. Use of uhpc in conjunction with pneumatic spray application and robotics for repair and strengthening of culverts-phase i. 2021.

[52] Henry G Russell, Benjamin A Graybeal, Henry G Russell, et al. Ultra-high performance concrete: A state-of-the-art report for the bridge community. Technical report, United States. Federal Highway Administration. Office of Infrastructure ..., 2013.

[53] Sukhoon Pyo, Million Tafesse, Heeae Kim, and Hyeong-Ki Kim. Effect of chloride content on mechanical properties of ultra high performance concrete. *Cement and Concrete Composites*, 84:175–187, 2017.

[54] N Roux, Cid Andrade, and MA Sanjuan. Experimental study of durability of reactive powder concretes. *Journal of materials in civil engineering*, 8(1):1–6, 1996.

[55] Sukhoon Pyo, Selamu Yihune Abate, and Hyeong-Ki Kim. Abrasion resistance of ultra high performance concrete incorporating coarser aggregate. *Construction and Building Materials*, 165:11–16, 2018.

[56] Nerma Caluk, Islam Mantawy, and Atorod Azizinamini. Durable bridge columns using stay-in-place uhpc shells for accelerated bridge construction. *Infrastructures*, 4(2):25, 2019.

[57] Mohamadreza Shafieifar, Mahsa Farzad, and Atorod Azizinamini. New connection detail to connect precast column to cap beam using ultra-high-performance concrete in accelerated bridge construction applications. *Transportation Research Record*, 2672(41):207–220, 2018.

[58] Mostafa Tazarv and M Saiid Saiidi. Uhpc-filled duct connections for accelerated bridge construction of rc columns in high seismic zones. *Engineering Structures*, 99:413–422, 2015.

[59] Guangda Zhang, Qiang Han, Kun Xu, Xiuli Du, and Weili He. Experimental investigation of seismic behavior of uhpc-filled socket precast bridge column-foundation connection with shear keys. *Engineering Structures*, page 111527, 2020.

[60] Zhen Wang, Jingquan Wang, Jianzhong Liu, Fangyu Han, and Jian Zhang. Large-scale quasi-static testing of precast bridge column with pocket connections using noncontact lap-spliced bars and uhpc grout. *Bulletin of Earthquake Engineering*, 17(9):5021–5044, 2019.

[61] Mahsa Farzad, Siavash Rastkar, Amir Sadeghnejad, and Atorod Azizinamini. Simplified method to estimate the moment capacity of circular columns repaired with uhpc. *Infrastructures*, 4(3):45, 2019.

[62] John B Mander, Michael JN Priestley, and R Park. Theoretical stress-strain model for confined concrete. *Journal of structural engineering*, 114(8):1804–1826, 1988.

[63] Tiziano Perea. *Analytical and experimental study on slender concrete-filled steel tube columns and beam-columns*. Georgia Institute of Technology, 2010.

[64] Mahmudur Rahman, Yoshiaki Okui, and Muhammad Atif Anwer. Probabilistic strength at serviceability limit state for normal and sbhs slender stiffened plates under uniaxial compression. *International Journal of Steel Structures*, 18(4): 1397–1409, 2018.

[65] Mahmudur Rahman, Yoshiaki Okui, Masato Komuro, Muhammad Atif Anwer, and Azusa Numata. Probabilistic compressive strength of stiffened steel plates exhibiting column-like behavior: Ultimate and serviceability limit states. *Journal of Structural Engineering*, 146(9):04020166, 2020.

[66] Jiho Moon, Charles W Roeder, Dawn E Lehman, and Hak-Eun Lee. Analytical modeling of bending of circular concrete-filled steel tubes. *Engineering structures*, 42:349–361, 2012.

[67] Lin-Hai Han, Chuan-Chuan Hou, and Wu Xu. Seismic performance of concrete-encased column base for hexagonal concrete-filled steel tube: numerical study. *Journal of Constructional Steel Research*, 149:225–238, 2018.

[68] Keum-Sung Park, Jiho Moon, Sang-Sup Lee, Kyu-Woong Bae, and Charles W Roeder. Embedded steel column-to-foundation connection for a modular structural system. *Engineering Structures*, 110:244–257, 2016.

[69] Ansys. Ansys academic research mechanical, release 18.1.

[70] Joško Ožbolt, Yijun Li, and Ivica Kožar. Microplane model for concrete with relaxed kinematic constraint. *International journal of solids and structures*, 38 (16):2683–2711, 2001.

[71] Imadeddin Zreid and Michael Kaliske. A gradient enhanced plasticity–damage microplane model for concrete. *Computational Mechanics*, 62(5):1239–1257, 2018.

[72] Stephen P Schneider. Axially loaded concrete-filled steel tubes. *Journal of structural Engineering*, 124(10):1125–1138, 1998.

[73] Junhui Cao, Xudong Shao, Lu Deng, and Yidong Gan. Static and fatigue behavior of short-headed studs embedded in a thin ultrahigh-performance concrete layer. *Journal of Bridge Engineering*, 22(5):04017005, 2017.

[74] Junhui Cao and Xudong Shao. Finite element analysis of headed studs embedded in thin uhpc. *Journal of Constructional Steel Research*, 161:355–368, 2019.

[75] Zhaofei Lin, Yuqing Liu, and Jun He. Behavior of stud connectors under combined shear and tension loads. *Engineering structures*, 81:362–376, 2014.

[76] Lewei Tong, Luhua Chen, Ming Wen, and Chen Xu. Static behavior of stud shear connectors in high-strength-steel–uhpc composite beams. *Engineering Structures*, 218:110827, 2020.

[77] J Zeghiche and K Chaoui. An experimental behaviour of concrete-filled steel tubular columns. *Journal of constructional steel research*, 61(1):53–66, 2005.

[78] Martin D O'Shea and Russell Q Bridge. Design of circular thin-walled concrete filled steel tubes. *Journal of Structural Engineering*, 126(11):1295–1303, 2000.

[79] Aaron D Probst, Thomas H-K Kang, Chris Ramseyer, and Uksun Kim. Composite flexural behavior of full-scale concrete-filled tubes without axial loads. *Journal of structural engineering*, 136(11):1401–1412, 2010.

[80] Ming-Xiang Xiong and JY Richard Liew. Discussion on the applicability of the mn interaction curve for the fire resistance design of cft members. *Thin-Walled Structures*, 125:172–186, 2018.

[81] LRFD AASHTO. Aashto lrfd bridge design specifications, 2012.

[82] AISC Committee et al. Specification for structural steel buildings (ansi/aisc 360-10). *American Institute of Steel Construction, Chicago-Illinois*, 2010.

[83] Dominic Kruszewski, Kay Wille, and Arash E Zaghi. Push-out behavior of headed shear studs welded on thin plates and embedded in uhpc. *Engineering Structures*, 173:429–441, 2018.

[84] Konstantinos G Vandoros and Stephanos E Dritsos. Concrete jacket construction detail effectiveness when strengthening rc columns. *Construction and Building Materials*, 22(3):264–276, 2008.

[85] Guoshan Xu, Bin Wu, Dedeng Jia, Xiaotong Xu, and Ge Yang. Quasi-static tests of rc columns under variable axial forces and rotations. *Engineering Structures*, 162:60–71, 2018.

VITA

SHEHARYAR E REHMAT

2008	B.Sc., Civil Engineering University of Engineering and Technology Taxila, Pakistan
2015	M.E., Environmental Science and Civil Engg Saitama University Saitama-shi, Japan
2016−2022	Doctoral Candidate, Civil Engineering Florida International University Maimi, Florida

PUBLICATIONS PRESENTATIONS

Sheharyar Rehmat, Amir Sadeghnejad, Islam Mantawy, and Azizinamini, A., 2021. Experimental study on concrete filled steel tubes to footing connection using ultra-high performance concrete. Engineering Structures (2021), 242, p.112540.

Sheharyar Rehmat, Amir Sadeghnejad and Atorod Azizinamini. "Connection Details for Concrete Filled Tubes using UHPC for Resilient Bridge Substructure." Transportation Research Record, no. 5 (2021)

Azizinamini, Atorod, Sheharyar Rehmat, and Amir Sadeghnejad. "Enhancing resiliency and delivery of bridge elements using ultra-high performance concrete as formwork." Transportation Research Record 2673, no. 5 (2019): 443-453.

Rehmat, Sheharyar, Azizinamini, Atorod. "Non-destructive testing (NDT) of a segmental concrete bridge scheduled for demolition, with a focus on condition assessment and corrosion detection of internal tendons." (2017).

Dammika, A. J., R. Sheharyar, R. Takanami, H. Yamaguchi, and Y. Matsumoto. "An investigation on modal damping ratio as an indicator of invisible damage in PC

bridges." Life-Cycle of Structural Systems: Design, Assessment, Maintenance and Management (2014): 404.

Tanaka, T., S. Rehmat, Y. Matsumoto, and Abeykoon J. Dammika. "Damping properties of existing single-span prestressed concrete girder bridges with different service periods." In the 6th International Conference on Structural Engineering and Construction Management, pp. 11-13. 2015.

Sadeghnejad, Amir, Sheharyar Rehmat, Islam M. Mantawy, and Atorod Azizinamini. "Comparative Study of Cyclic and Shake Table Tests for Simple for Dead Load and Continuous for Live Load Steel Bridge System in Seismic Area." Transportation Research Record (2020): 0361198120921853.

Rehmat, Sheharyar, Amir Sadeghnejad, and Atorod Azizinamini. "Prefabricated UHPC Structural Formwork for Cap Beams." In International Interactive Symposium on Ultra-High Performance Concrete, vol. 2, no. 1. Iowa State University Digital Press, 2019.

Sadeghnejad, Amir, Sheharyar Rehmat, and Atorod Azizinamini. "Development of Innovative Short-Span Bridge System Using UHPC Formworks." In International Interactive Symposium on Ultra-High Performance Concrete, vol. 2, no. 1. Iowa State University Digital Press, 2019.

Rehmat, Sheharyar, Amir Sadeghnejad, and Atorod Azizinamini. "Connection between Concrete Filled Tube (CFT) Columns and Prefabricated elements using UHPC." In International Interactive Symposium on Ultra-High Performance Concrete, vol. 2, no. 1. Iowa State University Digital Press, 2019.

Rehmat, Sheharyar, Lau, Kingsley, and Atorod Azizinamini. "Development of Quality Assurance and Quality Control System for Post Tensioned Segmental Bridges in Florida: Case of Ringling Bridge-Phase II." (2018).

Rehmat, Sheharyar, Sadeghnejad, Amir, Alireza Valikhani, Brian Chunn, Kingsley Lau, and Atorod Azizinamini. Magnetic Flux Leakage Method for Detecting Corrosion in Post Tensioned Segmental Concrete Bridges in Presence of Secondary Reinforcement. No. 17-05231. 2017.